Preparation, Characterization and Study of Magnetic Properties of Co_xCu_{1-x} $(0.01 \leq x \leq 0.7)$ Granular Alloys

by

Susmita Dhara

Enrolment No.: PHYS05201004005

Saha Institute of Nuclear Physics
Kolkata

A thesis submitted to the
Board of Studies in Physical Science Discipline
In partial fulfillment of requirements
For the Degree of

DOCTOR OF PHILOSOPHY

of

HOMI BHABHA NATIONAL INSTITUTE

November, 2016

Homi Bhabha National Institute

Recommendations of the Viva Voce Committee

As members of the Viva Voce Committee, we certify that we have read the dissertation prepared by Susmita Dhara entitled “Preparation, characterization and study of magnetic properties of Co_xCu_{1-x} ($0.01 \leq x \leq 0.70$) granular alloys” and recommend that it may be accepted as fulfilling the thesis requirement for the award of Degree of Doctor of Philosophy.

Date :

Chairman : **Prof. Prabhat Mandal**, SINP

Date :

Guide & Convener : **Prof. Bilwadal Bandyopadhyay**, SINP

Date :

Member : **Dr. Gayatri N Banerjee**, VECC

Date :

Member : **Prof. Indranil Das**, SINP

Date :

External Examiner : **Dr. Zakir Hossain**, IIT Kanpur

Final approval and acceptance of this thesis is contingent upon the candidate’s submission of the final copies of the thesis to HBNI.

I hereby certify that I have read this thesis prepared under my direction and recommend that it may be accepted as fulfilling the thesis requirement.

Date :
Place : **Guide**

STATEMENT BY AUTHOR

This dissertation has been submitted in partial fulfillment of requirements for an advanced degree at Homi Bhabha National Institute (HBNI) and is deposited in the Library to be made available to borrowers under rules of the HBNI.

Brief quotations from this dissertation are allowable without special permission, provided that accurate acknowledgement of source is made. Requests for permission for extended quotation from or reproduction of this manuscript in whole or in part may be granted by the Competent Authority of HBNI when in his or her judgment the proposed use of the material is in the interests of scholarship. In all other instances, however, permission must be obtained from the author.

Susmita Dhara

DECLARATION

I, hereby declare that the investigation presented in the thesis has been carried out by me. The work is original and has not been submitted earlier as a whole or in part for a degree / diploma at this or any other Institution / University.

Susmita Dhara

“Fill the brain, therefore, with high thoughts, highest ideals, place them day and night before you, and out of that will come great work. Talk not about impurity, but say that we are pure."

— Swami Vivekananda

“Difficulties in your life do not to destroy you, but to help you realise your hidden potential and power, let difficulties know that you too are difficult"

— Dr. A. P. J. Abdul Kalam

List of Publications arising from the thesis

Journal

1. **"Synthesis, characterization and magnetic properties of Co_xCu_{1-x} ($x \sim 0.01 - 0.3$) granular alloys"**,
   S. Dhara, R. Roy Chowdhury, S. Lahiri, P. Ray and B. Bandyopadhyay,
   J. Magn. Magn. Mater. **374**, 647-654 (2015).

2. **"Strong memory effect at room temperature in nanostructured granular alloy $Co_{0.3}Cu_{0.7}$"**,
   S. Dhara, R. Roy Chowdhury, and B. Bandyopadhyay,
   RSC Adv. **5**, 95695-95702 (2015).

3. **"Observation of resistivity minimum in low temperature in nanostructured granular alloys Co_xCu_{1-x} ($x \sim 0.17 - 0.76$)"**,
   S. Dhara, R. Roy Chowdhury, and B. Bandyopadhyay
   Phys. Rev. B (in press).

Conferences

1. **"Magnetization study of Co_xCu_{1-x} nanoparticles"**,
   Susmita Dhara, Rajeswari Roy Chowdhury, Bilwadal Bandyopadhyay,
   Proc. Int. Conf. Magnetic Materials and Applications (MagMA-2013),
   Phys. Procedia **54**, 38-44 (2014).

2. **"Kondo effect in Co_xCu_{1-x} granular alloys prepared by chemical reduction method"**,
   Susmita Dhara, Rajeswari Roy Chowdhury, Bilwadal Bandyopadhyay,
   59^{th} DAE Symp. on Solid State Physics, AIP Conf. Proc. **1665**, 130056 (2015).

3. **"Evidence of formation of Co_xCu_{1-x} nanoparticles with core-shell structure"**,
   Susmita Dhara, Rajeswari Roy Chowdhury, Bilwadal Bandyopadhyay,
   Acta Physica Polonica A. Proc. **128(4)**, 533 (2015)
   .

Other Publications

1. **"Evidence of ferromagnetism in vanadium substituted layered intermetallic compounds $RE(Co_{1-x}V_x)_2Si_2$ (RE = Pr and Nd; $0 \leq x \leq 0.35$)"**,
   R. Roy Chowdhury, S. Dhara, and B. Bandyopadhyay,
   J. Magn. Magn. Mater. **401**, 998-1005 (2015).

2. **" Ferromagnetism in $Nd(Co_{1-x}V_x)_2Si_2$ ($0 \leq x \leq 0.5$)."**,
   Rajeswari Roy Chowdhury, Susmita Dhara, Bilwadal Bandyopadhyay,
   Proc. Int. Conf. Magnetic Materials and Applications (MagMA-2013),
   Phys. Procedia **54**, 113-117 (2014).

3. **"Crossover from Antiferro-to-Ferromagnetism on Substitution of Co by V in $RE(Co_{1-x}V_x)_2Si_2$ ($0 \leq x \leq 0.35$)."**,
   Rajeswari Roy Chowdhury, Susmita Dhara, Bilwadal Bandyopadhyay,
   59^{th} DAE Symp. Solid State Physics, AIP Conf. Proc. **1665**, 130040 (2015).

4. **"Effect of Vanadium Substitution of Cobalt in $NdCo_2Si_2$"**,
   Rajeswari Roy Chowdhury, Susmita Dhara, Bilwadal Bandyopadhyay,
   Acta Physica Polonica A. Proc. **128(4)**, 530 (2015).

5. **"Spectral anion sensing and γ-radiation induced magnetic modifications of polyphenol generated Ag-nanoparticles"**,
   Zarina Ansari, Susmita Dhara, Bilwadal Bandyopadhyay,
   Abhijit Saha, Kamalika Sen,
   Spectrochim. Acta. A. **156**, 98-104 (2016)

DEDICATIONS

Dedicated to My Beloved Parents and Teachers

ACKNOWLEDGMENTS

This thesis is not just words typed on the keyboard; it is the fruit of labor of more than five years in SINP, and a milestone in my life. It is the time to thank everyone who has made this dream of mine a reality. First I would like to express my special appreciation and thanks to my advisor Professor Dr. Bilwadal Bandyopadhyay for offering me this fascinating topic as PhD thesis. I would like to thank you for encouraging my research and for helping me to grow as a research scientist. Thank you for many fruitful discussions, your helpful suggestions and advice, your dedication to the research area of magnetic particles and your trust in my work. Thank you for your sense of humor that I will certainly miss when I leave SINP. Special thanks to Prof. Kajal Ghosh Roy, Prof. Amitava Ghosh Roy, Prof R. Ranganathan, Prof. Prabhat mandal, Prof. Indranil Das and Prof. Chandan Majumder for their helpful comments and suggestions. I would like to express my warm and sincere thanks to my teachers of Physics department, Visva-Bharati University who have inspired me to pursue a research career. I convey my sincere gratitude to Prof. Asish Bhattacharyya, Prof. Arani Chakravarty, Prof. Pijushkanti Ghosh, and Prof. Subhasish Roy for supporting me with their invaluable suggestions and helping me overcome several points of frustration and uncertainty during my whole student life. I am thankful to my primary school teacher Bijay dadamani, for all his help, support and inspiration throughout my whole life.

Many thanks to Rajeswari my sweet lab mate for the great cooperation and for being such a wonderful friend. Thank you Rajeswari for sleepless nights with me while we were working together, and for all the fun we have had in the last five years. I want to thank Dr. Kalipada Das for the stimulating discussions, helpful suggestions and brilliant analysis and ideas. He was always there cheering me up and stood by me through the good times and bad. Also, my thanks go to Arindam da, Nazir da, Mayukh Da, Manasi Di as seniors who

helped me a lot with the fruitful discussions on various topics of this work and also helping in my experiment. Thanks to Mr. Dhrubojyoti Seth, scientific assistant of our NMR group, for his technical assistance during the experiment. Many thanks to Anis da for helping me in all my crucial XRD work. I specially want to thank Arun da who has been an inspiration on how to set-up an experiment perfectly. The ICPOES measurements were done in the lab of Prof. Susanta Lahiri with his active participation and Mr. Pulak Roy took all the TEM micrographs. I am especially indebted to both of them.

Thanks to Mala, Moumita and again Rajeswari, my post M. Sc and my hostel friends (MSA-1) for their great friendship, which I have enjoyed a lot during this research life. I treasure every minute I have spent with them. I should express my gratitude to the all the members of Experimental Condensed Matter Physics Division of Saha Institute of Nuclear Physics (SINP) for their help. Special thanks goes to Dr. Jhishnu Basu for constantly helping me in my research work whenever I have approached him. I am thankful to DAE, Govt. of India for providing me the research fellowships. I am grateful to the director of SINP for providing me the opportunity to work at SINP, and for the hostel accommodation.

A special thanks to my family. I am really thankful to my parents, who constantly inspired and encouraged me in the so-called higher education. Words cannot express how grateful I am to Mana di, Sampu di, Barun da and Anuj da, for all the sacrifices they have made for my career. Your prayer for me was what sustained me thus far. I also like to acknowledge my little nephew Ramya whose innocent smile have cherished me against all odds.

Lastly I want to thank my best friend and husband Rashbihari for every single wonderful moment with you which makes my life so happy and worthwhile!

CONTENTS

SYNOPSIS

Granular magnetic nanoparticle systems of binary alloys have drawn researchers' attention due to their potential technological applications in ultrahigh-density data storage, magnetic memories, spin electronics, magnetic sensors, and applications in biology. For many years, Co_xCu_{1-x} ($x < 0.3$) alloys have been investigated as model granular systems to gain insight into the magnetic and spin dependent transport processes in metallic alloys containing a dispersion of nano magnetic particles. We have prepared Co_xCu_{1-x} ($0.01 \leq x \leq 0.7$) nano alloys by chemical reduction method and studied the variation of their magnetic and transport properties with cobalt concentration. The samples were prepared by reducing appropriate mixtures of $CoCl_2$ and $CuCl_2$ in aqueous solution with cetyltrimethylammonium bromide (*CTAB*) as the capping agent. The chemical compositions of cobalt and copper were determined from inductively coupled plasma optical emission spectroscopy (ICPOES) study. The room temperature powder x-ray diffraction (XRD) studies (Fig. 1(a)) have shown that Co atoms are alloyed in *fcc* copper phase which is is also confirmed from high resolution transmission electron microscopy (HRTEM) (Fig. 1(c)). Average particles size was calculated from the broadening of the XRD peaks using Williamson-Hall method. The TEM images, as shown in the micrograph Fig. 1(b), yielded the particle size histograms (shown in Fig. 1(d) for sample Co-0.01) and the average diameter of the particles were calculated from fitting the histogram using a lognormal distribution function.

On as-prepared samples, magnetic measurements at 4-300 K were carried out in zero-field cooled and field cooled (ZFC/FC) protocol showing a clear branching which indicates the superparamagnetic (SPM) nature for all the samples, except for the sample Co-0.01. For Co-0.01, ZFC and FC magnetization show identical behavior of a simple paramagnetic nature down to 4 K. For other samples Co-0.03 $\longrightarrow$ Co-0.33, the ZFC magnetization shows a broad peak at a temperature T_B^{expt}, the so called blocking temperature, which are centered

Table 1: The cobalt contents in mol % obtained from inductively coupled plasma optical emission spectroscopy (ICPOES) study for samples designated as Co-0.01 $\longrightarrow$ Co-0.33, and their particle sizes calculated from transmission electron microscopy (TEM) studies. Ferromagnetic (FM) and superparamagnetic (SPM) saturation magnetization, M_S^{FM} and M_S^{SPM}, respectively, remanence (M_R), coercivity (H_C), and the average SPM moment for a particle or cluster (μ) for the Co_xCu_{1-x} nanostructured alloys, were obtained from the analysis of magnetization data at 4 K.

Sample	Co mol %	D (TEM) nm	M_S^{FM} (μ_B/Co)	M_R (μ_B/Co)	H_C (mT)	M_S^{SPM} (μ_B/Co)	μ (μ_B)
Co-0.01	1.11(1)	8	–	–	–	1.310(5)	4.5(1)
Co-0.03	2.88(1)	13	0.07(1)	0.030(1)	39(1)	0.48(1)	7.0(1)
Co-0.05	5.28(1)	–	0.08(1)	0.038(1)	42(2)	0.45(1)	7.3(1)
Co-0.08	8.27(1)	–	0.08(1)	0.023(1)	33(1)	0.38(1)	7.5(1)
Co-0.10	10.37(1)	25	0.13(1)	0.076(1)	41(2)	0.225(5)	10.0(1)
Co-0.15	14.97(1)	10	0.12(1)	0.078(1)	42(2)	0.225(5)	10.8(1)
Co-0.21	21.22(1)	13.5	0.20(1)	0.102(1)	34(1)	0.360(5)	11.5(1)
Co-0.33	32.94(1)	18	0.18(1)	0.099(3)	32(1)	0.200(5)	13.0(1)

at various temperatures in between 40-90 K for all samples. ZFC and FC magnetization curves bifurcate at a certain temperature, T_p, higher than T_B^{expt}. These samples are SPM above those bifurcation temperatures. In case of a nanoparticle system having a size distribution, there is a distribution in blocking temperature T_B which represent variations in particle size and inhomogeneities of their chemical compositions (shown in Fig. 2(b)). The ZFC/FC behavior can be fitted using non-interacting superparamagnetic model (shown in Fig. 2(a) for sample Co-0.20) taking consideration of the distributions in volume and blocking temperature of the particles.

We have measured the thermo-remanent magnetization (TRM), and fitted the experimental data using independent particles model. The blocking temperature obtained from TRM have nearly the same values with blocking temperatures from ZFC/FC magnetization measurements. The magnetic field (H) dependence of magnetization (M) were studied for all samples at different temperatures 4-300 K, in ZFC condition in between -7 T to 7 T. At 4 K, Co-0.01 shows no coercivity and exhibits SPM magnetization behavior identical in ascending and descending fields. All other samples exhibit prominent hysteresis loops yielding coercive fields (H_C) of $\sim$ 40 mT. The $Mvs.H$ can be fitted by the following equation

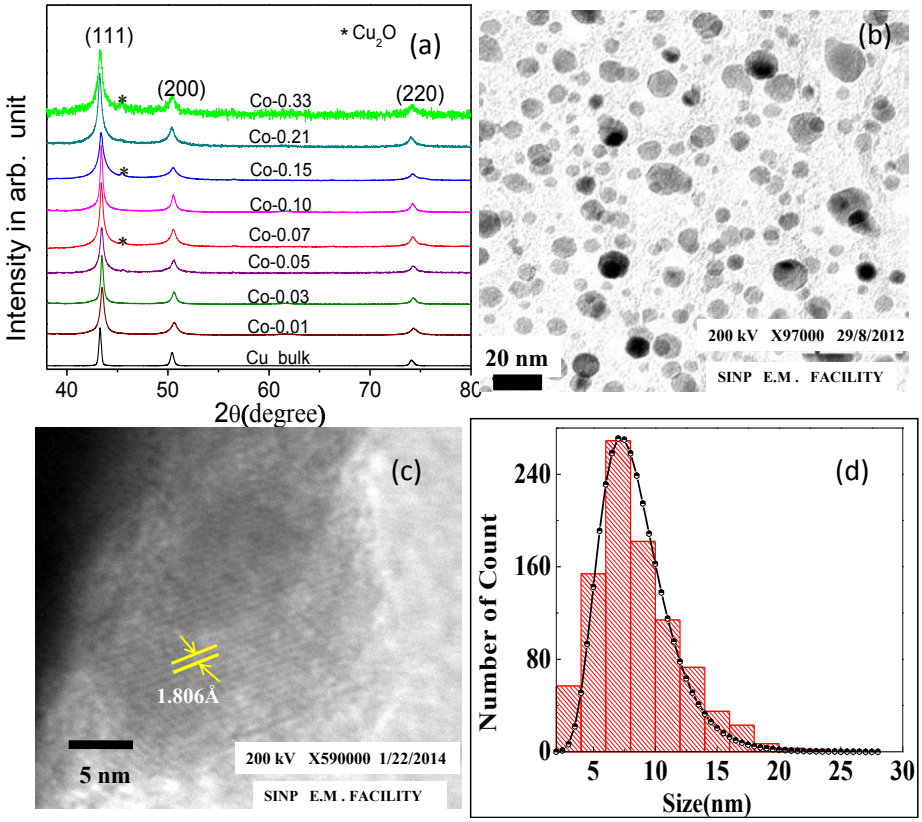

Figure 1: *(a) Room temperature x-ray diffraction (XRD) patterns of samples Co-0.01 $\longrightarrow$ Co-0.33 and bulk Cu powder; (b) transmission electron micrograph of sample Co-0.01; (c) high resolution transmission electron micrograph of sample Co-0.21; and (d) particle size histogram of sample Co-0.01.*

(shown in Fig. 2(d)for sample Co-0.20).

$$M(H) = \frac{2M_S^{FM}}{\pi}\left[tan^{-1}\left[\left(\frac{H \pm H_C}{H_C}\right)tan\left(\frac{\pi M_R}{2M_S^{FM}}\right)\right]\right] + M_S^{SPM}\left[coth\left(\frac{\mu H}{k_B T}\right) - \left(\frac{\mu H}{k_B T}\right)^{-1}\right] + \chi^{PM} H \tag{1}$$

The first and second terms on the right hand side of the equation represent the FM and SPM contributions, respectively. The fitting parameters are M_S^{FM} and M_S^{SPM}, the saturation magnetization for FM and SPM parts, respectively, in terms of magnetic moment per Co atom, and μ, the average magnetic moment of SPM particles or clusters. The values

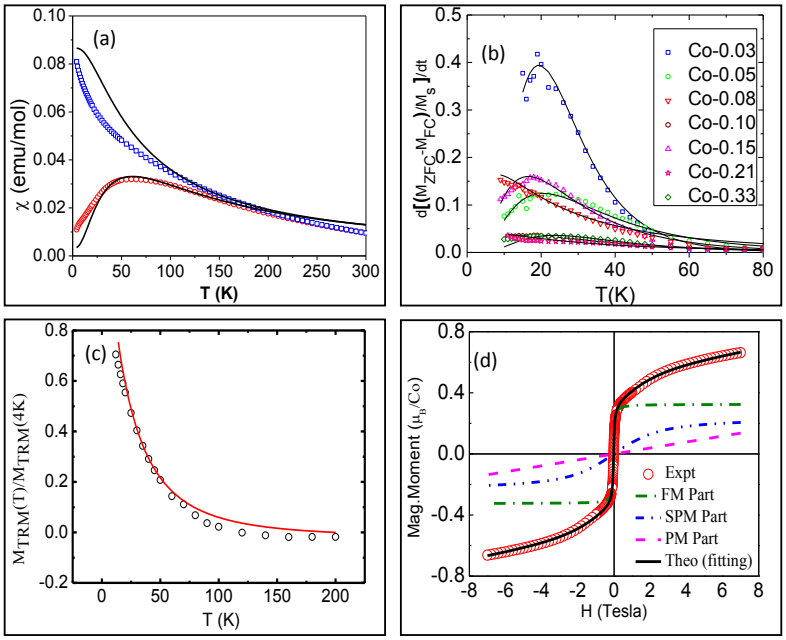

Figure 2: *(a) Zero-field cooled (ZFC, open symbols) and field-cooled (FC, solid symbols) magnetic susceptibilities of Co-0.21, measured with 10 mT probing field. Solid lines are theoretical fit using noninteracting superparamagnetic particles model; (b) blocking temperature distributions for samples Co-0.03 $\longrightarrow$ Co-0.33. Solid lines are fitting with a lognormal distribution; (c) thermoremanent magnetization (TRM) of sample Co-0.21, solid lines are theoretical fit; and (d) data for descending magnetic fields of hysteresis loops obtained at 4 K for samples Co-0.21. The experimental data are shown by open circles. The simulations using Eq. 1 are shown as the FM (dash and dot), the SPM (dash, dot and dot), the PM (dash) components and their sum (continuous line).*

of remanence, M_R, and, coercivity, H_C are obtained from experimental data. The third term in the equation represents a paramagnetic (PM) contribution, nearly uniform in all samples, with $\chi^{PM} \sim 10^{-6}\mu_B$/Oe. The various parameters in Eq. 1 obtained from fitting are given in Table 1. From the above we have concluded that in Co-0.01 sample with the lowest cobalt concentration of Co$\sim$ 1%, there is negligible interaction among Co magnetic moments. In all other samples, the magnetization is a combination of ferromagnetic and superparamagnetic contributions with a blocking temperature distribution. The above observations indicate that in the nanoparticles there is a cobalt rich part where ferromagnetism is favored, and another part low in cobalt that is superparamagnetic. Since no segregation of copper and cobalt is observed in any sample, it has been concluded that

Co_xCu_{1-x} alloy particles are formed in a core-shell type structure with the Co rich part at the core. The paramagnetic contribution to the magnetization comes from dilute Co atoms embedded in copper at or near the surface of particles. The magnetic properties of an assembly of such particles, as we have studied here, are largely determined by the dipolar and exchange interactions among the cluster of Co atoms within a particle. Since they are capped with a surfactant, the particles are isolated and inter-particle interactions are negligible.

Upon annealing the samples, the maximum of the ZFC curves are shifted to above room temperature. The blocking temperatures now estimated for Co-0.03 $\longrightarrow$ Co-0.76 samples are in the range 350-380 K. At low temperatures 2-7 K, the ZFC curves at low fields show a sharp small peak followed by a minimum. This behavior is due to the occurrence of spin-glass like ordering which has been investigated in course of relaxation and memory effect studies.

For annealed samples, the hysteresis loops at various temperatures 2-300 K were obtained in both ZFC and FC conditions and there was the existence of exchange bias field in the samples. As observed earlier, these particles are formed in a core-shell type structure in which the blocked moments in Co rich core become ferromagnetic. The dilute Co moments outside the core region do not contribute to ferromagnetism. On the contrary, there is a strong possibility of AFM interaction between isolated pair of Co moments away from the core region and thus formation of FM-AFM interface giving rise to the exchange bias (H_{EB}). H_{EB} increases continuously with decrease in temperature until about 10 K, where, only at this low temperature, H_{EB} is affected by the onset of spin-glass ordering. For low Co samples exchange bias varies in the range 7-2 mT decreasing with temperature. For high Co samples with Co $>$ 30%, the exchange bias disappears. There is possibly no well defined core and shell regions in high Co samples.

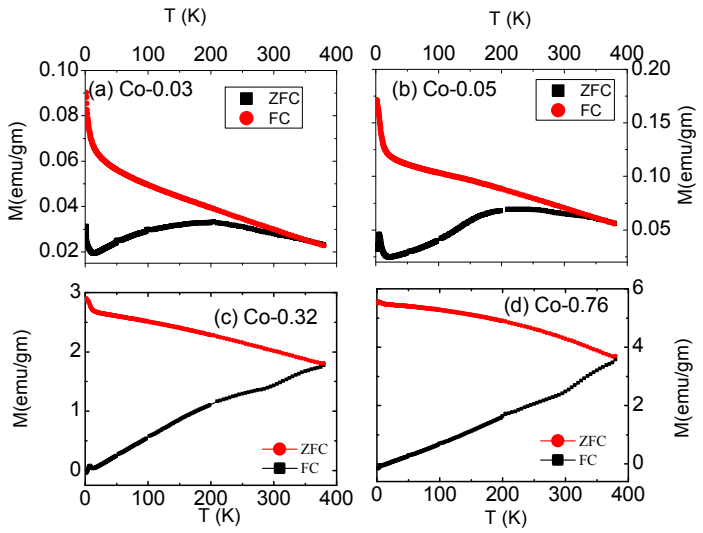

Figure 3: *Zero-field cooled (ZFC, black square) and field-cooled (FC, red circle) magnetization measured with 10 mT probing field in annealed samples: (a) Co-0.03, (b) Co-0.05, (c) Co-0.32; and Co-0.76.*

The *dc* magnetic relaxation study of $Co_{0.32}Cu_{0.68}$ has been performed at different temperatures 2-300 K. $M(t)vs.t$ can be fitted very well as a sum of exponential decay of two magnetization components. One component corresponds to the blocked part of the magnetic moments with long relaxation time ($\sim 10^4 - 10^6$ s) which signifies a negligible interaction among the supermoments and this part is dominant in all temperature. Another part with a shorter relaxation time ($\sim 10^2$ s) has a small magnitude at low temperatures. It tends to grow as temperature increases and therefore corresponds to the SPM component. We have fitted the relaxation data using the Ulrich's equation and calculated the strength of inter-particle dipolar interaction as a function of temperature and particle density. The relaxation measurements confirm that our system is an assembly of non-interacting or weakly interacting nanoparticles.

We have studied the memory effect in detail in $Co_{0.30}Cu_{0.70}$ using both ZFC and FC protocols. In FC protocol the study resulted in a step-like $M(T)$ curve form 4 K to 300 K. Step like memory effect appear in FC magnetization of a nanoparticle system, whether non-interacting or interacting, whenever there is a particle size distribution, and therefore,

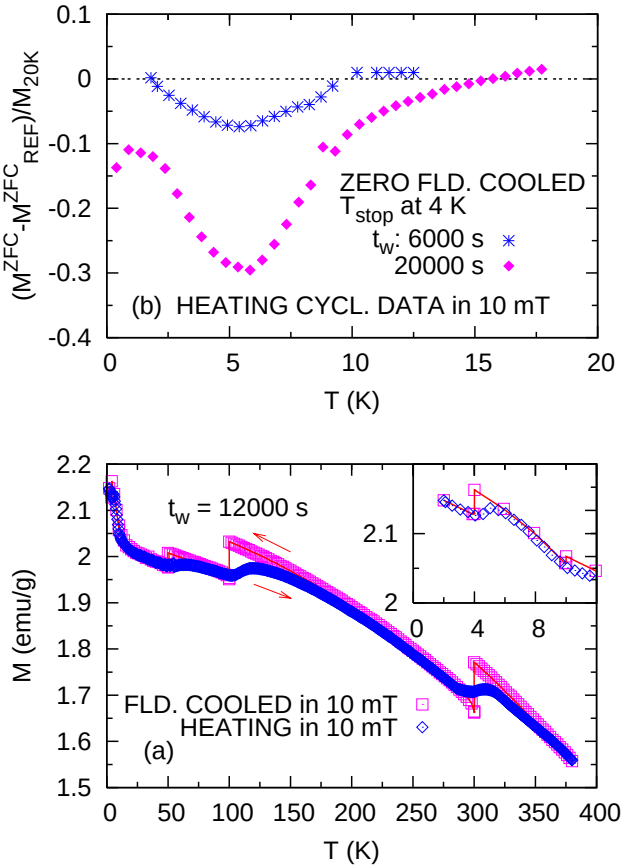

Figure 4: *For sample $Co_{0.32}Cu_{0.68}$, (a) temperature (T) dependence of magnetization (M) during cooling in 10 mT magnetic field (squares) with cooling temporarily stopped for t_w of 12000 s at each of temperatures (T_{stop}) of 300, 100, 50, 10 and 4 K, followed by Mvs.T under conditions of continuous heating in 10 mT (rhombuses). Inset shows same data for expanded low temperature region; (b) the difference of M^{ZFC} and M^{ZFC}_{REF}, both measured during continuous heating in 10 mT following zero-field cooling. For M^{ZFC} there was temporary stop at 4 K during zero-field cooling. The data were taken twice; for t_w of 6000 s (stars) and 20000 s (filled symbols).*

a distribution in blocking temperature. In our samples, the blocking temperature has an upper limit of 350-380 K, and significant memory effect persists even at 300 K. Memory effect has been further investigated by studying relaxation dynamics using the experimental protocol of Sun *et al.*.

Below about 7 K, memory effect has been observed even in ZFC condition, confirming spin-glass like ordering at these temperatures.

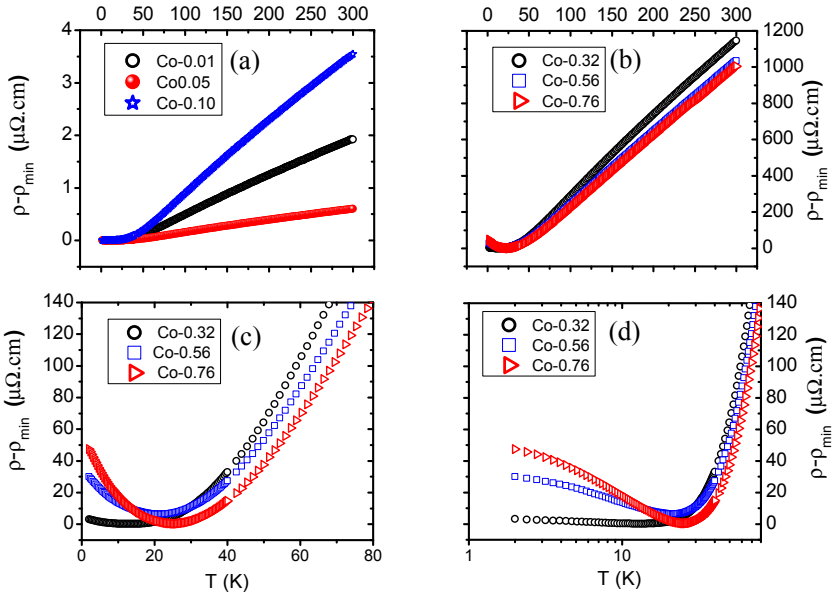

Figure 5: Resistivity (ρ) as a function of temperature for (a) samples Co-0.01, Co-0.05 and Co-0.10; (b) samples Co-0.32, Co-0.56 and Co-0.76; (c) expanded low temperature region of Fig. 5(b); and (d) logarithmic plot of expanded low temperature region of Fig. 5(b).

Electrical resistivity of Co_xCu_{1-x} $(0.01 \leq x \leq 0.7)$ granular nanoparticle system using four probe method was measured as a function of temperature in zero field and in presence of magnetic field. Figure 5 shows the resistivities as a function of temperature 2-300 K. The samples with low cobalt content of $x \leq 0.1$ show a metallic resistivity behavior. For samples with higher cobalt content, $x \geq 0.17$, the resistivity shows a minimum. The minimum becomes more pronounced as Co content (x) increases and also the temperature of minimum resistivity, T_{min}, increases with x. Such trends continue even when x is as high as $\sim 76\%$. This is the first time resistivity minimum is observed in a metal alloy system with such high concentrations of a ferromagnetic element. Below T_{min}, there is a logarithmic temperature dependence of resistivity. The magnitude of resistivity is slightly suppressed on application of magnetic field. We have tried to analyze and find out the possible mechanism of the upturn in resistivity in low temperature. In granular alloys

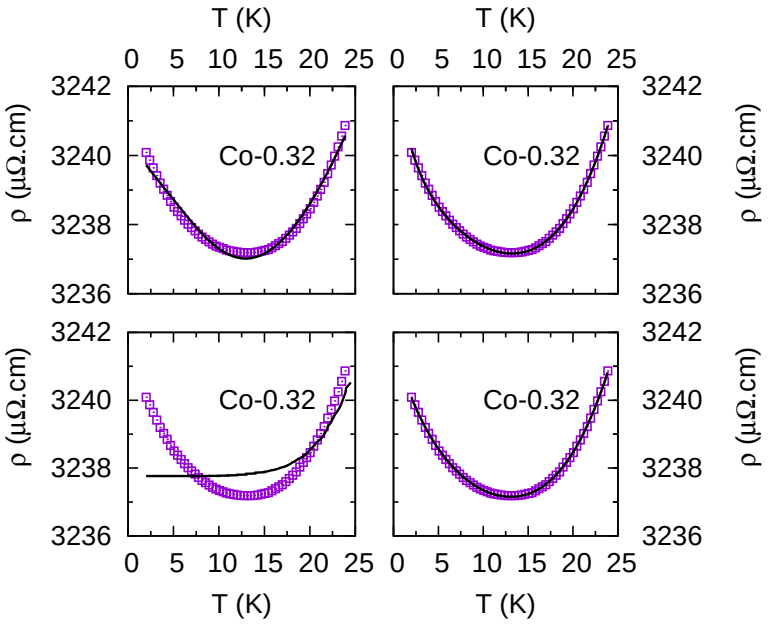

Figure 6: Fitting of low temperature resistivity upturn of Co-0.32 sample. The experimental data (□) are fitted (solid line) for (a) Coulomb blocking effect; (b) inter-grain tunneling of electrons; (c) Kondo effect; and (d) elastic scattering of electrons.

or nanoparticle systems, the resistivity upturn in low temperature has been described by different mechanisms, *e.g.*, electron-electron ($e-e$) scattering, Coulomb blockade effect and Kondo effect. While trying to fit the experimental data with expressions corresponding to each of these interactions, we found that the best fit is obtained by taking the $e-e$ like elastic scattering term ($-\rho_q T^{1/2}$) (shown in Fig. 6) in case of all the samples. Detailed analysis suggests that the low temperature upturn in resistivity most probably arises due to elastic electron-electron interaction (quantum interference effect). Magnetic measurements at 4 K on the same samples show absence of long range magnetic interaction and evidence of increasing magnetic disorder as x increases beyond $\sim 10\%$. Combining the results of the two types of measurements, a model of formation of these alloy particles involving random clusters of Co atoms within Cu matrix has been proposed.

The thesis is composed of four chapters and these are as follows.

Chapter 1. INTRODUCTION

The chapter gives a general introduction of magnetism, and the motivation and scope of the present work. Some basic theories of magnetism of nanoparticle systems are discussed in this chapter.

Chapter 2. EXPERIMENTAL TECHNIQUE

The sample preparation procedure is thoroughly described in this chapter. Various commercial instruments were used to characterize and measure the physical properties of the prepared samples. The working principles of those instruments are briefly discussed in this chapter. The details of chemical, structural, and microscopic characterization are also presented.

Chapter 3. RESULTS AND DISCUSSION

Some general experiments like zero field cooled and field cooled magnetization, thermo-remanence magnetization, hysteresis loop etc., are performed to understand the magnetic behavior of the samples. Exchange bias, *dc* relaxation, memory effects are also studied on annealed samples to understand the total magnetic behavior. The temperature and field dependent resistivity behavior have been studied to compliment the results of magnetization measurements.

Chapter 4. SUMMARY AND CONCLUSION

The key observations of the present work and prospects of further studies are discussed in this chapter.

LIST OF FIGURES

LIST OF TABLES

CHAPTER 1

INTRODUCTION

From about two thousand years ago when loadstone compasses were being used by Chinese navigators, magnetism and magnetic phenomena have been among the important aspects of human civilization. In the present day, magnets and magnetic materials are ubiquitous in computer memory disks, credit and ID cards, loud speakers, refrigerator door seals, cars and toys etc. The scientific development of the subject of magnetism has come through various landmark discoveries beginning with the remarkable conclusion by William Gilbert in 1600 that earth behaves as a giant magnet. That an electric current produces a magnetic field was established through the works of Hans Christian Ørsted, André-Marie Ampère, Carl Friedrich Gauss, Jean-Baptiste Biot, and Félix Savart in early 19th century. Then in 1831, Michael Faraday found that a time-varying magnetic flux through a loop of wire induced a voltage. Finally, James Clerk Maxwell synthesized and expanded these insights into what is now known as Maxwell's equations that constitute the foundation of classical electrodynamics.

A deeper insight into the origin of magnetism has become possible by the quantum mechanical concept of atomic magnetic moment resulting from orbital and spin angular

momentum of unpaired electrons. In most materials the atomic moments are small and aligned randomly, leading to paramagnetism, as shown in Fig. 1.1(a). When atoms are brought in proximity to each other there is a probability of coupling of the spin moments of the atoms through a mechanism known as Heisenberg exchange, causing the spin moments to align parallel or anti-parallel. In some materials, specifically in transition metals such as nickel, cobalt, and iron, the spin moments are large, and align in parallel or ferromagnetically as shown in Fig. 1.1(b). This causes a net spontaneous magnetic moment in the material.

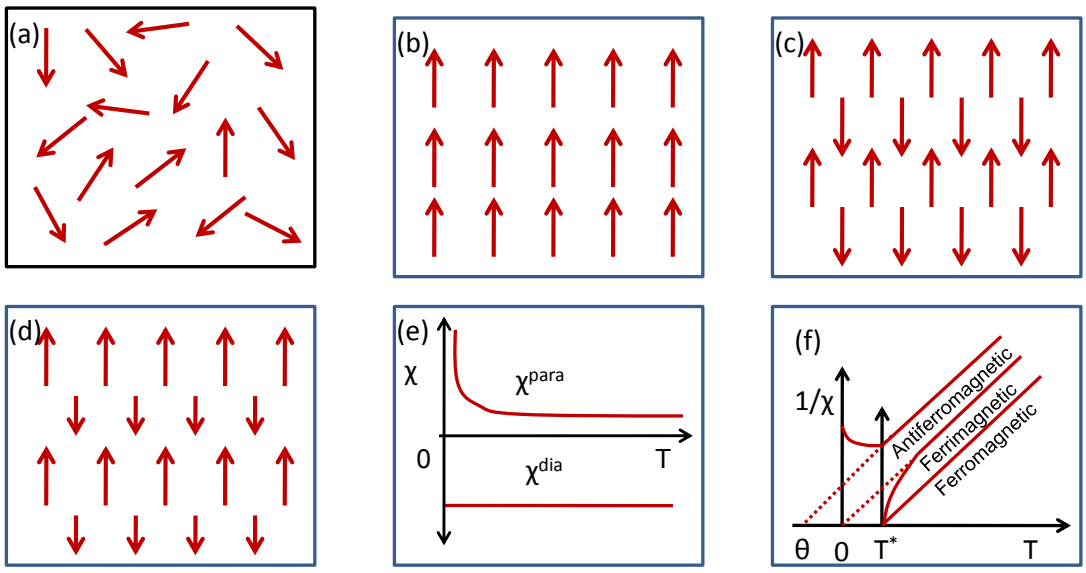

Figure 1.1: Schematic representation of magnetic spin structure; (a) paramagnetic spin moments, (b) ferromagnetic spin moments, (c) antiferromagnetic spin moments, (d) ferrimagnetic spin moments, (e) temperature dependence of the magnetic susceptibility in the case of diamagnetism and paramagnetism; (f) inverse magnetic susceptibility (χ^{-1}) ferromagnetism, antiferromagnetism, and ferrimagnetism with T^* being the critical temperature and θ the paramagnetic Curie temperature.

1.0.1 Classification of Magnetic Materials

A material can be classified in one of the following different magnetism classes depending upon the susceptibility χ and spin structure of the material.

Diamagnetism

Diamagnetism is a very weak form of magnetism that is exhibited only in the presence of an external magnetic field and results from changes in the orbital motion of electrons due to the external magnetic field. An external magnetic field (H) induces atomic or molecular magnetic dipoles which are oriented antiparallel with respect to the exciting field due to Lenz's law. Therefore, the diamagnetic susceptibility is negative.

$$\chi^{dia} = Const. < 0 \tag{1.1}$$

Diamagnetism is present in all materials; however, it is relevant only in the absence of para- and ferromagnetism. Some examples of diamagnetic materials are nearly all organic substances, metals like Hg, superconductors below the critical temperature. For an ideal diamagnet, χ^{dia} is -1. A typical diamagnetic susceptibility with temperature is shown in the Fig 1.1(e).

Paramagnetism

In paramagnetism, the atoms or molecules of the substance have net orbital or spin magnetic moments that tend to be randomly orientated due to thermal fluctuations when there is no magnetic field (shown in Fig 1.1(a)). In a magnetic field these moments start to align parallel to the field such that the magnetisation of the material is proportional

to the applied field. They therefore have a positive susceptibility. Paramagnetism occurs in all atoms and molecules with unpaired electrons, *e.g.*, free atoms, free radicals, and compounds of transition metals containing ions with unfilled electron shells. There are magnetic moments associated with the spins of the conducting electrons in a metal, and in presence of a magnetic field, the imbalance in the numbers of parallel and antiparallel spins results in weak and almost temperature independent paramagnetism.

The susceptibility of paramagnetic materials is characterized by,

$$\chi^{para} = Const. > 0 \tag{1.2}$$

$$\chi^{para} = \chi^{para}(T) \tag{1.3}$$

A typical paramagnetic susceptibility with temperature is shown in the Fig 1.1(e).

Ferromagnetism

Ferromagnetism is a result of an exchange interaction between atomic or molecular magnetic moments. Below a characteristic temperature which is called the Curie temperature T_C, the material from the point of view of magnetism is subdivided into small volumes or so-called 'domains' which typically have sizes $\sim 1\mu$m. The magnetic moments enclosed in these domains exhibit a nearly parallel orientation even in absence of an external magnetic field, *i.e.*, each domain of the material has a spontaneous magnetization. The magnetic moments can again be localized (*e.g.*, Gd, EuO) or itinerant(*e.g.*, Fe, Co, Ni). Depending upon the temperature a ferromagnetic material can be in one of the three states. First condition is when,

$$T > T_C \tag{1.4}$$

The magnetic moments exhibit a random orientation like in paramagnetism. The susceptibility is given by,

$$\chi = \frac{C}{T - T_C} \tag{1.5}$$

which is the Curie-Weiss law. The constant C is called the Curie constant. The second condition is when,

$$0 < T < T_C \tag{1.6}$$

The magnetic moments exhibit a preferential orientation. χ exhibits a significantly more complicated functionality of different parameters compared to dia− and paramagnetism.

$$\chi^{Ferro} = \chi^{Ferro}(T, H, History) \tag{1.7}$$

The third state is when,

$$T = 0 \tag{1.8}$$

All magnetic moments are aligned parallel (shown in Fig. 1.1(b)). A typical inverse ferromagnetic susceptibility with temperature is shown in the Fig 1.1(f).

Antiferromagnetism

In ferromagnetic materials, it is energetically favorable for the atomic spins to orient in the same direction, leading to a spontaneous magnetization. However, in antiferromagnetic materials, the conditions are such that it is energetically favorable for two neighboring spins to orient in opposite directions, leading to no overall magnetization (shown in Fig. 1.1(c)). This is the opposite of ferromagnetism and the transition temperature is called the Néel temperature. Above the Néel temperature, the material is typically paramagnetic. A typical inverse susceptibility with temperature of a antiferromagnetic material is shown in the Fig 1.1(f).

Ferrimagnetism

The magnetic moments are aligned in opposite direction but the aligned moments are not of the same size, *i.e.*, the total moment cancelation is not occurred as in the case of antiferromagnetic material (shown in the Fig. 1.1(d)). Generally this happens when there are more than one type of magnetic ions in material. An overall magnetization is produced but not all the magnetic moments may give a positive contribution to the overall magnetization. A typical inverse susceptibility with temperature of a ferrimagnetic material is shown in the Fig 1.1(f).

1.0.2 Magnetism in nanosized particles

Materials constituted of particles having sizes 1 to 100 nm are called nanostructured material [1]. When the size of the material reduces and reaches the order of nanometers, the influence of the surface atoms becomes comparable or even more important than the bulk contribution. The defects associated with the broken crystalline symmetry and other physical effects may also become very important when the size reduces to nanometer scale. Generally a physical property of a material depends on the size of the material, when the size is comparable to the dimension which is relevant to that property. A large interest in magnetic nanoparticles was observed in last decades by virtue of their various potential applications in fields ranging from ultrahigh-density recording and catalytic chemistry to biology and medicine [2, 3, 4, 5, 6]. Nanostructured materials have very interesting structural, chemical, electrical and magnetic properties [7, 8, 9, 10, 11, 12, 13, 14, 15] which sustain the activity of research in magnetic nanoparticles. Observation of giant magneto resistance in magnetic thin films [16, 17] and granular systems of Fe, Co and Ni and in their binary alloys with Cu, Ag and Au have enhanced the interest [18, 19, 20].

As mentioned before, bulk ferromagnetic materials are constituted of magnetic domains whose size depends on various parameters, such as, temperature, magneto-crystalline anisotropy, etc. However, typically domain size is $\sim 1\mu$m, and, therefore, magnetic nanoparticles are essentially monodomain particles. The exchange coupling effect, which affects the magnetic ordering of neighboring ferri- or ferromagnetic particles in a non-magnetic host has a range of several nanometers [21]. So, in this we have one of the limiting conditions which in recent years have resulted in an increased attention towards study of nanostructured magnets.

The physical properties observed at such reduced dimensions are strongly sensitive to slight variations of size, shape, and composition. One of the most remarkable magnetic properties that arises in these reduced dimensions is superparamagnetism (SPM), which stands for the paramagnetic-like behavior displayed by single-domain magnetic entities above a characteristic threshold named 'blocking temperature', and is determined by a complex interplay between the intrinsic physical characteristics of the material (magnetic moment, anisotropy, etc.) as also the experimental conditions (measuring time, applied magnetic field, etc.). Giant magneto-resistance in granular magnetic systems [16, 17, 18, 19, 20], departure from metal-like resistivity [16, 19, 20, 22, 23, 24, 25, 26, 27, 28, 29, 30], exchange bias in core-shell type nanoparticles [31, 32, 33], memory effect [34, 35, 36, 37, 38, 39, 40, 41, 42], are some of the other interesting behavior displayed by monodomain magnetic systems. The large number of applications for these nanostructured materials makes the understanding of the physics behind their behavior of practical and fundamental relevance.

1.1 Scientific background and motivation

For many years, Co_xCu_{1-x} ($x \leq 0.3$) alloys have been investigated as a model granular system [19, 20, 43, 44] to study spin-dependent transport processes in metallic alloys containing a fine dispersion of nano-magnetic particles. Hickey *et al.* [45] studied SPM behavior of very small magnetic particles of Co embedded in a matrix of Cu in a melt-spun granular sample of $Co_{0.13}Cu_{0.87}$ and also studied its giant magneto-resistance [46] and magnetization as a function of magnetic field. In electro-deposited binary alloys of Co and Cu, Fedosyuk *et al.* [47] analyzed the distribution of magnetic Co-rich clusters in the nonmagnetic Cu-rich matrix. They also studied the interactions between the magnetic particles [48, 49, 50, 51] and magnetoresistance [47] in such a system. Allia et al. [52] studied melt-spun CoCu ribbons and showed that the classical superparamagnetic model failed to coherently account for the results of a systematic study of isothermal magnetization curves measured at different temperatures, and the concept of 'interacting superparamagnet' had to be applied. Electro- and magneto-transport properties of $Co_{0.1}Cu_{0.9}$ and $Co_{0.15}Cu_{0.85}$ melt-spun ribbons were studied by Fabietti *et al.* [24]. Panissod *et al.* [53] studied granular $Co_{0.1}Cu_{0.9}$ alloys and analyzed behavior of the thermoremanent magnetization (TRM), which provided relevant information about the distribution of blocking temperatures within the samples [54] clearly revealing the existence of three different phases. Childress and Chien [55] presented results on the magnetic properties of metastable fcc Co_xCu_{1-x} alloys in a wide composition range $0 \leq x \leq 0.80$.

The study of memory effect is another very interesting phenomenon in grounds of potential technological applications in magnetic memories, spin electronics, and magnetic sensors etc. Different groups studied memory effect in interacting and non-interacting superparamagnetic nanoparticle systems [34, 36, 37, 38, 39, 40]. The magnetism of a system of nanoparticles strongly depends on the particle size distribution and interparticle

interactions [56, 57]. Therefore, at any temperature below the largest significant blocking temperature, the response to a change in the magnetic field or temperature is slower for the larger particles in the ensemble than that for smaller particles. It has been shown [38] that such a behavior gives rise to interesting effects of aging in situations of either decrease or increase of magnetic field or temperature, the so-called memory effect, even in a system of non-interacting magnetic nanoparticles [34, 35].

The systematic experiments on the magnetic memory effect was pioneered by Sun *et al.* [36] and they explained the observations by considering dipolar interaction between nanoparticles. Zheng *et al.* [35, 58] reported a similar memory effect in what was initially thought to be a system of non-interacting Co nanoparticles dispersed in hexane solution, but later on, was proved to be an interacting system. Sasaki *et al.* [34, 59] finally showed that the same memory effect as studied by Sun *et al.* could be obtained in an isolated nanoparticle system also. Memory effects have been observed in different magnetic systems mostly at temperatures far below the room temperature [34, 35, 36, 37, 38, 39, 40, 41, 42]. Only rarely systems show memory effect near room temperature [60, 61].

Initially, the exchange bias effect was observed in systems having interface of two materials with different magnetic histories like FM and AFM (FM Co/AFM CoO nanostructures), as described by Meiklejohn in a review [62]. Later on exchange bias effect has been observed in different types of systems having interface of combinations between FM, AFM, canted AFM, FIM, SG and disordered magnetic components [63, 64, 65, 66, 67, 68, 69, 70, 71, 72, 73, 74, 75, 76]. Exchange bias effects have been observed in core-shell type nanostructured system where core and shell have different magnetic histories [76]. Exchange bias effects were also studied in binary alloy systems such as NiMn [77, 78, 79, 80, 81], CuMn [79], AgMn [82], CoMn [83] and FeMn [80] alloys.

Historically Kondo effect was observed in dilute magnetic alloy systems in which the host noble metals contained isolated atoms of 3*d* magnetic elements at concentrations

of 0.1% or less [25, 84, 85, 86, 87, 88]. Afterwards Kondo-like resistivity behavior, *i.e.*, a low temperature upturn in resistivity was obtained in metal alloys in which the magnetic elements were present in much higher concentrations. $Au_{1-x}Ni_x$ and $Cu_{1-x}Ni_x$ ($x \sim 0.30 - 0.45$) alloy system showed resistivity minimum in low temperature which too were be explained by Kondo effect [89, 90]. A dilute spin cluster model was used to explain the resistivity minima at these concentration of localized moments. According to this model, two kinds of electron-electron interactions are considered, *viz.*, the $s-d$ exchange interaction (J_{sd}) between localized d electrons in a spin cluster and the conduction electrons, and the $d-d$ exchange interaction (J_{dd}) among localized moments in a cluster. The effect of $s-d$ exchange interaction on resistivity is suppressed by that of phonon scattering at high temperatures, but at low temperatures the $s-d$ interaction dominates. Its strength is nearly independent of local moment concentration. On the other hand, the intracluster interaction J_{dd} strongly depends on the local moment concentration. For $Au_{1-x}Ni_x$ ($x \sim 0.30 - 0.45$), J_{dd} is weak and the clusters behave as independent and Kondo scattering can happen in this Ni content range. When Ni content increases, the average size of Ni spin clusters becomes larger and the distance separating them become shorter. After reaching a critical composition the strength of J_{dd} increases to the level that neighboring clusters begin to align in long-range ferromagnetic ordering. Kondo effect has been extended to systems of dense alloys with rare-earth ions [16, 19, 29, 30], in particular, the intermetallic compounds of Ce and Yb [91, 92, 93, 94, 95, 96, 97]. Very recently, the observation of Kondo effect in melt-spun ribbon of Co_xCu_{1-x} ($x \sim 0.1 - 0.15$) alloys has been reported [23, 24]. Similar observation of Kondo effect has been reported in Co_xCu_{1-x} microwire with $x = 0.05$ [98].

On the other hand, apart from alloys and intermetallics, ceramic samples as also disordered and amorphous alloys [99, 100, 101] exhibit low temperature resistivity upturns which are explained by alternative mechanisms, such as, electron-electron interaction, weak localization effect (due to finite size effect), spin polarized tunneling through grain boundaries [102, 103, 104, 105, 106, 107, 108, 109], etc. Experimentally, the prevalence of

one or other of these mechanisms is manifested through the magnetic field dependence of the resistivity behavior around the temperature (T_{min}) of minimum resistivity.

1.2 Scope of work

In recent years much attention has been paid to the understanding of nanostructured magnetic materials, *e.g.*, nanoparticles, nanowires, multilayers and others, for their application in various fields, such as, miniaturization of electronic devices, high density data storage systems, magnetic fluids, etc. The discovery of giant magnetoresistance (GMR) in magnetic thin films [19, 20, 110, 111] and such effects in small granular systems of Fe, Co, Ni and their various alloys in Cu, Ag or Au matrices [16, 112, 113, 114, 115, 116, 117, 118] have also generated further interest in the study of such binary magnetic systems.

The present thesis describes preparation of Co_xCu_{1-x} nanoparticles with a wide variation of Co concentration ($0.01 \leq x \leq 0.7$) and an appreciable distribution of particle size using a low cost substrate free sample preparation method. We have carried out a systematic study of the temperature, time and cobalt concentration dependent evolution of the magnetization and electrical resistivity of the nanoparticle systems. We have observed an interesting low temperature upturn of electrical resistivity for the first time in concentrated magnetic granular alloy systems.

The main objective of this thesis is to study the changes of magnetic and transport properties of Co_xCu_{1-x} granular alloys with variation of Co concentration. The research work was carried out in three steps, *viz*.,

(i) synthesis of Co_xCu_{1-x} magnetic nanoparticles using chemical reduction method,

(ii) characterization of samples using x-ray diffraction (XRD), transmission elec-

tron microscopy (TEM) and inductively coupled plasma optical emission spectroscopy (ICPOES), and,

(iii) the study of magnetic and transport properties using highly sensitive superconducting quantum interference device vibrating sample magnetometer (SQUID-VSM of Quantum Design) and Physical Properties Measurement System (PPMS of Quantum Design).

1.3 Some basic theories

1.3.1 Superparamagnetism

Superparamagnetic (SPM) system is an assembly of very small single-domain magnetic grains or particles dispersed in some non-magnetic medium and exhibiting magnetic phenomena very similar to atomic paramagnetism. Usually magnetic particles with diameter smaller than 100 nm are called superparamagnetic, though typical SPM particle sizes are of the order of 10 nm. The energy of a magnetic particle generally depends on the equilibrium magnetization direction separated by energy barriers. These energy barriers depend on particle volume and crystalline structure of the material. At any temperature there is a critical diameter below which thermal excitations are sufficient to overcome the energy barrier and to rotate the particle magnetization randomly. The time averaged magnetization of such a particle is zero [119] and this phenomenon is known as superparamagnetism. The SPM behavior of an assembly of granular single domain particles strongly depends on particle volume distribution, types of interparticle interactions, disorder and surface effects, etc. The surface spins are not exactly compensated and in a small particle a small net magnetization arises from the surface spins also [120].

SPM systems show the same behavior as normal paramagnetic materials with one exception, that their magnetic moment is large compared with that of simple paramagnetic systems. The value of magnetic moment per atom or ion for a normal paramagnet is a few bohr magnetons (μ_B). But the moment of a single domain superparamagnetic iron particle with 5 nm diameter is $12000\mu_B$ [121]. Superparamagnet can be described by the same equations that are used for ordinary paramagnetic systems, but the only difference is that a grain or a cluster composed of 1000s of atoms play the role of a single atom as in case of simple paramagnetic system. Basically, single-domain magnetic nanoparticles can be characterized by their large total magnetic supermoment. In the ideal case of noninteracting single domain nanoparticles the dynamics are typically described by the Néel-Brown theory [122, 123, 124], where SPM behavior was predicted at high temperature and the blocked state at low temperature. The temperature which divides this region is blocking temperature (T_B). For small magnetic granules, if the temperature is higher than the average blocking temperature, most of these magnetic granules become SPM. While the temperature is lower than the average blocking temperature, most of these granules become blocked and others still remain SPM. Below T_B superparamagnet's magnetization curve $M(H)$ has hysteresis and is thus more similar to magnetization curve of a ferromagnet. In the following paragraph we introduce the basic characteristics of superparamagnetism.

At any given temperature for which the thermal energy (k_BT) is much lower than the anisotropy energy barrier (K_AV), the magnetization forms an angle θ with the easy axis. In this case the magnetic behavior of an assembly of independent particles is quasi-static, thermal energy being very weak. As the thermal energy increases with increasing temperature, the probability of overcoming the anisotropy energy barrier separating two easy magnetization directions increases. Finally when $k_BT > K_AV$, the magnetization can flip freely among the two easy directions and then its time average of magnetization in absence of an external magnetic field (H) is zero. In such condition the assembly of the particles behave like a simple paramagnetic system and also the coercivity becomes zero.

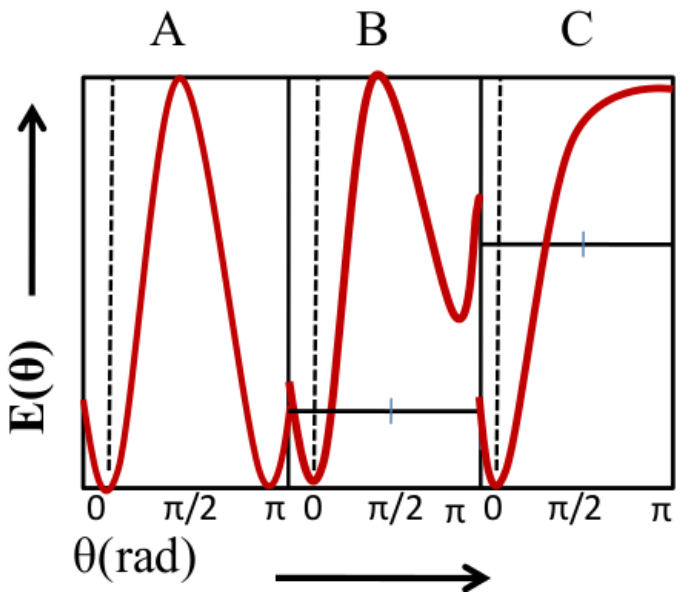

Figure 1.2: *(a) Anisotropy energy ($E(\theta)$) for $H = 0$, (b) for $H < \frac{2K_A}{M_S}$, and, (c) for $H > \frac{2K_A}{M_S}$*

If an external magnetic field (H) is applied parallel to the easy axis, the anisotropy energy of the particle can be written as follows.

$$E_A = K_A V \sin^2\theta - \overrightarrow{m_S}.\overrightarrow{H} \tag{1.9}$$

where, we can define the magnetic moment of a single domain particle,

$$\overrightarrow{m_S} = \overrightarrow{M_S} V \tag{1.10}$$

where M_S is the saturation magnetization and is the volume of the particle. The above equation can be rewritten as,

$$E_A = K_A V \sin^2\theta - M_S V H \cos\theta \tag{1.11}$$

There can be two situations depending upon the value of external field H.

(i) $H < 2K_A/M_S$; there are still two minima but they are not same since the energy barrier from $\theta = 0$ to $\theta = \frac{\pi}{2}$ is higher than that from $\theta = \frac{\pi}{2}$ to $\theta = \pi$ shown in Fig. 1.2, curve B).

(ii) $H > 2K_A/M_S$; there is only one minimum and the SPM relaxation is no longer observed (shown in Fig. 1.2, curve C).

The average time for the switching of the magnetization direction between two easy directions of magnetization is called the SPM relaxation time (τ). For a single domain ferromagnetic particle with uniaxial anisotropy, τ can be written according to Arrhenius law

$$\tau = \tau_0 \exp(\frac{K_A V}{k_B T}) \tag{1.12}$$

where τ_0 is called pre-exponential factor or relaxation time constant [21] and it is considered as the average time between attempts to jump over the energy barrier. In 1949 Neel first evaluated the relaxation time of a superparamagnetic particle and therefore Eq. 1.12 is often called the "Neel relaxation time".

The magnetic behavior of single domain particles is strongly dependent on relaxation time, as expressed in Eq. 1.12. Therefore the magnetic properties of an assemblies of single domain particles depends on the experimental measuring time window (τ_m) of the technique employed to observe the relaxation. In fact if $\tau << \tau_m$, the relaxation appears so fast that a time average of the magnetization is observed as zero and the particles will be in the SPM state. In such conditions an assembly of noninteracting single domain particles do not show magnetic hysteretic behavior (*i.e.*, zero coercivity and remanent magnetization). On the other hand if $\tau >> \tau_m$, the relaxation is so slow that only static properties are observed and the particles will be in the blocked state. In this condition the magnetization as a function of applied field show ferromagnetic behavior with a hysteresis loop. The blocking temperature (T_B) is defined as the temperature at which the relaxation time is equal to the

experimental measuring time.

Let us consider now in more detail some aspects of the magnetic behavior at temperatures higher and lower than the blocking temperature.

Magnetic properties above the blocking temperature

The dependence of the magnetization on the temperature and magnetic field is similar to that of a classical paramagnetic system, using the particle or cluster moment instead of the atomic moment.

$$M(T,H) = M_S L(\frac{\mu H}{k_B T}) \tag{1.13}$$

where M_S is the saturation magnetization, and $L(\frac{\mu H}{k_B T})$ is the classical Langevin function (shown in the Fig. 1.3).

$$L(\frac{\mu H}{k_B T}) = \coth(\frac{\mu H}{k_B T}) - (\frac{k_B T}{\mu H}) \tag{1.14}$$

For $\frac{\mu H}{k_B T}$ « 1 the Langevin function can be approximated with

$$L(\frac{\mu H}{k_B T}) = (\frac{k_B T}{\mu H}) \tag{1.15}$$

as indicated by the line tangential to the curve near the origin (shown in Fig. 1.3).

As the magnetic field is increased ($\frac{\mu H}{k_B T} >> 1$), the magnetization increases. In such condition the Langevin function can be approximated with,

$$L(\frac{\mu H}{k_B T}) = 1 - (\frac{k_B T}{\mu H}) \tag{1.16}$$

Assuming $k_B T >> \mu H$ the susceptibility can be obtained by differentiation of the above Eq. 1.13 with respect to the field H

$$\chi = \frac{V M_S^2}{3 k_B T} \tag{1.17}$$

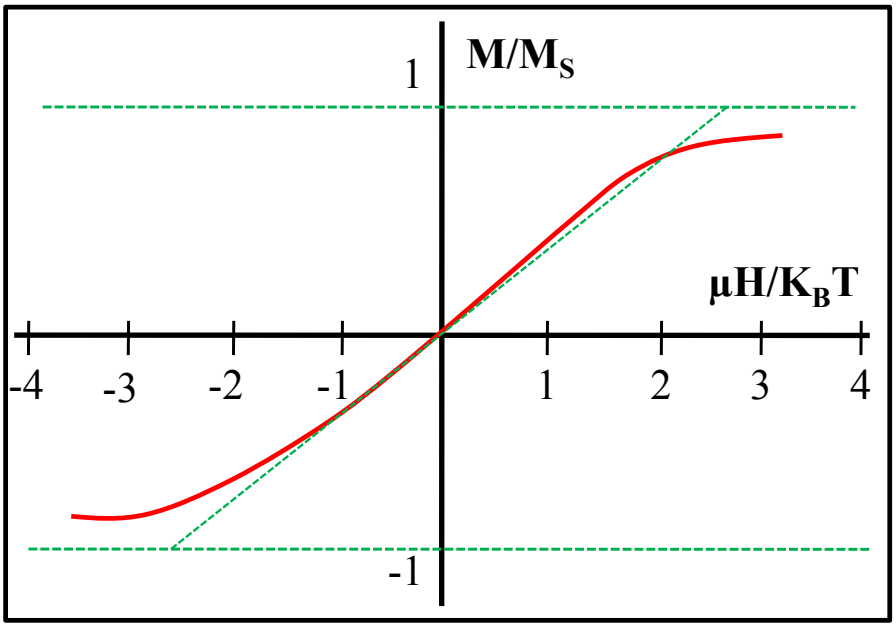

Figure 1.3: *Field dependence of magnetization described by Langevin function*

For a real SPM system in which there is a distribution in particle size and hence in particle volume, Eq. 1.13 can be written as,

$$M(H,T) = M_S \frac{\int_0^2 L(\frac{k_B T}{\mu H}) V f(V) dV}{\int_0^2 V P f(V) dV} \tag{1.18}$$

where *f(V)* is the distribution of particles volume. The more common approach consists in assuming that this size or volume distribution has a certain form. A lognormal distribution is often in good agreement with the particle size distribution obtained experimentally by TEM observations and also determined from the fitting of $M(H,T)$ curves for many kinds of nanoparticle system.

Magnetic properties below the blocking temperature

Below the blocking temperature superparamagnetic nanoparticles show ferromagnetic like hysteretic behavior in the field dependence of magnetization. When a magnetic

field is applied, in the expression of the anisotropy energy the additional term $\cos\theta$ appears. The magnetization can be expressed as

$$M(H,T) = M_S < \cos\theta > \tag{1.19}$$

where θ is the angle between the particle moments and the applied field direction. The magnetization increases with increasing the external field and reaches a maximum value M_S when external applied field is as high as all the moments are aligned along the field direction. When the external field is decreased the magnetization decreases from saturation down to a remanence value when the applied field decreases to zero ($H = 0$). This remanence value is expected to be one half of the saturation value ($M_R = M_S/2$). This picture is valid when all the particles at low temperature are in the blocked state. On increasing the temperature some of the particles will be shifted to the SPM state, thus lowering the remanence value. In a real system, there always exists a distribution in particle size and so also in blocking temperature. Even at the lowest measured temperature a fraction of particles can still be found in SPM state as there exists a smallest volume for which $K_A V$ is always lower than $k_B T$. For this reason the saturation of the magnetization will be partial and M_R value will be lower than $M_S/2$, even at high field.

1.3.2 Single domain particle

According to Weiss [125] theory a ferromagnetic (FM) material contains a number of small magnetic regions, with different shapes and sizes, called magnetic domains. Each domain is a uniformly magnetized region and the local magnetization reaches the saturation value within a domain. The magnetization directions of different domains are at random. So the net magnetization is zero in absence of an external magnetic field. This picture is called the multi-domain structure of a material. In a FM magnetic material, a number of

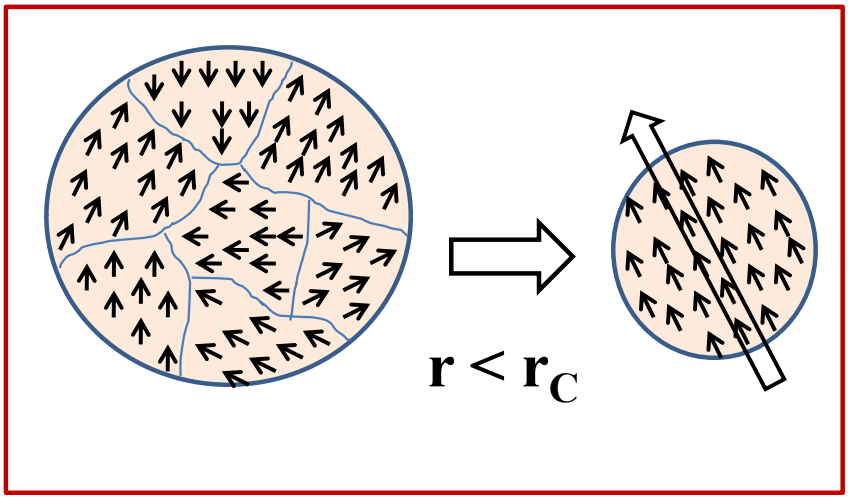

Figure 1.4: *Schematic diagram of prevalence of single-domain structure over multi-domain structure due to size reduction*

magnetic domains exist as a result of the balance between the exchange interaction energy and the magnetostatic interaction energy. Basically exchange interaction energy favors the parallel alignment of neighboring atomic moments and thereby forming magnetic domains and the magnetostatic interaction energy tries to break them into anti-paralleled oriented smaller domains. The domain size is determined by the relative strength of these two energies. With decreasing size of the magnetic particle, there is a critical diameter below which the magnetostatic energy is not sufficient to divide the system into smaller domains with different magnetization directions, and so the system remains as a particle with a single magnetic domain, as illustrated in Fig. 1.4.

As the particle size continues to decrease below the critical size of forming the single domain, the spins increasingly overcome the anisotropy energy barrier and are affected by random thermal fluctuations, and so the system becomes superparamagnetic. The existence of single domain particles were theoretically predicted first by Frenkel and Dorfman [126] and the critical size was estimated by Kittel [127] and others. For a spherical particle, the

critical diameter proposed by Kittel [127] is given below,

$$d_C = 18\frac{E_w}{m_\upsilon M_S^2} \tag{1.20}$$

and

$$E_w = 2\sqrt{(\frac{K_A}{A})} \tag{1.21}$$

E_w is the domain wall energy, m_υ is the magnetic moment for unit volume and M_S is the saturation magnetization. K_A is the anisotropy energy and A the exchange energy density. Typical values of critical diameters of ferromagnetic particles are 15 nm for iron, 70 nm for cobalt, 55 nm for nickel [1].

The coercivity (H_C) depends strongly on the domains size and for multi-domain particle H_C can be written as,

$$H_C = a + \frac{b}{D} \tag{1.22}$$

where a and b are constants and D is the diameter of the domain. From Eq. 1.22 we see that coercivity increases with decreasing domain size which is shown in Fig 1.5, curve A. After that when the particles become single domain then the coercivity reaches a maximum value H_C. Thereafter, H_C decrease with decreasing particle size (Fig. 1.5, curve B) which can be written as,

$$H_C = g - \frac{h}{D^{3/2}} \tag{1.23}$$

where g and h are constants. The decrease of H_C observed in magnetic monodomain systems is due to thermal effects.

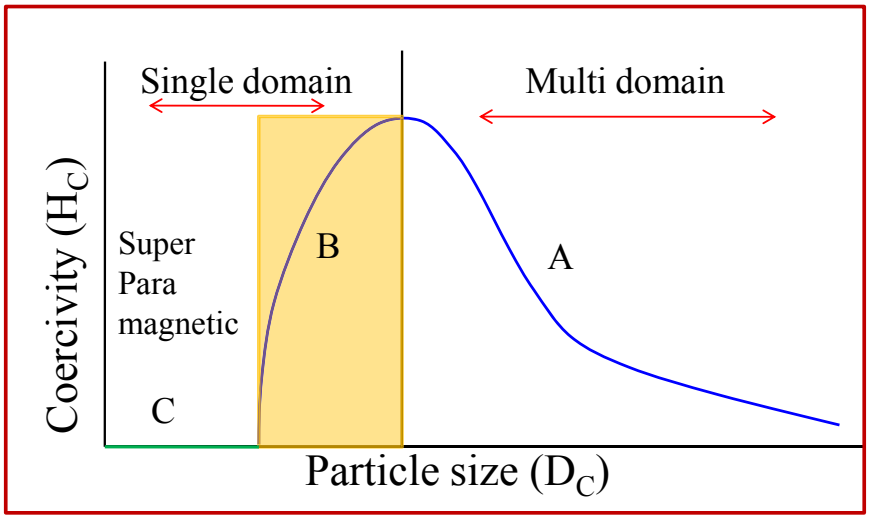

Figure 1.5: *Behavior of the particle size dependence of the coercivity in nanoparticle systems.*

1.3.3 ZFC/FC magnetization curve

ZFC/FC magnetization curve provides valuable information on the temperature and field dependence of a nanostructure. It is easy to estimate different important parameters like blocking temperature and strength of interaction between particles of a single domain nanoparticle sample from the graphs of temperature dependence of magnetization $M(T)$. To draw this curve first the sample is demagnetized at a temperature higher than the blocking temperature where all particle moments are randomly oriented. After that it is cooled in zero external magnetic field down to a temperature much lower than T_B and finally a small field H_m is applied to measure the magnetization in heating cycle from the lowest temperature. The curve thus obtained is called zero-field cooled (ZFC) magnetization. One can obtain a field cooled (FC) curve by following the same process but only the cooling cycle is done in presence of the same small magnetic field (H_m).

In ZFC/FC magnetization processes the temperature evolution of the total magnetization of the system is recorded following different thermomagnetic histories.

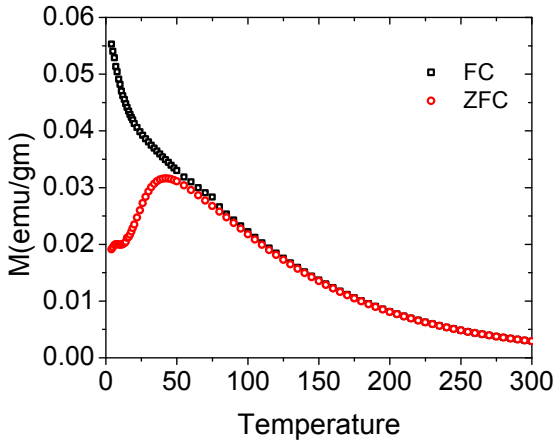

Figure 1.6: *Temperature dependence of magnetization in ZFC and FC protocol of as-prepared Co_xCu_{1-x} nanoparticle for x = 0.03.*

A typical ZFC/FC curves are shown in Fig. 1.6 in which the general behavior of a SPM system is found, *viz*., (i) both curves coincide at high temperatures in a paramagnetic (PM)-like dependence, (ii) with decreasing temperature (T) magnetization in both curves grow until a certain temperature range is reached where the curves start to bifurcate, (iii) the FC curve still growing when the temperature is below the bifurcation, and (iv) the ZFC exhibiting a maximum and then decreasing as temperature is lowered. This broad maximum of the ZFC curve is defined as blocking temperature (T_B). This maximum roughly differentiates two main temperature regimes; at high temperature (above T_B) where the sample exhibits a PM-like behavior in temperature dependence and at low temperature regime (below T_B) where the particles are blocked. However, a close view of the curve reveals that a PM-like decrease right above T_B is not observed in the ZFC curve, and there is a slight difference between ZFC and FC curves. These features indicate that a true SPM behavior is not exhibited right above the maximum of ZFC, but at higher temperatures at which the ZFC curve perfectly overlaps with the FC one and exhibits well defined PM-like temperature dependence. This temperature at which ZFC/FC curves exactly overlap is called bifurcation temperature (T_P) which is slightly higher than T_B. In practice, there is a distribution in particle size in all real SPM systems and this is the reason why the

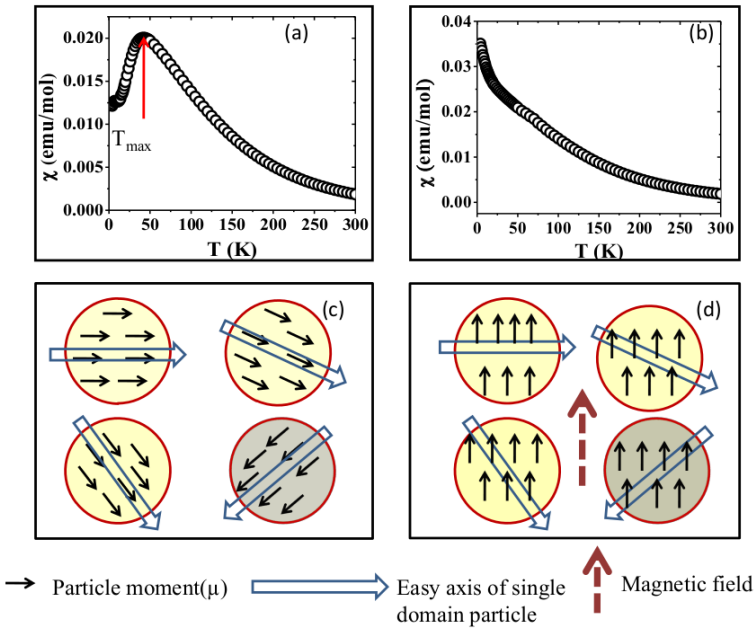

Figure 1.7: *(a) Magnetic susceptibility (χ) in ZFC protocol of Co_xCu_{1-x} nanoparticles for x = 0.03, (b) χ in FC protocol of the same sample, (c) Random orientation of nanoparticles after cooling in ZFC process, (d) random orientation of nanoparticles after cooling in FC process.*

ideal SPM behavior is not observed right at T_B. When the nanoparticles are cooled below the blocking temperature without magnetic field, all the net magnetic moments in single domain particles point along their respective easy axes. Magnetic anisotropy dominate the thermal energy in this region and acts as an energy barrier to switching the magnetization direction from the easy axis. The particle size distribution introduces a random distribution of the easy axes directions also, and the average magnetization, as well as the susceptibility, is about zero [128] or a very low value in this low temperature region. When temperature rises, the particles gain some thermal energy and try to overcome the the magnetic anisotropy barrier. The magnetization directions of these thermally activated nanoparticles start to align themselves along the applied magnetic field direction. Therefore, the total magnetization initially increases in ZFC magnetization with increasing temperature. With increasing influence of thermal randomization, the ZFC curve exhibits a maximum (shown in Fig. 1.7(a) and (c)) and the corresponding temperature (T_{max}) is, for non interacting

particles, directly proportional to the average blocking temperature.

$$T_{max} = \beta < T_B > \tag{1.24}$$

where β is a proportionality constant that depends on the type of size distribution. In the literature, it has been reported that, for a random assembly of non-interacting nanoparticles, β is typically within 1.5-2.0. T_{max} can be related to the blocking of particles having the mean particle size [129, 130].

The FC protocol consists in cooling the sample in a small *dc* magnetic field and measuring the magnetization during the heating cycle in presence of this field. As the nanoparticles are cooled at progressively lower temperature in presence of field, the magnetization of each particle is frozen along the field direction and (Fig. 1.7(b) and (d)) [128] blocked in this condition. During heating a number of particles gain thermal energy and randomize their magnetization directions. The number of particles in SPM state starts to increase and the magnetization monotonically decrease with increasing temperature.

When the temperature is sufficiently increased the system shows a typical paramagnetic behavior (Fig. 1.6) and ZFC and FC curves are superimposed. Below a given temperature the two curves diverge and an irreversible magnetic behavior is observed. The temperature at which the irreversibility is observed is called irreversibility or bifurcation temperature as previously defined (T_P) and can be related to the blocking temperature of the biggest particles [131, 132]. The difference between T_{max} and T_{irr} provides a qualitative measure of the width of blocking distribution (*i.e.*, of the size distribution in absence of interparticle interactions).

1.3.4 Thermal relaxation and blocking temperature

The thermal energy of the single domain particle results in the fluctuation of the magnetic moments. As stated above, the relaxation time of magnetization of these type of systems is a function of the energy barrier and the temperature, and can be described by Arrhenius law (Eq. 1.12). In this equation, τ_0 is the pre-exponential factor inverse of the jump attempt frequency of the particle magnetic moment between the opposite directions of the magnetization easy axis. τ_0 directly depends on the material parameters and can have values ranging between $10^{-10} - 10^{-9}$ s that can be theoretically calculated and experimentally determined [121, 133, 134]. In granular systems the observed magnetic behavior strongly depends on the characteristic measurment time τ_m (the time window) of the employed experimental technique with respect to the intrinsic system relaxation time τ, associated with the energy barrier. This time window varies from large values, as in magnetization measurements (typically 100 s) to very small ones, like in Mössbauer spectroscopy (10^{-8} s). If $\tau_m \gg \tau$, the relaxation is faster than the time window of observation of magnetization, allowing the system to reach thermodynamic equilibrium. The nanoparticles are considered to be in the superparamagnetic regime. On the other hand, if $\tau_m \ll \tau$, the system relaxation proceeds very slowly, and one can observe quasi-static properties as in ordered magnetic systems. Such nanoparticles are in the so-called blocked regime. The blocking temperature T_B that divides both regimes depends on τ_m and is determined for particles with $\tau \sim \tau_m$). T_B is associated to the energy barrier, and for this reason it increases when the particle size increases. Let us define a critical volume V_{crit} at a certain constant temperature T_0, which would lead to $\tau_m = \tau$ in Eq. 1.12.

$$\ln \tau = \ln \tau_0 + \left(\frac{K_A V_{crit}}{k_B T_0}\right) \tag{1.25}$$

Therefore, for $\tau_m = 100$ s (a typical measurement time for conventional magnetome-

try). One has,

$$\ln(10^2) = \ln(10^{-9}) + \frac{K_A V_{crit}}{k_B T_0} \tag{1.26}$$

$$4.65 + 20.7 = \frac{K_A V_{crit}}{k_B T_0} \tag{1.27}$$

$$25 = \frac{K_A V_{crit}}{k_B T_0} \tag{1.28}$$

$$V_{crit} = \frac{25 k_B T_0}{K_A} \tag{1.29}$$

The critical volume at which a particle becomes superparamagnetic is directly proportional to the temperature. In a real SPM system where there always exists a particle size distribution, the bigger particles become superparamagnetic at higher temperatures.

Blocking temperature can be defined for a given measuring time $\tau_m = \tau$ and for a certain fixed volume $V = V_0$ by the equation below

$$\ln \tau = \ln \tau_0 + (\frac{K_A V_0}{k_B T}) \tag{1.30}$$

For $\tau_m = 100$ s one obtains the well-known result,

$$T_B = \frac{K_A V_0}{25 k_B} \tag{1.31}$$

From above discussion we see that T_B strongly depends on τ_m and hence the magnetic response of the system also depends on τ_m of specific measurement and application. As for example, for data storage purposes large time scales are necessary, but short times are

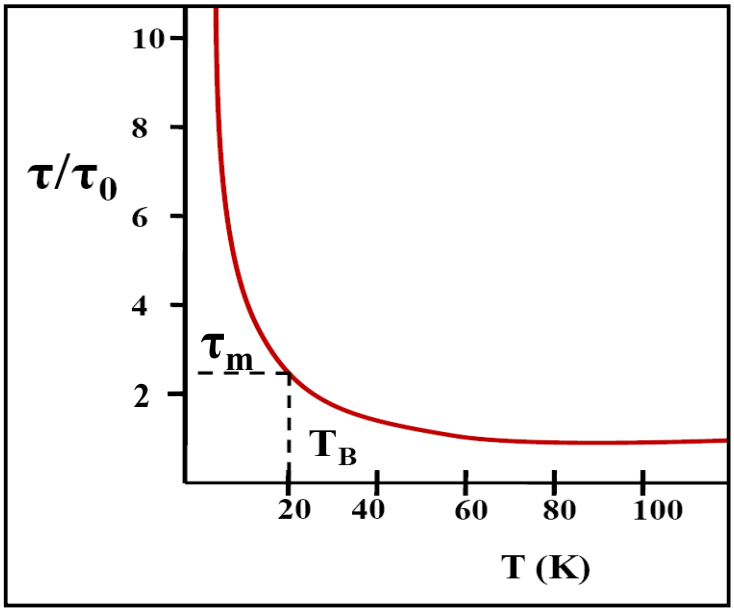

Figure 1.8: *Temperature dependence of relaxation time of superparamagnetic nanoparticles and blocking temperature (T_B) for a certain τ_m.*

required for magnetic recording. So, the experimental techniques are chosen depending upon the objective of application. A typical temperature dependence of relaxation time is shown in the Fig 1.8.

1.3.5 Thermo-remanent magnetization

Thermoremanent magnetization (TRM) is a key parameter providing information about the superparamagnetic relaxation and anisotropy energy barrier. In TRM measurement first saturation field for specific sample is applied at a temperature higher than T_B. After that the sample is cooled down to a lower temperature than T_B and the field is turned off. After 100 sec waiting the magnetization is measured as a function of temperature in warming cycle. After cooling at the presence of saturation field nanoparticles are blocked in the applied field direction. After reaching the lowest temperature though the magnetic field is switched off but the anisotropy energy barrier blocked any change of

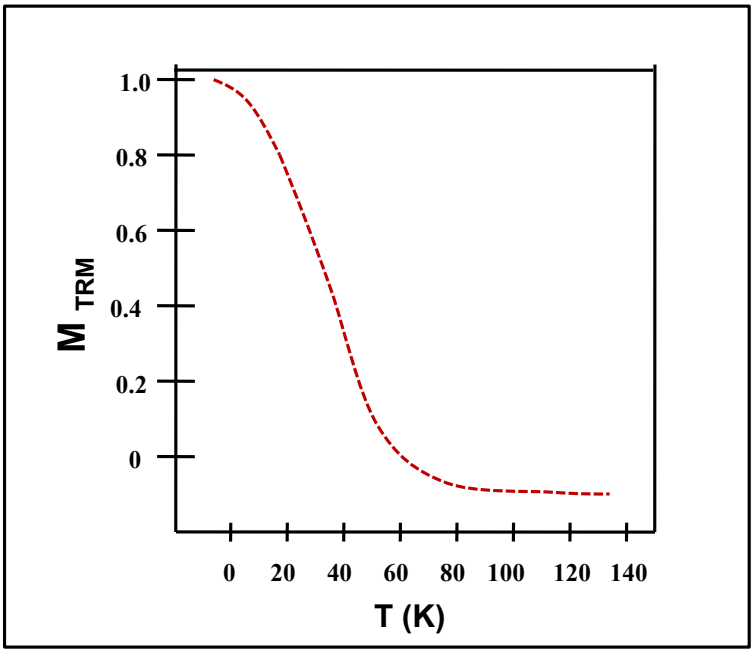

Figure 1.9: *A typical temperature dependent thermo-remanent magnetization curve (dashed line) of superparamagnetic nanoparticle system.*

magnetization direction of the nanoparticles. For random size distribution of nanoparticles and distributions of the angles between easy axis usually anisotropy energy barriers have a broad distribution [128]. As the temperature increases, some of the nanoparticles are able to move their magnetization direction from the blocked condition as they gain some thermal energy (k_BT). As the process is continued, number of thermally activated nanoparticles increases with temperature. This thermally activated nanoparticles randomly flip their magnetization direction faster than the measuring time taken by the magnetometer [130]. For a ideally non-intercaing superparamagnetic system TRM can be written as,

$$\frac{M_{TRM}}{M_S} = 0 + \int_T^{\infty} \gamma f(T_B) dT_B, \tag{1.32}$$

There is no contribution of any susceptibility, as the applied field during the measurement is zero. So that the remanent magnetization is simply the magnetization of the blocked particles. where the factor γ is a constant and equal to 0.5 in the case of uniaxial anisotropy

[52, 135] and 0.886 for cubic anisotropy. Figure 1.9 shows a typical thermo-remanent magnetization curve of superparamagnetic nanoparticle system.

1.3.6 Magnetic anisotropy

In a magnetically ordered material, there are certain preferred orientations of direction of the magnetization. These easy directions are given by the minima in the magnetic anisotropy energy. Magnetic anisotropy energy is combination of several contributions like magnetocrystalline and magnetostatic energies [136, 137] in bulk materials. In single domain particles, other kinds of anisotropy like exchange and dipolar anisotropy, surface anisotropy, stress anisotropy contribute to the total anisotropy energy. Magnetic anisotropy appears due to the finite size of the particles, which are made up of several atoms (usually up to thousands of atoms for single-domain particles), and in these particles the spin-orbit coupling and dipolar interaction control the orientation of easy magnetization direction. The magnetic anisotropy energy E_A (Eq. 1.11) of the particles can be described by a simple model with two main contributions, crystalline anisotropy and shape anisotropy, which are primarily associated to the core and surface atoms, respectively. Figure 1.10(a) show the direction of easy axis, applied magnetic field and the of the moments of the fine particles and Fig 1.1(b) the angular dependence of the energy barrier for zero external magnetic field and for an externally applied field lower than the coercive field.

Magnetocrystalline anisotropy The origin of this contribution is the spin-orbit coupling, which results from the interaction between magnetic moments and is determined by the crystal structure of the system. This is an intrinsic property of the material, and related to the crystal symmetry and arrangement of atoms in the crystal lattice. The orbital wave function will reflect the symmetry of the crystal lattice and the spins will be affected by the anisotropy due to the interaction of orbital wave function with spin, *i.e.*, the spin-orbit

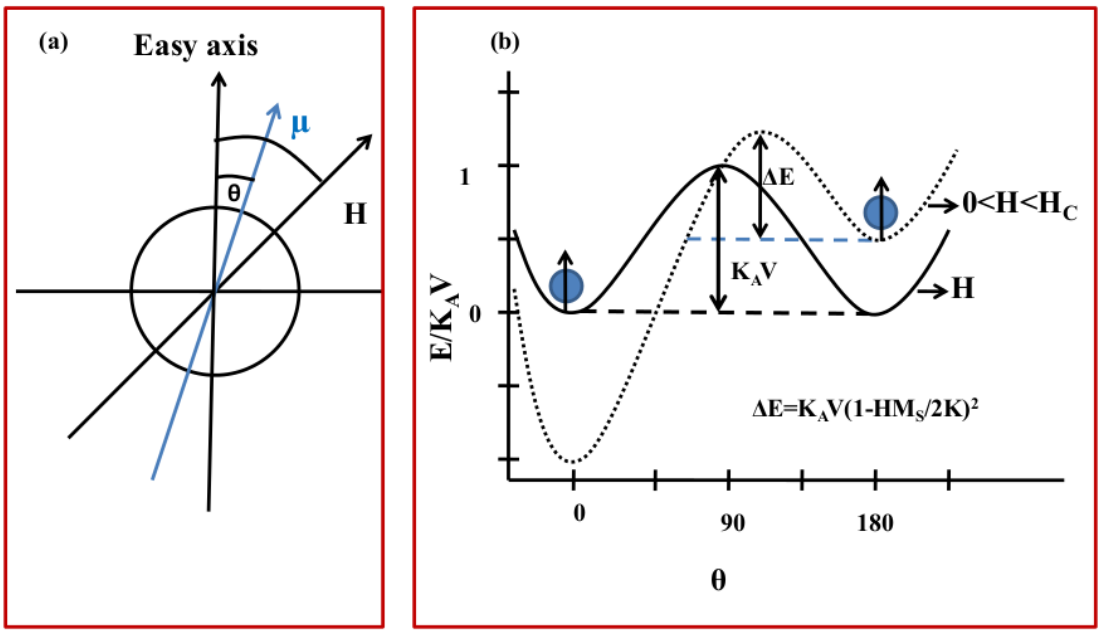

Figure 1.10: *(a) Easy axis, applied magnetic field direction and the direction of the moments of the fine particles, (b) the angular dependence of the energy barrier for zero external magnetic field (continuous line) and for an externally applied field lower than the coercive field (dashed line).*

coupling.

Shape anisotropy If the sample is exactly spherical the same field will magnetize it to the same extent in every direction. But if the sample is not spherical, then it will be easier to magnetize it along a long axis. This phenomenon is known as shape anisotropy. A magnetized body will produce magnetic charges or poles at the surface. Another magnetic field builds up in the magnetized body resulting from this surface charge distribution. It is called the demagnetizing field because it acts in opposition to the magnetization that produces it. Shape anisotropy results from this demagnetizing field. The demagnetizing field will be less if the magnetization is along the long axis than if is along one of the short axes. This produces an easy axis of magnetization along the long axis. A sphere, on the other hand, has no shape anisotropy. The magnitude of shape anisotropy is dependent

on the saturation magnetization. For smaller particle shape anisotropy is the dominant form of anisotropy but in larger sized particles, shape anisotropy is less important than magnetocrystalline anisotropy.

Surface anisotropy The surface atoms have a lower symmetry compared to that of atoms within the particle and their influence on the energy of the particle may depend on the orientation of the magnetization. Actually the when size of a magnetic material is reduced to the critical size to form single domain particle the surface spins are uncompensated and frustrated compared with the spins inside the particles. This gives rise to surface anisotropy which may also depend on adsorbed species on the surface.

Stress anisotropy Another contribution to the anisotropy energy comes from magnetostriction, which is coming from the interaction between the mechanical properties and the magnetic properties which is again due to spin-orbit coupling. In 1842 Joule first observed this phenomenon in a specimen magnetized in a given direction. He observed a change in length in that direction. Strain is related to any stress that may be acting on the considered system. So this implies that the anisotropy energy depends on the stressed state of the system.

Exchange and dipolar anisotropy When two particles come together so close that they have a magnetic interaction, which can be either due to magnetic dipole interaction or exchange interaction, leads to an additional contribution in anisotropy energy. In this case, the easy direction is determined by the relative orientation of the two interacting magnetic moments. In most cases, it is assumed that the sum of all contributions to the magnetic anisotropy energy results in an effective uniaxial anisotropy.

1.3.7 Exchange bias

The exchange bias effect is an old phenomenon which was discovered in 1956 by Meiklejohn and Bean. They observed a shift of the magnetic hysteresis loop along the field axis at low temperature when Co/CoO core-shell nanoparticles were cooled in a static magnetic field [138, 139]. Exchange bias effect is the shift of the magnetic hysteresis loop resulting from the pinning effect at the interface between soft and hard magnetic substances. One of the most interesting interfaces for study the exchange bias effect is interface between a ferromagnetic (FM) and an antiferromagnetic (AFM) material. Spin arrangement in a FM/AFM layer at the temperature $T_N < T < T_C$ and at the temperature $T < T_N$ is shown in the Fig 1.11(a) and (b). An example of a simple hysteresis loop at the temperature $T_N < T < T_C$ and such a shifted hysteresis loop at the temperature $T < T_N$ of a material with a FM/AFM layer are sketched in Fig. 1.11(c) and (d). The center of the hysteresis loop is shifted from zero applied magnetic field by an amount H_{EB}, the exchange bias field. There are three different fields used to characterize the bias; the left and right coercive fields, H_{c1} and H_{c2}, and the bias field H_{EB}. In a FM/AFM system, a shifted hysteresis loop can be experimentally obtained below T_N of the AFM material in the following protocol. First, the hysteresis curve is drawn in the ZFC condition. After that a magnetic field is applied at a temperature higher than T_N in order to saturate the ferromagnetic material. The second step is to cool the sample below T_N in the presence of the same magnetic field. Then again hysteresis curve is drawn in this FC condition. The hysteresis loop in FC condition is shifted compared with the loop in ZFC condition. This shift is due to the strong anisotropy and a weak exchange energy coupling between the FM and AFM material.

The macroscopic observation of the hysteresis loop shift due to unidirectional anisotropy of a FM/AFM bilayer can be qualitatively understood by analyzing the microscopic magnetic structure of their common interface. The critical temperature of FM

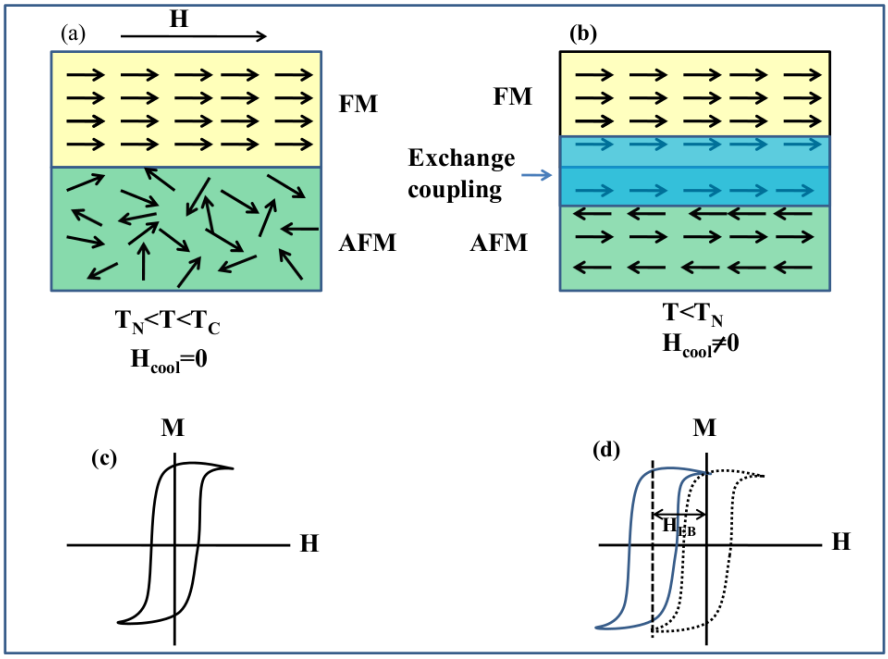

Figure 1.11: *(a) Spin arrangments in a FM/AFM layer at the temperature $T_N < T < T_C$; (b) Spin arrangments in a FM/AFM layer at the temperature $T < T_N$; () hysteresis loop of a material with FM/AFM layer at the temperature $T_N < T < T_C$; (d) a shifted hysteresis loop of a material with FM/AFM layer at the temperature $T < T_N$.*

and AFM layer should satisfy the condition $T_C > T_N$, where T_C is the Curie temperature of the FM layer and T_N is the Neel temperature of the AFM layer. At a temperature $T_N < T < T_C$), the FM spins align along the direction of the applied field, whereas the AFM spins remain randomly oriented in a paramagnetic state. The hysteresis curve of the ferromagnetic material is centered around zero. Next, a high magnetic field is applied which is higher than the saturation field of ferromagnetic layer and then, without changing the applied field, the temperature is being decreased to a finite value lower then T_N (field cooling procedure). After field cooling the system, due to the exchange interaction at the interface, the first monolayer of the AFM layer will align ferromagnetically (or antiferromagetically) to the FM spins. The next monolayer of the antiferromagnet will have to align antiparallel to the previous layer as to complete the AFM order, and so on. Note that the AFM interface spins are uncompensated, leading to a finite net magnetization of this monolayer. It is

assumed that both the ferromagnetic and the antiferromagnetic are in a single domain state and that they will remain single domains during the re-magnetization process. When reversing the field, the FM spins will try to rotate in-plane to the opposite direction. Being coupled to the AFM, which is considered to be rigid, it takes a stronger force and therefore a stronger external field is needed to overcome this coupling and to rotate the ferromagnetic spins. As a result, the first coercive field is higher than the previous one at $T > T_N$, when the FM/AFM interaction was not yet active. On the way back from negative saturation to positive one, the FM spins will need a smaller external force in order to rotate back to the original direction. A torque is acting on the FM spins for all angles except the stable direction which is along the field cooling direction (unidirectional anisotropy). As a result, the magnetization curve is shifted to negative values of the applied field.

1.3.8 Memory effect

In nanoparticle system one interesting behaviors in relaxation dynamics and in ZFC/FC magnetization dynamics is the existence of memory effect. The magnetic state of a system is defined by behavior of temperature dependence, field dependence and time dependence of magnetization of the system. Sometimes it is observed that a magnetic system remembers its magnetic history and repeats its magnetic state after an intermediate change in the temperature or magnetic field. This phenomenon is known as memory effect in superparamagnetic or spin glass like nanoparticle system.

In magnetic nanoparticle systems, there are two possible origins of this memory effect. In non-interacting or weakly interacting nanoparticle system the distribution of particle size which introduces a distribution in relaxation time play the key role in memory effects. Another possible dynamics in an interacting nanoparticle system is frustration caused by strong dipolar interactions among the particles and the randomness in the particle

positions and anisotropy axis orientations.

During the last few years a number of articles on observation of memory effect in nanomagnetic SPM, AFM materials through ZFC/FC magnetization measurements as a function of temperature have been published [34, 36, 37, 38, 39, 40]. Such systems store the memory of either decrease or increase of magnetic field enabling a magnetic *coding* of ”0” and ”1”. Application of a field larger than a critical field erases the memory effect. This behavior can be explained by a wide distribution of grain sizes having different blocking temperatures.

The memory effects in SPM nanoparticle system has be described by Sun *et al.* [36] by using the hierarchical model [140]. In the hierarchical model, there exist numerous valleys (metastable state) at a given temperature (T) on the free-energy surface. Each free energy valley splits and form a new set of sub-valleys with decreasing temperature from T to $T - \triangle T$. When the value of $\triangle T$ is large enough it is impossible to overcome the barriers separating the main valleys during a time t_2. Then the relaxation happens within the new set of sub-valleys. When the temperature is increased back to T these new set of sub-valleys merge with each other and form the previous free-energy picture. Thus the magnetic relaxation is retrieved in its original level after completion of the time t_2. But in temporary heating period, the scenario is different. Here as the temperature is increased from T the magnetic relaxation occurs in a new free energy landscape which is created by the merging of the set of sub-valleys of a lower temperature which is T. When the sample is cooled back to T after the end of heating period t_2, the system is trapped in any one of the set of sub-valleys created in lower temperature T. As a result, the relaxation is not retrieved in its previous level after completion of heating time t_2. Sun *et al.* concluded that the hierarchical model requires a large number of degrees of freedom to be coupled to form a new set of sub-valleys or merging with each other to form a new free energy level. However, independent behavior of the individual particles can not possibly lead to such

coupled states.

But Sasaki *et al.* [34, 59] and Zheng *et al.* [35, 58] studied memory effect following the same experimental protocol of Sun *et al.* in nearly non-interacting nanoparticle systems and obtained similar results. Bandyopadhyay and Dattagupta [38] theoretically reproduced the experimental result of memory effect of paper Sun *et al.* by assuming two state non-interacting SPM models with a particle size distribution. For a nearly non-interacting system the slow dynamic behavior in relaxation mechanism is coming from the broad distribution of particles size.

The magnetic moment of each independent particle relaxes according to its individual anisotropy energy barrier in non-interacting case. The distribution of the size of the particle results in a distribution of energy barriers and blocking temperatures of non-interacting SPM nanoparticle ensemble. As such in non-interacting case, no memory effect should be observed in ZFC process below T_B, as below T_B the probability of occupation of 'up' and 'down' spin of the particles are both same and equal to 0.5 according to two-state model. So, the non-interacting SPM system does not show any difference in the magnetization data with and without intermittent stop during the cooling process. But when there is inter-particle interaction or a spin-glass (SG) like state is present then the case is different. The glassy dynamics is actually the result of interaction between the different clusters below the glassy ordering temperature, T_g. Because of dipolar interaction between the particles the local mean dipolar field is a random variable. As the temperature goes below T_g the system crosses a number of sub-valleys with higher and higher energy barriers, and with progress of time the system goes into deeper energy barrier of the state. Therefore, the energy barrier of the state in which the system is blocked depends on the aging time of the system, and when temperature is low, the consequent higher energy barrier makes the system more reluctant to respond to an applied field.

Therefore in the interacting case, memory effect in ZFC method can be observed

over a temperature range, albeit narrow, below T_g. It can be said that although no true SPM to SG phase transition occurs in the strongly interacting case, a sharp transition from a SPM state towards local domains of stable magnetic moments does occur very close to T_g. We conclude this section by underscoring that simulations based on the simple two-state non-interacting model reproduce all the 'memory effect' in real SPM systems. There is an asymmetric response with respect to negative/positive temperature cycling. This asymmetry is due to the fact that after temporary cooling only smaller nanoparticles are able to respond to the temperature or field change and relax to the new equilibrium state, and the larger nanoparticles are frozen. Upon returning to the initial temperature or field value, the smaller particles rapidly respond to the change such that this new state is essentially the same as that before the temporary cooling, and the larger nanoparticles are now able to resume relaxing to the equilibrium state. This results in a continuation of the magnetic relaxation after the temporary temperature or field change. In contrast, for positive heating, all the particles, smaller as well as bigger, are able to respond to the temperature or field change. Therefore, after returning to the initial temperature, the bigger particles do not respond at all whereas the smaller particles take time to respond, thus leading to no memory effect in the positive heating cycle.

1.3.9 Transport property

Generally, for a metallic system resistivity is a monotonically decreasing function with deceasing temperature. The resistivity of some metals, for example, lead, niobium and aluminium - suddenly drop to zero at a very low temperature and they become superconducting. For ordinary metals resistivity at low temperature becomes temperature independent and reaches a plateau as the inelastic scattering of electrons ceases to exist at low temperature (Fig. 1.12 curve A). Even in noble metals, like copper, silver and gold, resistivity decreases with temperature but even at the lowest accessible temperatures they

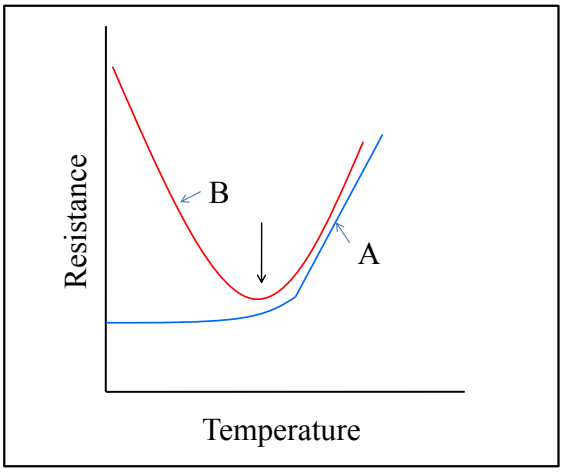

Figure 1.12: *As the temperature of a metal is lowered, its resistance decreases until it saturates at some residual value (A, blue line). In metals that contain a small fraction of magnetic impurities, such as cobalt-in-copper systems, the resistance increases at low temperatures (B, red line) due to the different mechanisms, such as, electron-electron interaction, weak localization effect (due to finite size effect), spin polarized tunneling, Kondo effect.*

have a constant finite resistivity which depends on the intrinsic defects, grain boundaries, impurities etc. This residual resistivity (ρ_0) can be increased by addition of defects externally but the character of the temperature dependence remains the same. In case of nanoparticles, the finite size also contributes to the residual resistivity. The temperature dependent part $\rho(T)$ can arise from various phenomena like electron-phonon interaction, electron-magnon interaction, electron localization (in case of disordered metals at low temperature). For a good non-magnetic metal, the temperature dependence originates from inelastic interactions, such as, electron-electron, electron-phonon, electron-magnon, etc. When magnetic atoms like cobalt or nickel are added, the resistivity in the low temperature region often starts to increase with decrease in temperature rather than saturating at a constant value (Fig. 1.12 curve B). In 1964 Jun Kondo discovered [141, 142] that in dilute magnetic alloy the antiferromagnetic exchange interaction between isolated magnetic moments and conduction electron spin leads to the quenching of local moments and in the expression of resistivity introduces a $-lnT$ term which combined with the positive

electron-phonon contribution leads to the minimum in resistivity. The temperature at which the resistance starts to increase again is often called Kondo temperature. However, in alloys with concentrated magnetic impurities the interpretation of electronic transport properties has always been difficult and controversial. In structurally disordered alloys and metallic glasses the existence of minima in $\rho(T)$ became a very well studied topic [99, 100, 101, 143, 144]. Most of these metallic glasses contain high concentration of $3d$ transition metals, and the upturn in $\rho(T)$ at low temperature follows a $-T^{(1/2)}$ type dependence. It has been established that this functional dependence of $\rho(T)$ arises from disorder induced electron-electron interactions [100, 145]. Apart from alloys and intermetallics, the ceramic samples and other compounds too exhibit low temperature resistivity upturns which are explained by various mechanisms, such as, electron-electron interaction, weak localization effect (due to finite size effect), spin polarized tunneling through grain boundaries [102, 103, 104, 105, 106, 107, 108, 109], etc. In systems where elastic electron-electron interaction is dominant, the temperature dependence of resistivity $\rho(T)$ can be written as,

$$\rho(T) = \rho_0 + \rho_{in} + \rho_{el} \tag{1.33}$$

Usually, ρ_{in} increases with temperature according to a power law $\rho_{in} = b^P$ in which the coefficient $'b'$ does not depend on H, and ρ_{el} depends on temperature as -$aT^{1/2}$.

The role of electron-electron interaction on the electronic properties of pure metal can be described by the Fermi-liquid theory. The elastic scattering of electrons by impurities in metals can substantially modify the electron electron interaction and hence the electronic properties of the system. Two important parameters are elastic momentum relaxation time τ, and the characteristic time $\hbar(k_BT)$ required for two interacting quasi-particles to change their energy by a value of about k_BT. Let τ be small compared to $\hbar(k_BT)$, *i.e.*,

$$\frac{k_BT\tau}{\hbar} << 1 \tag{1.34}$$

In such condition it is favorable for two interacting particles to diffuse coherently before they exchange an energy of about $k_B T$, and they are scattered many times by impurities in their diffusive path. The electrons spend a longer time in a given region of space compared with the plane-wave states in the diffusive regime, and their interaction with the impurities and defects is enhanced. Under this condition 1.28 the motion of electrons during the characteristic time of electronelectron collisions is characterized by the diffusion coefficient (D_{diff})

$$D_{diff} = \frac{v_F^2 \tau}{3} \tag{1.35}$$

where v_F is the Fermi velocity. This electronelectron interaction produces a cusp in the electronic density of states at the Fermi level [146, 147]. The physical reason for such a variation in the density of extended states near the Fermi level is related to the shift of the energy of a particle added into the system due to the Coulomb interaction with electrons of the occupied states. Thus, the nature of the cusp is similar to that of the Coulomb gap appearing at the Fermi level in the region of localized states [148]. This feature produces the anomaly in the low temperature resistivity of disordered systems.

CHAPTER 2

EXPERIMENTAL TECHNIQUES

In this chapter there are three sections. In first section we have discussed the details of sample preparation method which we have used to prepare our binary metallic nanoparticles. The systematic study of structural and chemical characterization of the samples are discussed in the second section. The details of experimental techniques and measurement procedures to study the magnetization and transport behavior are described in the last section.

2.1 Sample preparation technique

There are different methods for nanomaterial preparation, *e.g.*, solid state reaction, sol-gel route, ball milling and electro deposition, etc. Co and Cu are nearly immiscible, and no equilibrium phases exist in the Co-Cu binary phase diagrams. However, the high cooling rate during sample preparation may result in metastable CoCu alloys with extended solubility. For the preparation of magnetic granular alloys with immiscible non-magnetic hosts, many techniques have been used, such as, melt-quenching, evaporation, sputtering,

and mechanical alloying. Some of these techniques are substrate dependent and involve high cost. We have used a low cost substrate free sample preparation method. In this process we have successfully prepared Co-Cu nanoparticles in a wide concentration range of Co(x) $(0.01 \leq x \leq 0.80)$ and with an appreciable distribution of particle size.

Chemical reduction method

CoCu granular nanoparticles were prepared by chemical reduction process using $NaBH_4$ as a reducing agent [149, 150]. For removing oxygen distilled water was boiled for a few minutes, and thereafter the entire wet chemical synthesis process was carried out inside a glove box in flowing N_2 gas. $CoCl_2.6H_2O$ (Alfa Aesar) and $CuCl_2.2H_2O$ (Merck) in required ratios were dissolved in 30 ml aqueous solution as the total metal ion concentration in the solution remained 0.5 M. Cetyltrimethylammonium bromide ($CTAB$) (Sigma) as 0.05 mM in solution was added as a capping agent to prevent further nucleation and oxidation. A 15 ml 2.8 M aqueous solution of $NaBH_4$ (Merck) was poured drop-wise from a burette to the salt solution. The reduction reaction can be expressed as,

$$CoCl_2 + CuCl_2 + NaBH_4 + CTAB \longrightarrow CoCu + NaCl + NaBO_2 + H_20.$$

The solution was continuously stirred by a magnetic stirrer. The reaction was performed in an ice bath to prevent over-heating of the solution and keep it near room temperature. The resulting black precipitate was washed several times with distilled water and finally with acetone. The samples were quickly introduced in a vacuum desiccator to dry at room temperature. For further studies, the samples were pressed into pellets using a KBr pellet die under pressure of 0.33 GPa in a laboratory press. The density of the pellets ranged between 30-50 % of the theoretical value, with a minimum value of 2.7 ± 0.05 g/cc obtained for the Co-0.45 sample. The density was measured geometrically and the figure that we have mentioned is the lowest of four samples. In some rectangular specimens cut

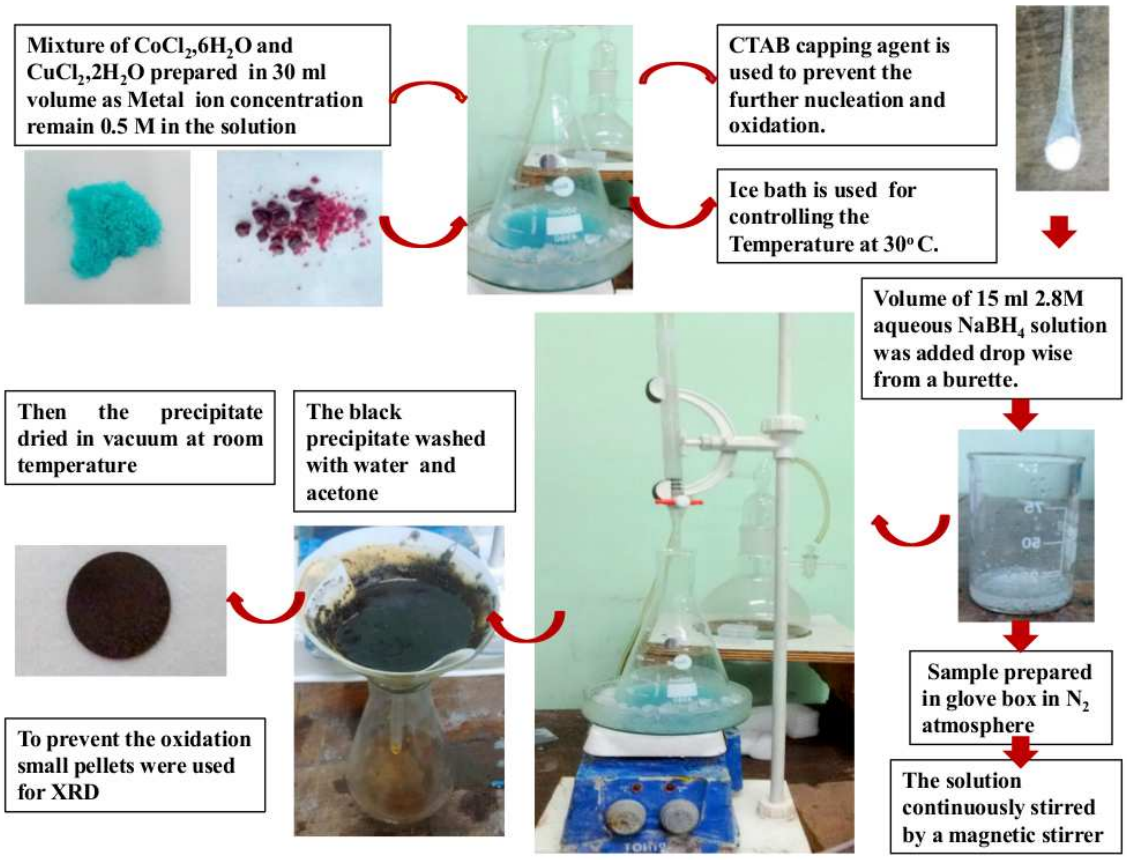

Figure 2.1: *Schemimatic diagram of different steps of sample preparation by chemical reduction method.*

for resistivity measurements, the highest density value was close to 5.7 ± 0.05 g/cc. These values are typical of pellet samples obtained only by cold compaction, without additional compaction by means of thermal treatment [151].

The different steps of the sample preparation process are shown in Fig. 2.1. Experiments were performed on as-prepared and also on annealed samples. A part of the sample pellets were annealed at 200°C for one hour in a reducing atmosphere inside a tube furnace. An admixture of gases 5% hydrogen and 95% nitrogen was flowing through the annealing tube where the sample was placed in a ceramic boat.

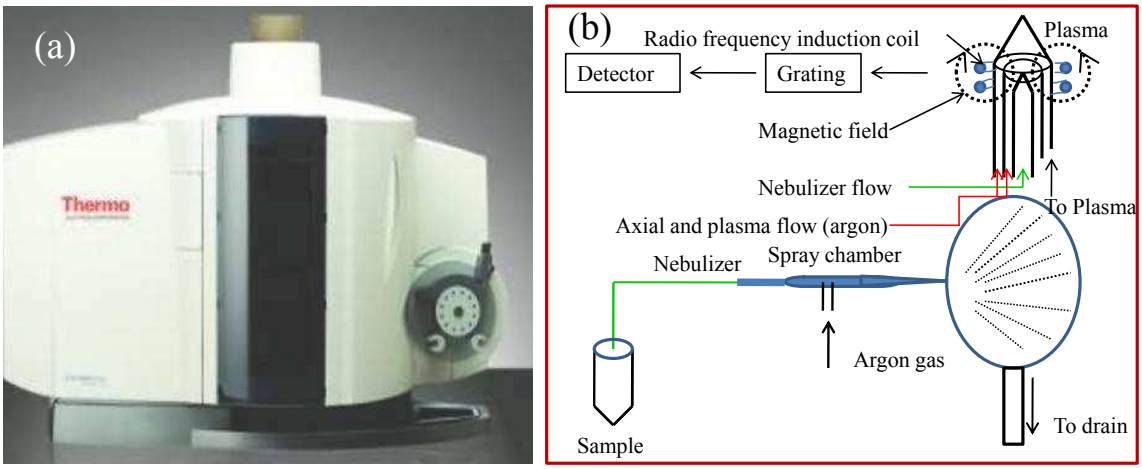

Figure 2.2: *(a) Picture of Thermo Fisher Scientific iCAP-6500 ICPOES used for this thesis, (b) schematic diagram of inductively coupled plasma torch.*

Table 2.1: The desired and actual values obtained from ICPOES studies of average cobalt and copper content in mol %, denoted as Co-D and Co-O, respectively, for cobalt, and Cu-D and Cu-O, respectively, for copper. The samples of batch I are designated Co-0.01 → Co-0.33 in increasing order of Co content.

Sample	Co-D mol %	Co-O mol %	Cu-D mol %	Cu-O mol %
Co-0.01	1	1.11(1)	99	98.89
Co-0.03	3	2.88(1)	97	97.12
Co-0.05	5	5.28(1)	95	94.72
Co-0.08	7	8.27(1)	93	91.93
Co-0.10	10	10.37(1)	90	89.63
Co-0.15	15	14.97(1)	85	85.83
Co-0.21	20	21.22(1)	80	78.78
Co-0.33	30	32.94(1)	70	67.06

2.2 Structural and chemical characterization technique

2.2.1 Inductively coupled plasma optical emission spectroscopy

ICPOES stands for inductively coupled plasma optical emission spectroscopy and is the commonly used technique in modern laboratories to determine the chemical composition of samples. It uses the principles of atomic emission spectroscopy, where

Table 2.2: The desired (D) and actual(O) values obtained from ICPOES studies of average Co and Cu content in mol % in Co_xCu_{1-x} samples of batch II which are designated as Co-*x*.

Sample	Co-D mol%	Co-O mol%	Cu-D mol%	Cu-O mol%
Co-0.01	1	1.20(1)	99	98.8
Co-0.03	3	3.41(1)	97	96.59
Co-0.05	5	5.67(1)	95	94.33
Co-0.08	7	8.02(1)	93	91.18
Co-0.10	10	10.48(1)	90	89.52
Co-0.17	15	17.87(1)	85	82.13
Co-0.32	30	31.96(1)	70	68.04
Co-0.45	40	44.93(1)	60	55.07
Co-0.56	50	56.01(1)	50	43.99
Co-0.76	70	76.73(1)	30	23.27

samples at high temperatures up to 8000 K are converted to free, excited ions and electrons or plasma. The excited atoms or ions emit radiation when they return to ground state. The emitted characteristic radiations and their intensities are recorded by optical detectors. Samples are introduced into the spectrometer as liquids. Solid samples are made into aqueous or acid solutions. Liquid sample goes through different steps when injected to the spectrometer.

The first process called nebulization where sample is converted to a mist of fine droplets called aerosol. In this process the sample is sucked into capillary tube by a high pressure stream of argon gas flowing around the tip of the tube. This pressure breaks the liquid into fine droplets of various sizes in the spray chamber. In the spray chamber, aerosol is separated into large droplets that go to drain, and fine droplets that are carried to form plasma. More than 99% of the injected sample goes to drain and less than 1 % carried to form plasma that is energized by radio-frequency passing through a water-cooled induction coil. Figure 2.2(a) is the picture a ICPOES set-up of Thermo Fisher Scientific iCAP-6500 and (b) is a schematic diagram of typical inductively coupled plasma source called torch.

Ionization of the flowing aerosol mix is initiated by a spark from a Tesla coil. The

electrons stripped from atoms and the resulting electrons then interact with the radio-frequency field produced by the induction coil. This interaction causes the ions and electrons within the coil to flow in closed annular paths causing Ohmic heating. Adding mechanical energy to the electrons/ions by the use of the induced field within the heart of the plasma in this manner is called inductive coupling. The emitted radiation from the plasma are measured by detectors and then used for analysis. The emissions are separated based on their respective characteristic wavelengths and their intensities are measured. The intensities are proportional to the concentrations of elements in the aqueous solutions. First the instrument is standardized with the multi-element calibration standard solution. The sample data are corrected in terms of standardization blanks.

In this work, ICPOES studies were performed with Thermo Fisher Scientific iCAP-6500 on microwave-digested samples in Suprapure HNO_3. The spectrometer was calibrated with NIST-SRM standard at wavelengths 238.8 nm for cobalt and 324.7 and 327.3 nm for copper. For the eight as-prepared Co_xCu_{1-x} samples of the first batch, the desired chemical compositions as in the mixture of $CoCl_2$ and $CuCl_2$ solutions, and the final compositions as obtained from ICPOES measurement on precipitated alloys are given in Table 2.1. The samples are denoted by symbols Co-0.01 $\rightarrow$ Co-0.33 in increasing order of Co content. For the eleven as-prepared Co_xCu_{1-x} samples of the second batch, the desired and final compositions are given in Table 2.2.

2.2.2 Powder x-ray diffraction

X-ray diffraction (XRD) is a non-destructive technique for analyzing a wide range of materials, including fluids, metals, minerals, polymers, plastics. XRD has also become important method to quickly determine the physical properties of materials, to measure the average spacings between layers or rows of atoms, and the crystal structure of an unknown

material. Also XRD is used to study the size, shape and internal stress of small crystalline particles. XRD studies at room temperature were carried out by using RIGAKU TTRAX-III diffractometer (shown in Fig 2.3(a)) at the operating voltage of 60 kV and current 150 mA in Parallel Beam (PB) geometry for the pelletized samples using Cu-K_α radiation. Figure 2.3(b) shows a schematic diagram of the diffractometer using in powder x-ray diffraction. The working principle is that the x-ray beam is scattered from the electron clouds of the individual atoms. When x-ray beam collide with the electrons, some photons will be diffracted away from their original direction. If the atoms are arranged in a periodic fashion, as in crystals, the diffracted waves undergo constructive interference (corresponding to maximum diffraction intensity), and destructive interference (corresponding to minimum diffraction intensity) with the same symmetry as in the distribution of atoms. Thus by measuring the diffraction pattern one can determine the distribution of atoms in a material. Let us consider an incident x-ray beam interacting with the atoms arranged in a periodic manner as shown in the Fig. 2.3(c). The atoms, represented as brown spheres, can be viewed as forming different sets of planes in the crystal. For a given set of lattice planes with an inter-plane distance of d, the condition for constructive interference at its strongest is given by Bragg's law,

$$2d \sin\theta = n\lambda \tag{2.1}$$

where λ is the wave-length of the diffracted x-ray beam, θ is the scattering angle, and n is an integer representing the order of the diffraction maxima. The reflected or diffracted x-ray beam is captured by a sensitive scintillation counter. Powder x-ray diffraction is the most widely used technique for characterizing materials. The term 'powder' means randomly oriented multiple single crystalline particles which is also called a polycrystalline material. The whole diffraction patterns were obtained by varying the incidence angle. Each peak in the x-ray diffraction patterns (2θ versus intensity plot) corresponds to the response of individual crystallographic planes of the material. Below a certain size of particles, there wouldn't be enough number of lattice planes available for the destructive interference to

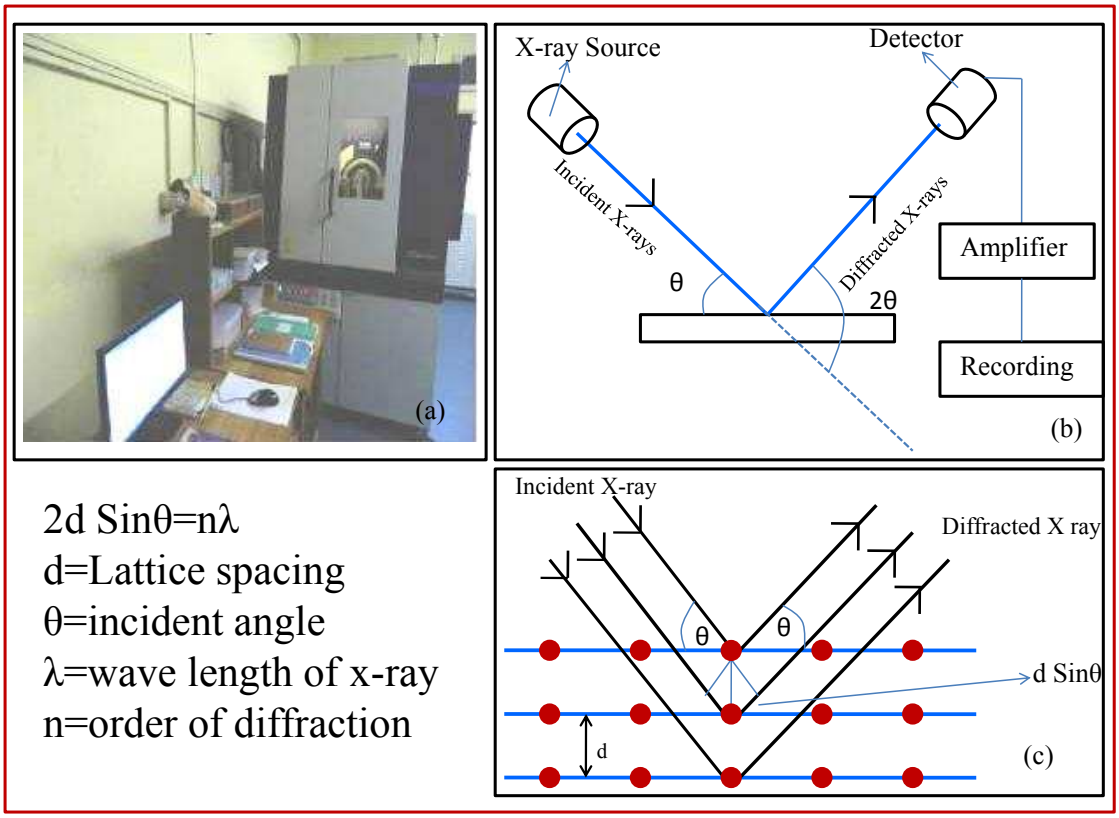

Figure 2.3: *(a)RIGAKU TTRAX-III diffractometer, (b)schematic diagram of a x-ray diffractometer, (c) Bragg diffraction diagram.*

be complete, and this is the primary reason for the size induced broadening of XRD lines.

XRD patterns of the as-prepared alloys Co-0.01 to Co-0.33 and that of commercially obtained Cu powder are shown in the Fig. 2.4. In alloy samples, all the reflections are from *fcc* Cu and none from *hcp* Co even for samples with high Co content, indicating that Co is alloyed in the predominantly Cu matrix [152], and there is no free cobalt. In some of the samples there is a small amount of Cu_2O, as indicated in Fig. 2.4. Compared to bulk Cu powder, the peaks are broadened in Co-*x* indicating small size of the particles. The particle sizes, *D*, are usually calculated from broadening of the diffraction peaks using Scherrer equation,

$$D = \frac{0.9\lambda}{\cos\theta\beta} \tag{2.2}$$

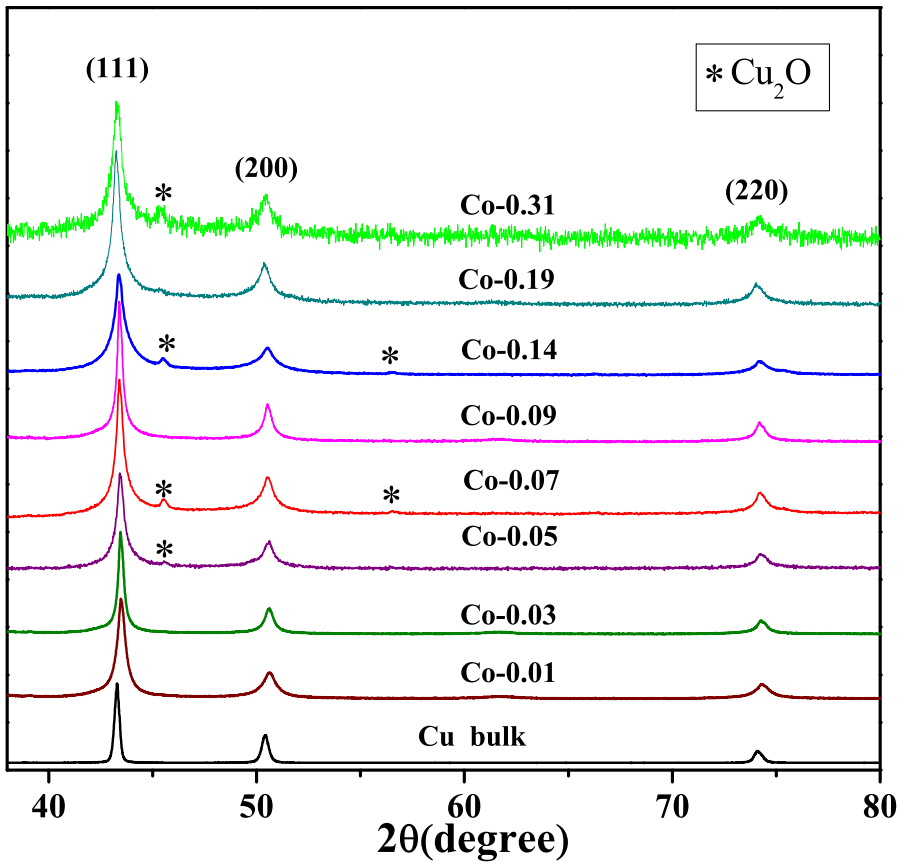

Figure 2.4: Room temperature powder x-ray diffraction patterns of as-prepared Co-*x* samples of the first batch and bulk Cu powder.

where λ is wavelength of the x-ray radiation, β is the FWHM (in radians) and θ is diffraction angle. But the particle sizes calculated using the above equation are different from the three peaks corresponding to the planes (111), (200), and (220). To get the particle size more accurately we have calculated the particle size using Williamson-Hall method. The principle of this plotting method is that the size broadening, β_D, and strain broadening, β_ε, vary quite differently with respect to Bragg angle, θ. One contribution varies as $1/\cos\theta$ and the other as $\tan\theta$.

$$\beta_D = \frac{K\lambda}{D\cos\theta}$$

$$\beta_\varepsilon = C\varepsilon\tan\theta$$

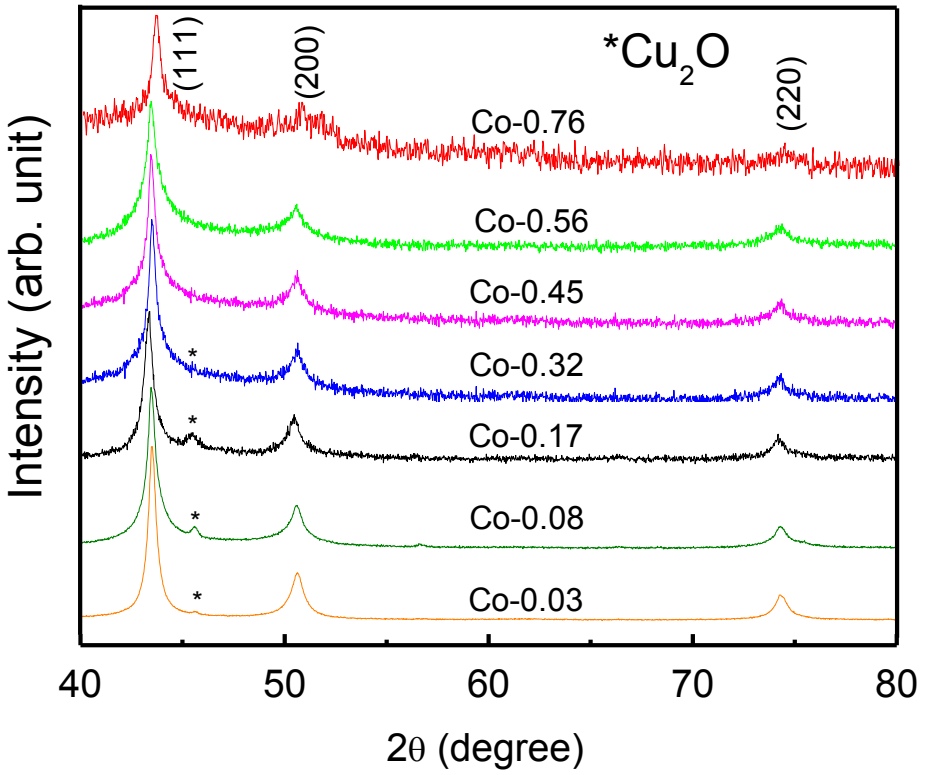

Figure 2.5: Room temperature powder x-ray diffraction pattern of Co-*x* samples of second batch.

If both contributions are present then their combined effect should be determined by convolution. The simplification of Williamson and Hall is to assume the convolution is either a simple sum or sum of squares (leading to Lorentzian and Gaussian diffraction lines, respectively). Here we use the sum of squares because our peaks are Gaussian in nature. Using this we get,

$$\beta^2 = \beta_e^2 + \beta_L^2$$

$$\beta^2 = (C\varepsilon \tan\theta)^2 + (\frac{K\lambda}{D\cos\theta})^2$$

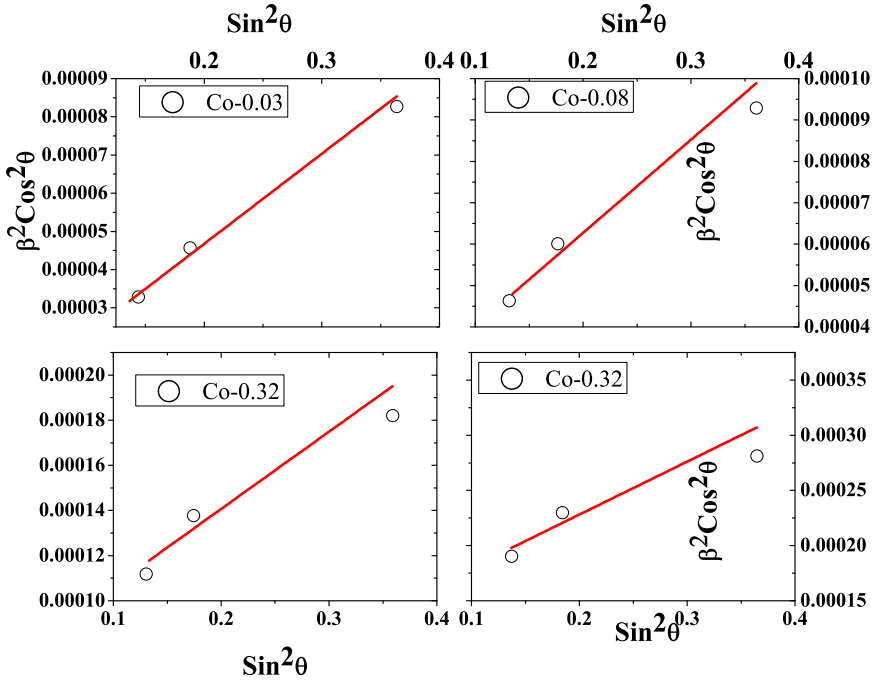

Figure 2.6: Williamson Hall plots of Co-0.03, Co-0.08, Co-0.17 and Co-0.32 samples.

If we multiply this equation by $(\cos\theta)^2$ we get:

$$\beta^2 \cos\theta^2 = (C\varepsilon \sin\theta)^2 + (\frac{K\lambda}{D})^2 \tag{2.3}$$

and comparing this to the standard equation for a straight line (m = slope; c = intercept).

$$y = mx + c \tag{2.4}$$

From the linear plot of $(\beta\cos\theta)^2$ versus $(\sin\theta)^2$ we obtain the particle size (D) from the intercept $(K\lambda/D)^2$. Williamson Hall plots and straight line fitting of sample Co-0.03, Co-0.08, Co-0.17 and Co-0.32 are shown in the Fig 2.6.

The XRD pattern of the second batch samples are shown in Fig. 2.5, where it is compared with that of 50 micron Cu powder which has diffraction lines from its *fcc* structure. Some of these samples have high Co content. Usually *hcp* cobalt is

Table 2.3: The values of Bragg's angles, average particle sizes (D from XRD) calculated from x-ray diffraction, lattice spacing (d in nm) and lattice parameter (a in nm) in Co_xCu_{1-x} samples of the first batch which are denoted as Co-x.

Sample Co-x	2θ degree	2θ degree	2θ degree	D (from XRD) (nm)	d (nm)	a (nm)
Co-0.01	42.77	49.90	73.62	20	1.729	0.361
Co-0.03	42.86	50.22	73.70	45	1.724	0.362
Co-0.05	42.25	50.56	74.29	20	1.731	0.362
Co-0.08	43.40	50.48	74.26	20	1.724	0.362
Co-0.10	43.01	50.14	73.82	44	1.730	0.362
Co-0.15	43.5	50.52	74.27	16	1.720	0.360
Co-0.21	42.96	50.06	73.78	21	1.730	0.362
Co-0.33	43.30	50.44	74.14	18	1.722	0.361

obtained at room temperature. In XRD with CuK_α radiation, cobalt yields high x-ray fluorescence. However, even using fluorescence suppression technique, no separate Co lines were obtained in XRD pattern. It may be noted that Co in its fcc form has lattice parameters very close to those of Cu. For pure fcc cobalt lattice parameter a is 0.356 nm and for pure copper a is 0.361 nm. In our CoCu alloy the average lattice parameter value is 0.361 nm which is very close fcc copper. Bragg's angles, lattice spacings and lattice parameters value obtained from the powder x-ray diffraction data shown in Tables 2.3 and 2.4. It is clear that there is no regular variation of lattice parameters or particles size with Co content. Average particles size calculated from the broadening of the XRD peaks using Williamson-Hall method are given in Table 2.4. Though the entire sample preparation procedure was carried out under inert gas and reducing atmosphere, some amount of oxidation during transfer of samples could not be avoided. The analysis of XRD data (Fig. 2.5) showed that some of the low cobalt containing samples had Cu_2O not exceeding 5% of the sample volume. Higher cobalt containing samples were comparatively free of oxidation.

Table 2.4: The values of Bragg's angles, average particle sizes (D from XRD) calculated from x-ray diffraction, lattice spacing (d in nm) and lattice parameter (a in nm) in Co_xCu_{1-x} samples of the second batch which are denoted as Co-x.

Sample Co-x	2θ degree	2θ degree	2θ degree	D (from XRD) (nm)	d (nm)	a (nm)
Co-0.01	43.51	50.61	74.33	12	1.717	0.361
Co-0.03	43.30	50.42	74.18	13	1.724	0.361
Co-0.05	43.29	50.40	74.18	13	1.724	0.362
Co-0.08	43.49	50.55	74.3	15	1.724	0.362
Co-0.10	43.39	50.55	74.3	14	1.721	0.361
Co-0.17	43.47	50.55	74.31	16	1.719	0.360
Co-0.32	43.34	51.94	74.28	12	1.721	0.361
Co-0.45	43.44	50.47	74.22	14	1.720	0.362
Co-0.56	43.64	50.67	74.44	10	1.727	0.362
Co-0.76	43.44	49.89	74.22	12	1.718	0.361

2.2.3 Transmission electron microscopy

The transmission electron microscopy technique is widely used to study the average particle size, size distribution and morphology of the nanoparticles. In particle size measurement, microscopy is the only method in which the individual particles are directly observed and measured. In the microscopy techniques the wave nature of the rapidly moving electron is utilized. The electrons were accelerate by anode voltage to the order of few hundred kV and the associated wavelength is less than 1Å. All the TEM investigation required in this work were carried out using FEI, Tecnai20 machine operating at 200 kV using embedded CCD camera having 0.24 nm resolution. Picture of FEI Tecnai20 (200 kV) transmission electron microscope and the basic working principle of the TEM is schematically shown in Fig. 2.7(a) and (b). Here the stream of monochromatic electrons, produced by the electron gun is focussed to a thin, small and coherent beam with the help of the two condenser lenses. The focused beam is partially transmitted after the strike the specimen. The image is formed by focussing the transmitted portion through the objective lens. This image is further magnified when it is passed through the intermediate and

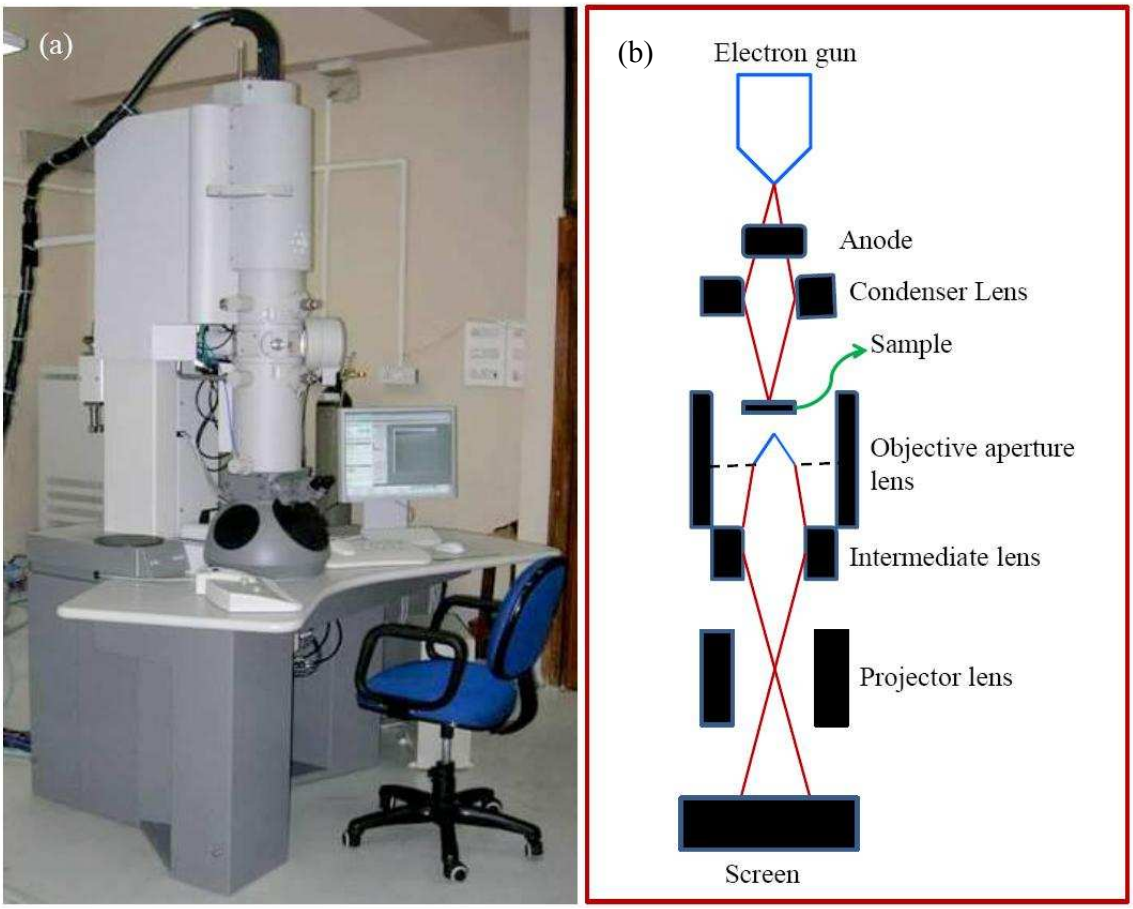

Figure 2.7: *(a) Picture of high resolution FEI, Tecnai20 (200 KeV) transmission electron microscope, (b) schematic diagram of transmission electron microscope*

projector lenses.

To prepare for the measurement, the sample was first dispersed in alcohol and a drop of the dispersed sample was put on a carbon-coated copper grid which was then thoroughly dried in vacuum before being inserted in the microscope for scanning. Besides morphology, high resolution TEM (HRTEM) was used for direct atomic level study like lattice fringes. Image-J software was used for the detail analysis of particle size from TEM micrographs. However, for every sample, the result was verified by manual measurements, *i.e.*, by placing a semi-transparent millimeter scale graph paper on printouts of TEM images. For samples that yielded an appreciable number of isolated particles in the micrographs, the diameters were plotted as histograms. The size distributions thus obtained were fitted with

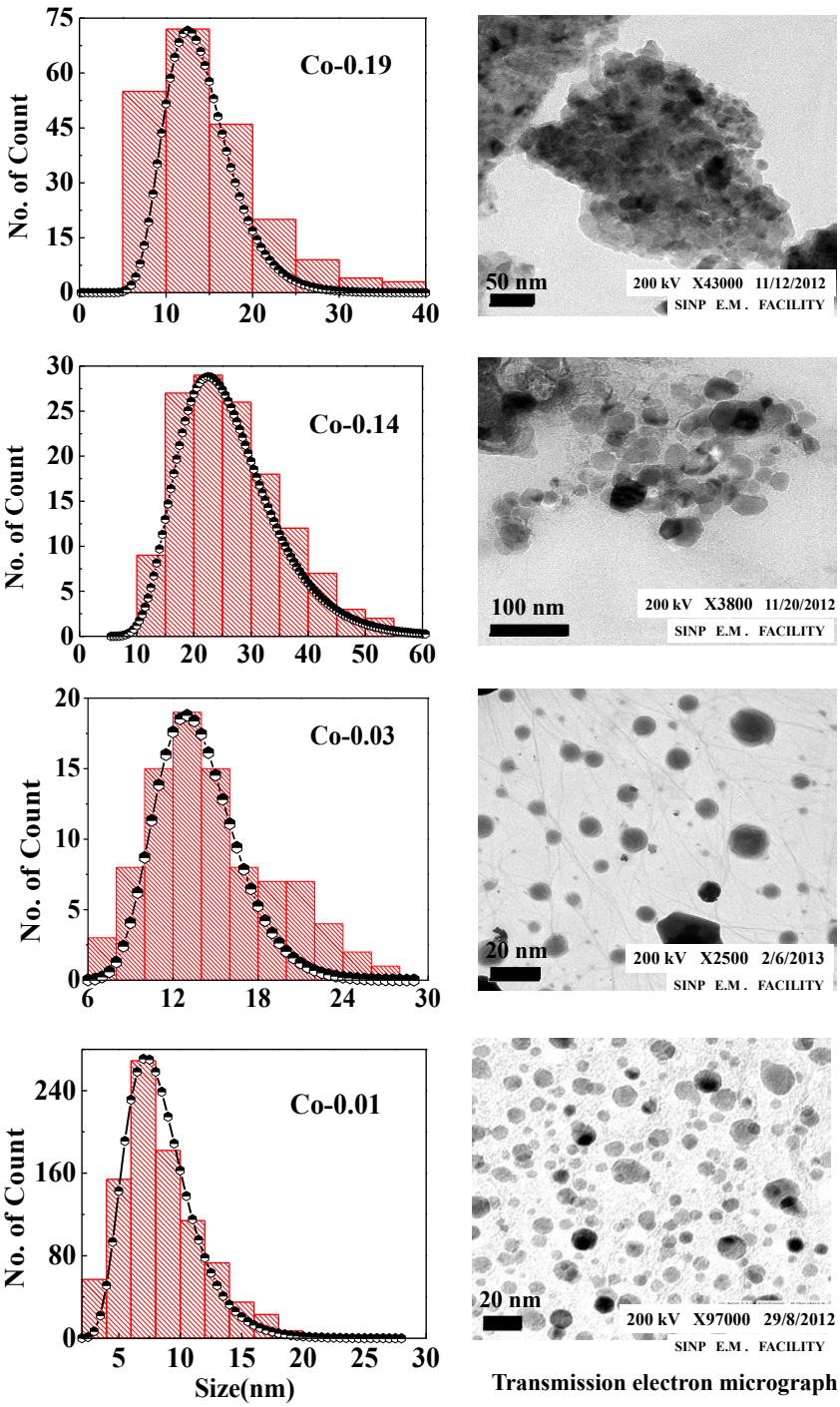

Figure 2.8: Transmission electron micrograph of Co-0.01, Co-0.03, Co-0.15 and Co-0.19 samples.

the following function (Eq. 2.5), as also shown is Fig. 2.8. The average particle size ($< D >$) of first series and second series of the samples from the fitting curves are given in

Table 2.5: The average particle sizes ($< D >$) calculated from transmission electron microscopy (TEM) studies for the samples Co_xCu_{1-x} of the first batch.

Sample Co-x	$< D >$ (from TEM) (nm)
Co-0.01	8
Co-0.03	13
Co-0.05	10
Co-0.08	–
Co-0.10	–
Co-0.15	25
Co-0.21	13.5
Co-0.33	18

Table 2.6: The average particle sizes ($< D >$) calculated from transmission electron microscopy (TEM) studies for the samples Co_xCu_{1-x} of the second batch.

Sample Co-x	$< D >$ (from TEM) (nm)
Co-0.01	9
Co-0.03	13
Co-0.05	10
Co-0.08	14
Co-0.10	18
Co-0.17	–
Co-0.32	15
Co-0.45	12
Co-0.56	–
Co-0.76	16

Table 2.5 and Table 2.6 respectively.

$$f(D) = \frac{1}{\sqrt{2\pi\sigma^2}}\frac{1}{D}\exp(-\frac{\ln\frac{D}{<D>}}{2\sigma^2}) \tag{2.5}$$

Table 2.3 shows that particle sizes obtained from XRD measurements are in general higher than those obtained from TEM studies. In the log-normal particle size distribution, number of particles on the higher side from the position of the peak is greater than that in the lower side. So, XRD reflections may have a higher contribution from larger particles

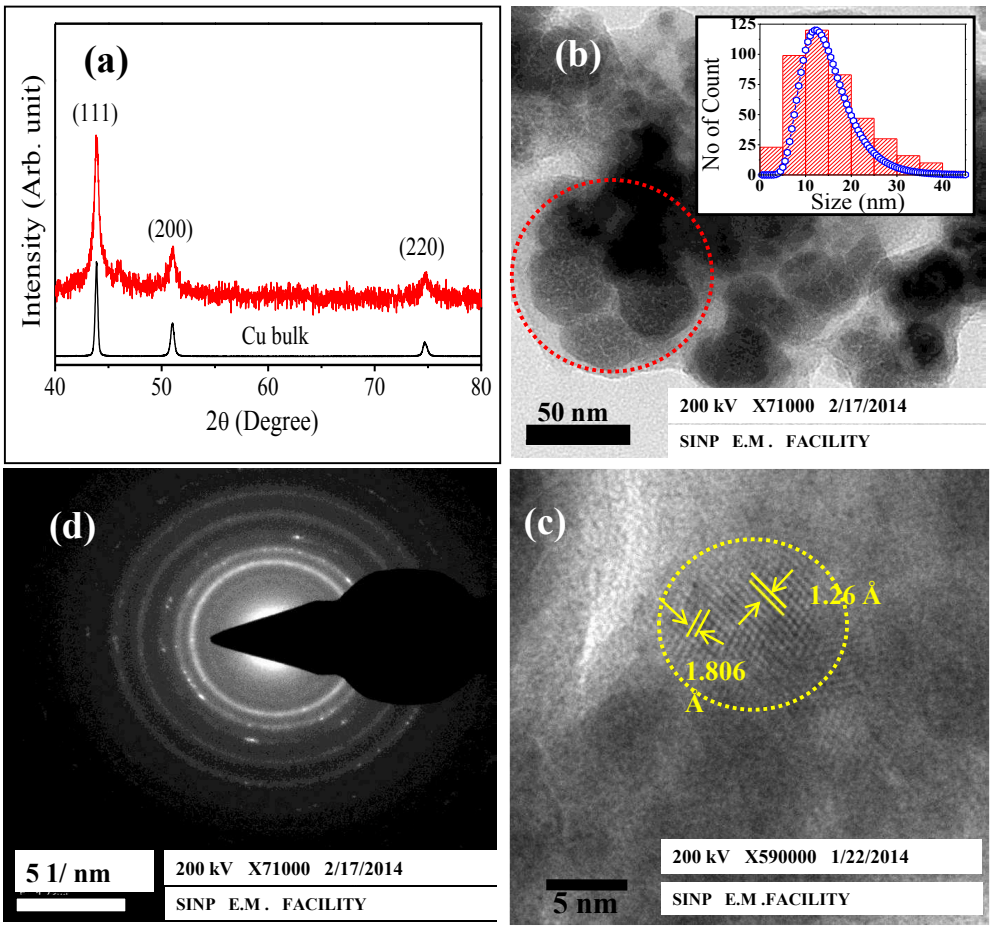

Figure 2.9: For the sample $Co_{0.3}Cu_{0.7}$, (a) room temperature x-ray diffraction (XRD) pattern compared with that of bulk Cu; (b) transmission electron micrograph (TEM), the inset shows particle size distribution; (c) lattice fringes from a region marked by dotted circle in (b); and, (d) selected area diffraction (SAD) pattern.

compared to that from smaller particles. The different distributions in particle sizes probably occurred due to variations in temperature and reaction rate. Since these parameters could not be sufficiently controlled in our experiment, any relation between particle size and composition could not be established. Figure 2.9(b) shows the transmission electron micrograph of the sample $Co_{0.32}Cu_{0.68}$. The high resolution TEM (HRTEM) image of the sample $Co_{0.32}Cu_{0.68}$ (Fig. 2.9(c)) shows lattice fringes signifying crystalline nature of the particles. The lattice spacing measured from HRTEM images are 0.209, 0.181 and 0.126 nm which may be compared with interplaner spacing of copper, *i.e.*, 0.2087, 0.1808 and

0.1278 nm, respectively. The selected area diffraction (SAD) pattern was recorded from a region marked by a circle in Fig. 2.9(b). The pattern shown in Fig. 2.9(d) consisting of concentric rings and distinct spots originating from isolated tiny single crystals of these nanostructures. The measured lattice spacing from SAD pattern further confirms that the alloy is formed in fcc crystalline phase as in copper. Figure 2.9 show the transmission electron micrograph of the second batch samples (a) Co-0.03; (b) Co-0.05; (b) Co-0.56 and Co-0.76. Figure 2.10(d) also show the assembly of nanoparticles in lump and filament like formations.

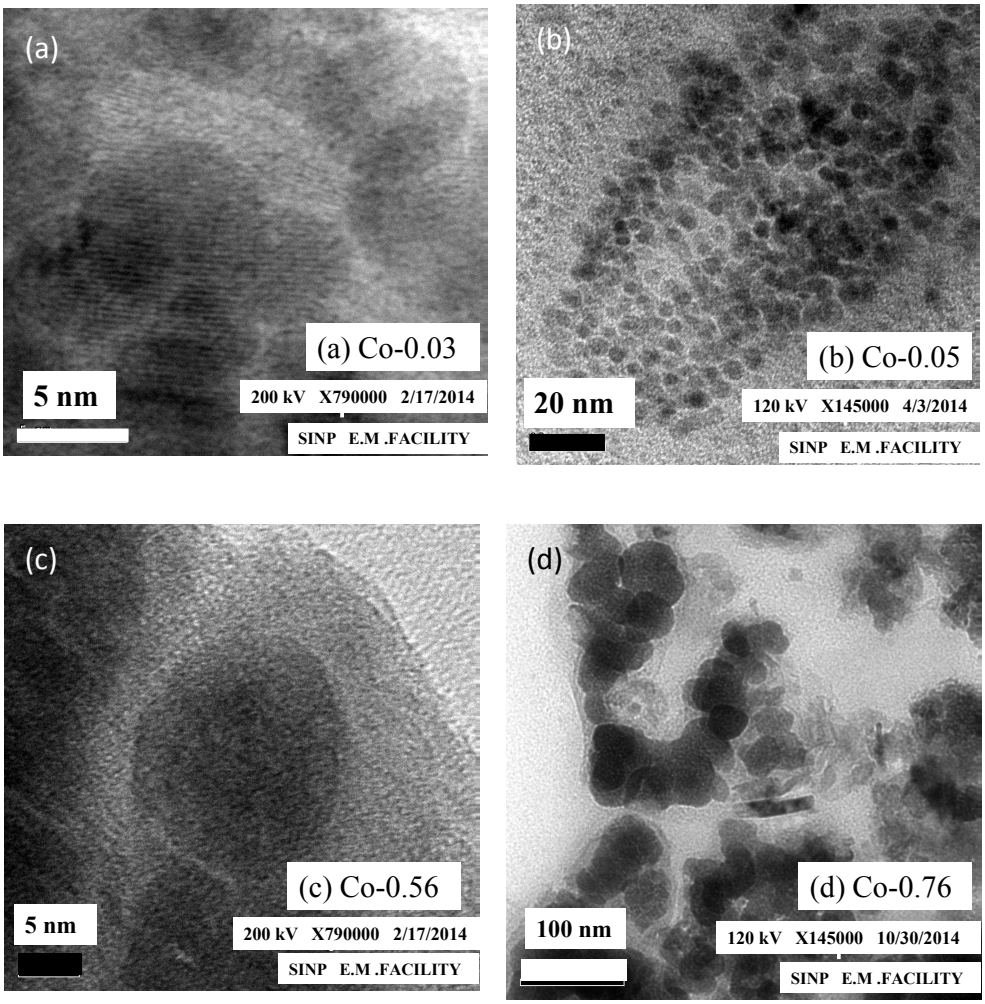

Figure 2.10: TEM picture of the second batch samples (a) Co-0.03; (b) Co-0.05; (c) Co-0.56 and (d) Co-0.76.

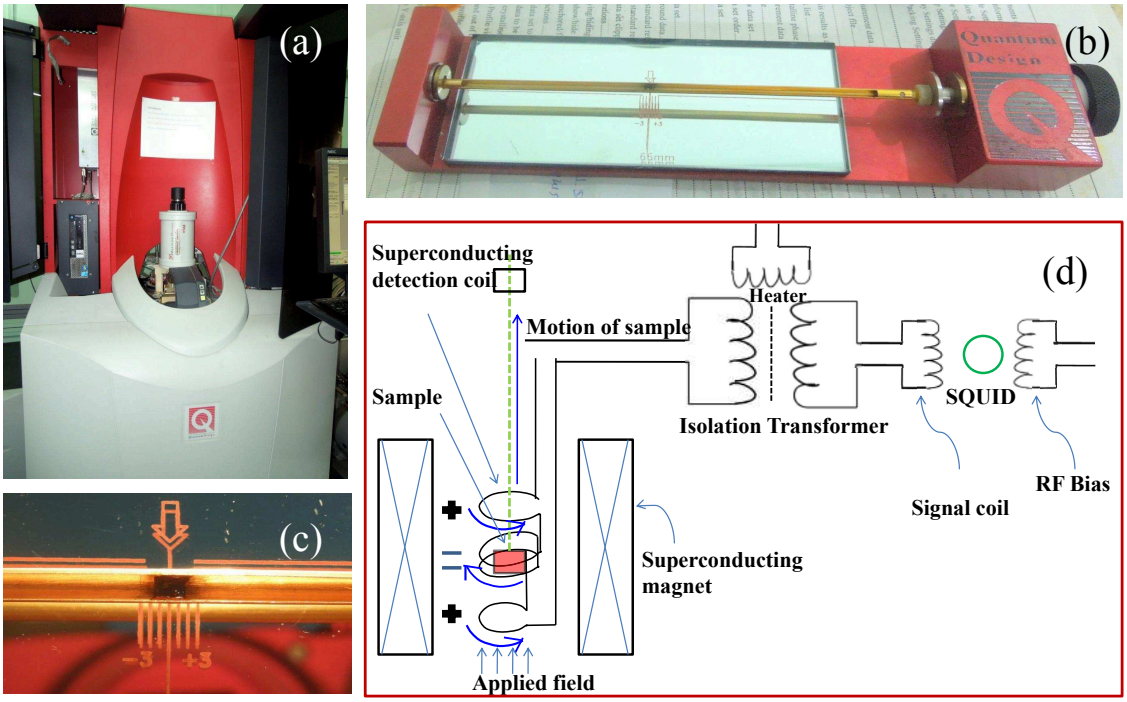

Figure 2.11: *(a) Photo of superconducting quantum interference device (SQUID) magnetometer (Quantum Design), (b) the sample holder of SQUID-VSM mwasurement, (c) sample placed in sample holder, (d) schematic diagram of SQUID-VSM magneometer.=*

2.3 Measurement technique

2.3.1 Magnetization measurements by VSM-SQUID (Quantum Design)

Superconducting Quantum Interference Device (SQUID) is the most sensitive device for measuring extremely small magnetic fields. SQUID magnetometer is used to characterize the magnetic materials with the highest sensitivity over a broad range of temperature. There are several components in a SQUID magnetometer - (1) superconducting magnet; (2) superconducting detection coil; (3) SQUID; (4) the electronic control system. A picture of superconducting quantum interference device vibrating sample magnetometer (SQUID-VSM) of Quantum Design is shown in the Fig 2.10(a). Figure 2.11(b) and (c) show the

sample loaded in the sample holder of SQUID-VSM. A schematic diagram of diagram of SQUID magnetometer is shown in Fig 2.10(d). The superconducting magnet is made by a superconducting solenoid, which is kept at liquid helium temperature. Although a completely closed superconducting loop is used for operating the magnet in "persistent mode", but the loop can electrically be opened by using a switch. A small heater attached with the superconducting solenoid can be treated as a persistent current switch. When the heater is operated, the small portion of the superconduction solenoid, adjacent to the heater, behaves like a normal conductor, so the superconducting loop is electrically opened up. Thus, one can change the current owing through the superconducting solenoid, by connecting a current source with the heater. Superconducting detection coil is nothing but a piece of a superconducting wire which is configured as a second-order gradiometer. This detection coil is subjected in the region of uniform magnetic field, produced by the superconducting magnet and is connected with the SQUID. SQUID is consisting of a superconducting loop which is interrupted by one or more Josephson junction. The basic principle of SQUID is based on two phenomena of superconductivity - (1) the flux quantization and (2) the Josephson effect. In a SQUID magnetometer, the sample is mounted in a clear plastic straw through another straw segment such that the sample must not slip or rattle when the straw is shaken and attached to one end of a sample rod which is inserted into the dewar. The another end is attached to a servo-motor-controlled platform which is used to move the sample through the detection coils which are placed at the center of the magnet. As the sample moves through the coils, the magnetic flux associated with the coils changes. Since the detection coil, the connecting wires and the SQUID input coil form a close superconducting loop, any change of magnetic flux produces a change in the persistent current in the detection circuit. Such a change in persistent current is proportional to the change in magnetic flux. Since the SQUID acts as a highly linear current-to-voltage converter, the variation in the current in the detection coil produce corresponding variation in output voltage of the SQUID, which is proportional to the magnetic moment of the

sample. The output voltage is recorded as a function of the position of the sample within the coil. A linear regression algorithm of the MPMS software fits the measured output data points to the theoretical curve of an ideal dipole and thus extracts the magnetic moment. As the SQUID is highly sensitive device, the sensor itself is shielded properly from the fluctuations of the ambient magnetic field of the laboratory as well as from the magnetic field produced by superconducting magnet.

2.3.2 Transport measurements by physical property measurement system (Quantum Design)

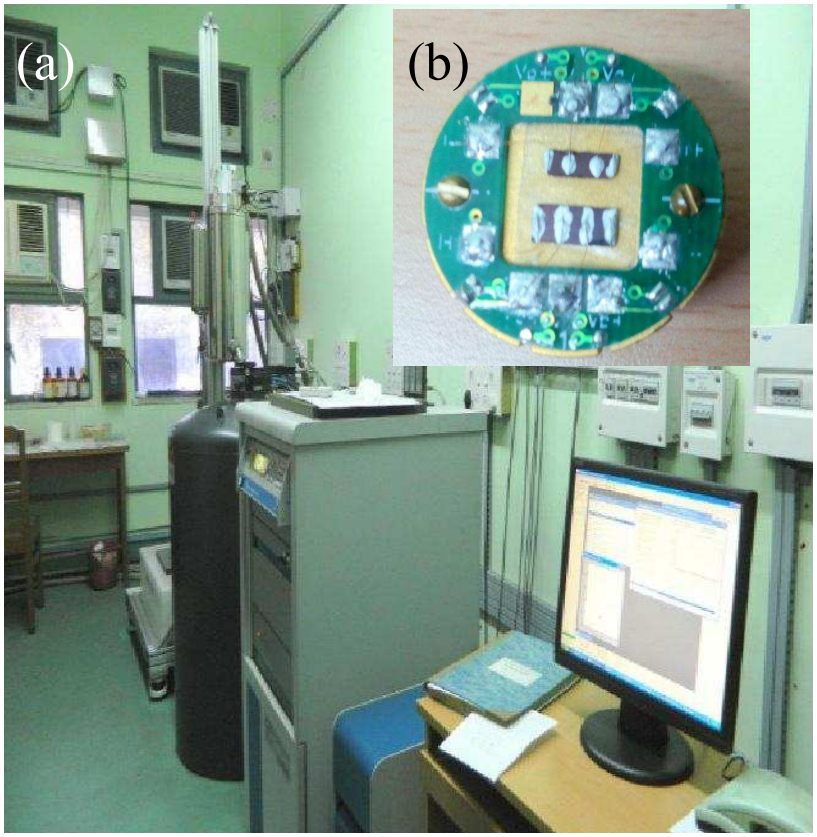

Figure 2.12: *(a) Physical property measurement system (PPMS) (Quntum Design) set up, (b) sample holder for resistivity measurement with sample.*

The electrical resistivity of the samples were measured by using standard four probe technique of physical property measurement system (PPMS). The four probes are four thin copper wires, which were point-connected to the rectangular-shaped sample using conductive silver paint contacts. The current is made to flow between two outer probes and the voltage is measured between two other inner probes. For the temperature variation of the sample, a closed-cycle helium refrigerator was used. Sample temperature was controlled by using temperature controller that monitors the voltage of a calibrated GaAlAs diode. To measure the sample temperature accurately, one end of a chromel-alumel thermocouple was placed very near to the sample. A direct current was sent through the sample from a constant current source and the voltage across the sample was measured by using a nanovoltmeter with current flowing in the forward and reverse directions to eliminate the contribution of thermoelectric effect at the contacts.

The signals from the voltage probes and thermocouple are recorded as resistance (R) and temperature, respectively by the computer via a bus interface. The resistivity (ρ) of the sample can be calculated as,

$$\rho = R\frac{l}{A} \tag{2.6}$$

where A is the cross sectional area and l is the length of the sample, *i.e.*, the distance between two inner probes. It should be mentioned that there is some degree of ambiguity as to the appropriate cross sectional area, as the value will depend on the precise path of the current through the sample. It has been assumed that the current flows uniformly throughout the width of the sample. The resistivity values thus obtained should be treated as an upper bound, as the area the current travels through may be restricted. Figure 2.12(a) shows the picture of PPMS (Quantum Design), and sample holder with samples with four probe arrangement for resistivity measurements is shown in Fig. 2.12(b).

CHAPTER 3

RESULTS AND DISCUSSIONS

3.1 Magnetization of as-prepared samples

3.1.1 ZFC/FC magnetization

First we present the magnetization study of the eight as-prepared Co_xCu_{1-x} samples which are denoted as Co-*x* of the first batch. As some of the samples showed small changes in magnetization with time, the samples were subjected to room temperature annealing for six months following which the final magnetic measurements were performed on them.

Measurements at 4-300 K were carried out using a Quantum Design SQUID-vsm with a maximum applied magnetic field of 7 T. For zero-field cooled and field cooled (ZFC/FC) magnetization measurements, the experimental data were recorded in the temperature range 4-300 K after initially cooling the sample first in zero field and then in presence of 10 mT probing field. The ZFC/FC magnetization curves for as-prepared samples Co-0.01 $\rightarrow$ Co-0.33 are shown in Fig. 3.1.

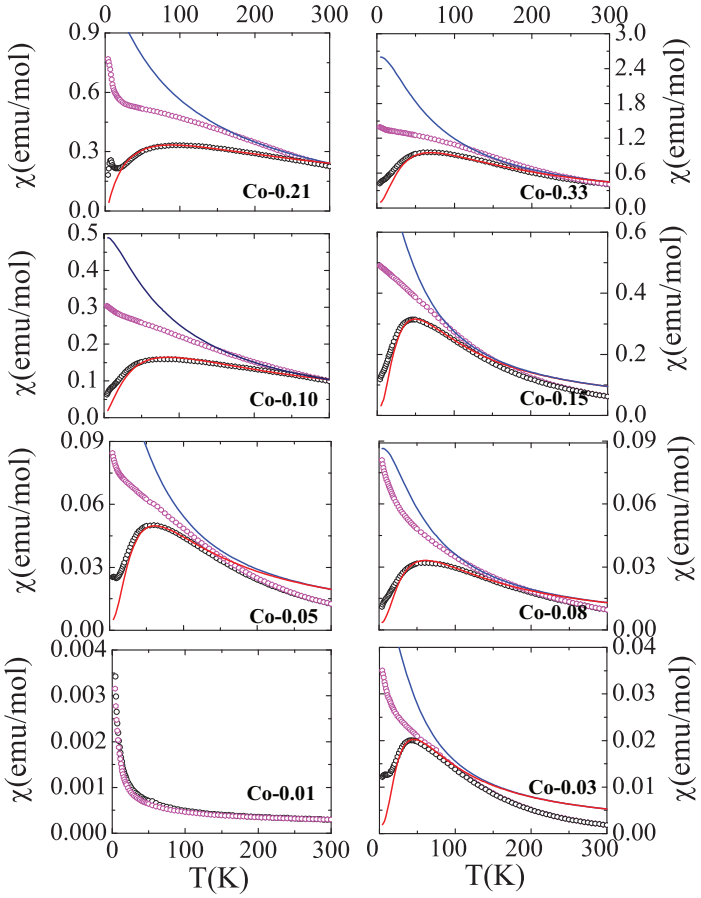

Figure 3.1: Zero-field cooled (ZFC, open symbols) and field-cooled (FC, solid symbols) magnetic susceptibilities of Co-0.01 → Co-0.33, measured with 10 mT probing field. Solid lines are theoretical fit using noninteracting superparamagnetic particles model.

For Co-0.01, ZFC and FC magnetization show identical behavior, both decrease with increase in temperature. At this low Co concentration, the alloy particles are formed in such a way that there is negligible interaction among the localized magnetic moments on Co ions. For other samples Co-0.03 → Co-0.33, the ZFC magnetization shows a broad peak at a temperature T_B^{expt}, the so called blocking temperature, which are centered at 42, 70, 50, 84, 55, 99 and 75 K for Co-0.03, Co-0.05, Co-0.08, Co-0.10, Co-0.15, Co-0.21 and Co-0.33, respectively. ZFC and FC magnetization curves bifurcate at a certain temperature, T_p, higher than T_B^{expt}. For Co-0.03, Co-0.05, Co-0.08 and Co-0.15, the

branching in ZFC/FC behavior occur at 92, 235, 205 and 213 K respectively. These samples are superparamagnetic (SPM) above those bifurcation temperatures. For Co-0.10, Co-0.21 and Co-0.33, the branching occurs near 300 K, and therefore, in these samples superparamagnetic part and blocked part coexist up to room temperature. In case of a nanoparticle system having a size distribution, the temperature T_B^{expt} can be regarded as the highest temperature at which the ZFC and FC magnetization bifurcate corresponding to the larger particles in the system, the ZFC magnetization decreases below this temperature [153, 154].

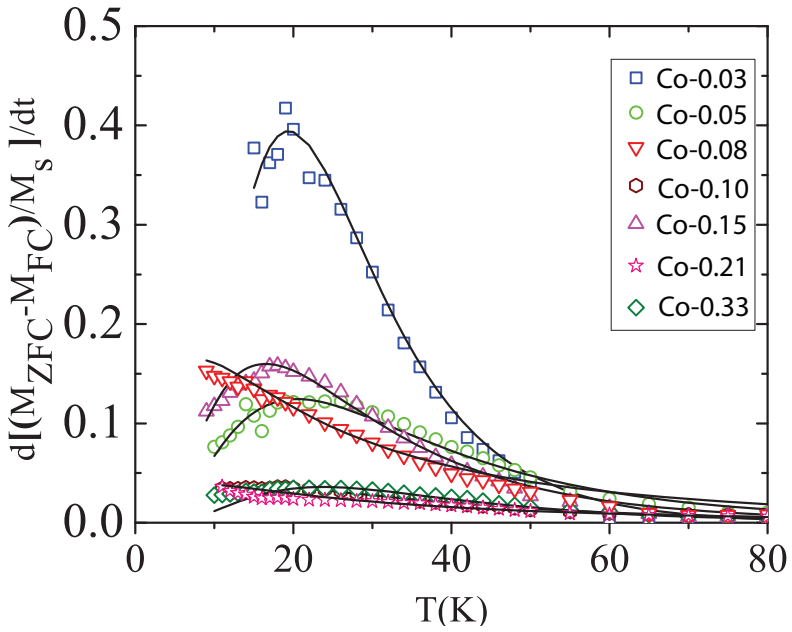

Figure 3.2: Blocking temperature distributions for samples Co-0.01 $\rightarrow$ Co-0.33. Solid lines are fitting with Eq. 3.1.

The ZFC/FC magnetization behavior thus show that the samples from Co-0.03 to Co-0.33 are characterized by blocking temperature distributions [55] which represent variations in particle size and inhomogeneities of their chemical compositions. The derivative of the difference between ZFC magnetization (M_{ZFC}) and FC magnetization (M_{FC}), or, more appropriately, $d[(M_{ZFC} - M_{FC})/M_S]/dT$, where M_S is the saturation magnetization in FC

Table 3.1: The values of blocking temperature (T_B) obtained from blocking temperature distribution, ZFC/FC magnetization and TRM studies, for samples Co-0.03 $\rightarrow$ Co-0.33

Sample	T_B (K) From T_B distribution fitting	T_B (K) From ZFC/FC fitting	T_B (K) From TRM fitting
Co-0.03	24(2)	26(2)	22(2)
Co-0.05	33(2)	44(2)	18(2)
Co-0.08	27(2)	28(2)	20(2)
Co-0.10	32(2)	45(2)	35(2)
Co-0.15	25(2)	33(2)	25(2)
Co-0.21	32(2)	45(2)	28(2)
Co-0.33	33(2)	42(2)	33(2)

condition, represents the number of particles whose blocking temperature falls into the range of the given temperature [155, 156]. The temperature dependence of the above derivative, which is the blocking temperature distribution, can be fitted with a log-normal distribution similar to Eq. 2.5,

$$f(T_B) = \frac{1}{\sqrt{2\pi\sigma^2}}\frac{1}{T_B}\exp(-\frac{\ln^2\frac{T_B}{<T_B>}}{2\sigma^2}) \tag{3.1}$$

Figure 3.2 shows the blocking temperature distributions and their fitting with the above equation for samples Co-0.03 $\rightarrow$ Co-0.33. The values of T_B obtained from above fitting are given in Table 3.1. According to Neel relaxation theory, relaxation time, τ, of a SPM particle at a temperature T is $\tau = \tau_0 exp(E_a/k_BT)$. Here $E_a = K_AV$ is the energy barrier separating the energy minima [52, 135] where K_A is the particle magnetic anisotropy constant, V is the particle volume and $\tau_0(\sim 10^{-9} - 10^{-10}s)$ is a constant. The blocking temperature of a SPM particle is defined as the temperature at which relaxation time τ equals to τ_m, the measurement time. At any given temperature $T < T_B$, the thermal excitations are not sufficient to overcome the anisotropy energy barrier and to rotate the particle magnetization randomly, i.e., the magnetic moments are fixed in a direction during a single measurement. The particle is then called blocked, and its susceptibility can be written as, $\chi_{BL} = M_S^2/3K_A$, where, M_S is the saturation magnetization. When $T > T_B$,

the thermal energy is large so that the magnetic moments overcome the anisotropy energy barrier to align with the magnetic field, and the particle behaves as superparamagnetic. The susceptibility in such condition is given as, $\chi_{SPM} = M_S^2 V/3k_BT$. The total susceptibility in case of ZFC magnetization of a system of non-interacting SPM particles with distributions in both particle volume and blocking temperature can be written as [135],

$$\begin{aligned}\chi_{ZFC} = &\frac{M_S^2 V}{3k_BT}\int_0^T \frac{T_B}{<T>} f(T_B)dT_B \\ &+\frac{M_S^2 V}{3K_A}\int_0^T \frac{T_B}{<T>} f(T_B)dT_B\end{aligned} \tag{3.2}$$

Here, $f(T_B)$ is the distribution function of blocking temperature, $<V>$ is an average volume and $<T_B>$ an average blocking temperature. Using the relationship between $<V>$ and $<T_B>$, the above equation can be written as,

$$\begin{aligned}\chi_{ZFC} = \frac{M_S^2}{3K_A}[(\ln\frac{\tau_m}{\tau_0})&\int_0^T \frac{T_B}{<T>} f(T_B)dT_B \\ &+\int_T^\infty \frac{T_B}{<T>} f(T_B)dT_B]\end{aligned} \tag{3.3}$$

In this equation first term comes from SPM part and the second term from blocked part. For susceptibility of FC part, the SPM part remains the same but the blocked part becomes different. Thus the susceptibility in case of FC magnetization,

$$\begin{aligned}\chi_{FC} = \frac{M_S^2}{3K_A}(\ln\frac{\tau_m}{\tau_0})[&\int_0^T \frac{T_B}{<T>} f(T_B)dT_B \\ &+\int_T^\infty \frac{T_B}{<T>} f(T_B)dT_B]\end{aligned} \tag{3.4}$$

Here also the first term comes from the SPM part and the second term from blocked part. Using K_A value of 3.5×10^8 erg/cm^3 (Sec. 3.1.3), experimental ZFC/FC magnetization data were fitted using the above non-interacting model for samples Co-0.03 $\rightarrow$ Co-0.33, as shown in Fig. 3.1 and $<T_B>$ values obtained thus are given in Table 3.1. These values are

not much different from $< T_B >$ obtained by fitting the blocking temperature distribution.

In some of the samples, *e.g.*, in Co-0.03, Co-0.05 and Co-0.21, ZFC/FC magnetization show some additional features below $\sim$ 15 K. We believe this is due to the presence of nanoparticles of antiferromagnetic cobalt oxide, formed when inert atmosphere conditions was not properly maintained during sample preparation [157]. Such features disappeared when the same samples were annealed in a reducing atmosphere. The effect of annealing on the magnetic properties of these samples will be studied later.

3.1.2 Thermoremanence magnetization

To obtain thermo-remanent magnetization (TRM), the sample was cooled down to 4 K in presence of 5 T magnetic field, followed by magnetization measurements at increasing temperatures. At each temperature, the sample was subjected to the same magnetic field for 60 s; the field was then switched off and after a waiting time of $t_W \sim 100$ s, the remanent magnetization which is the sum total of the magnetic moments that are still blocked at that temperature, was measured. TRM is expressed as M_{TRM}/M_S, normalized by the value of magnetization at 4 K. It reflects the probability of finding a SPM cluster with a blocking temperature (T_B) higher than the measurement temperature. Figure 3.3 Shows the results of TRM studies on different samples Co-0.03 $\rightarrow$ Co-0.33.

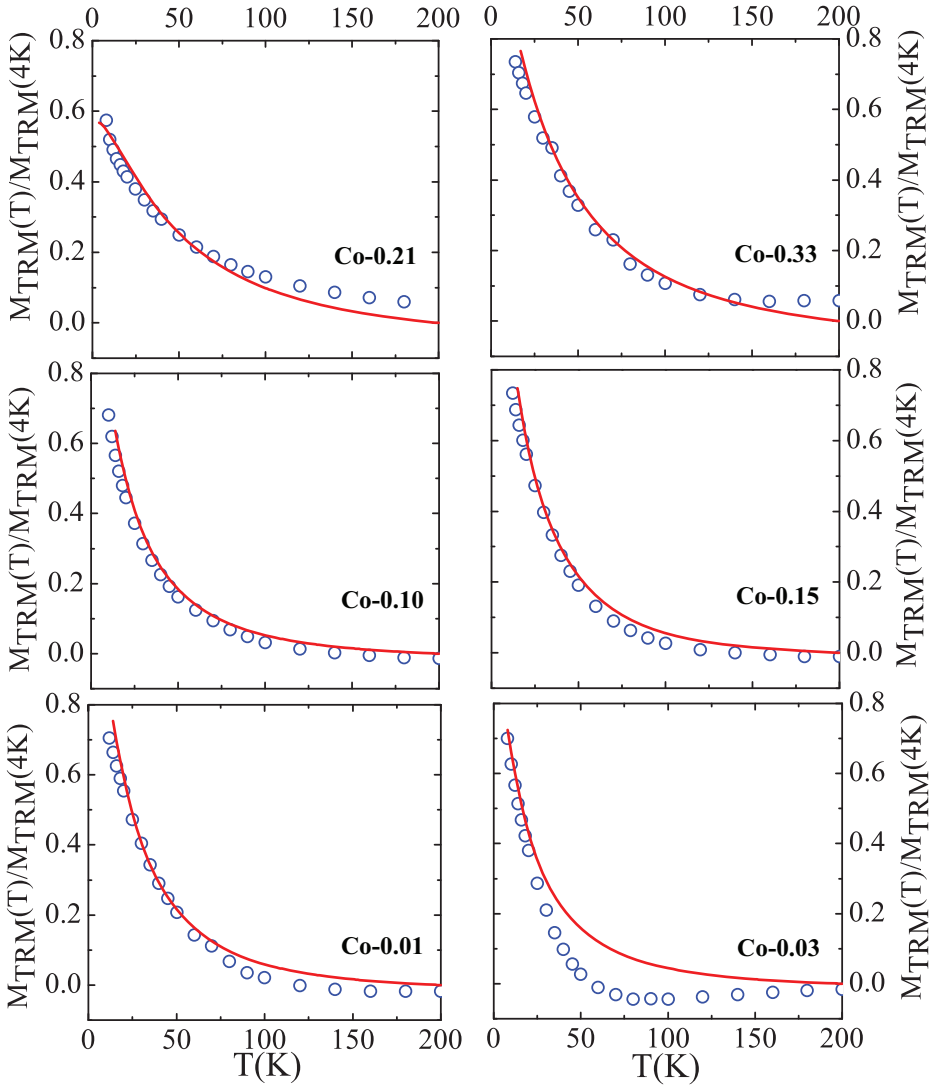

Figure 3.3: Thermoremanent magnetization (TRM) of samples Co-0.03 → Co-0.33 (Co-0.10 is not shown). Solid lines are theoretical fit as in text.

The TRM in independent particles model can be expressed as,

$$\frac{M_{TRM}}{M_S} = 0 + \int_T^{\infty} \gamma f(T_B) dT_B, \tag{3.5}$$

where the factor γ is a constant and equal to 0.5 in the case of uniaxial anisotropy [52, 135]. As the applied field is zero when the measurement is made there is no contribution from the unblocked particles. The zero term in right hand side of the equation represents unblocked

part.

Blocking temperatures from fitting the experimental TRM data with Eq. 3.5 are given in the Table 3.1. The blocking temperature obtained from TRM have nearly the same values with blocking temperatures from ZFC/FC magnetization measurements. In their study on $CoSiO_2$ granular films, Denardin *et al.* [135]. obtained a smaller blocking temperature from TRM than from ZFC/FC magnetization measurements. In their system, the SPM clusters in a silicate matrix were coupled with each other through dipolar interaction, and the magnetic relaxation process during TRM measurement, which started from a magnetized state, mixed both collective (between clusters) and individual (within a cluster) demagnetizing processes, involving energy barriers smaller than that for the magnetization reversal of an isolated cluster. In other words, for TRM the decay from a magnetically ordered state is mainly governed by the anisotropy of the individual particles and their coupling. In the present case, the surfactant coated particles are isolated and there is negligible interaction between the particle moments. It is assumed that the relaxation process during TRM is governed only by the intra-particle demagnetizing process which is nearly the same as the magnetization reversal in ZFC experiment. As a result, T_B from TRM and ZFC/FC magnetization measurements are not much different from each other. These results therefore satisfy the independent particle model.

3.1.3 Hysteresis loops

The magnetic field (H) dependence of magnetization (M) were studied for all samples at different temperatures 4-300 K, in ZFC condition in between -7 T $\leq H \leq$ 7 T. At 4 K, Co-0.01 shows no coercivity and exhibits SPM magnetization behavior identical in ascending and descending fields. All other samples exhibit prominent hysteresis loops yielding coercive fields (H_C) of $\sim$ 400 Oe. Existence of different ferromagnetic components

in a non-homogeneous magnetic material can be ascertained from $d(\Delta M)/dH$ versus H plots [158], where ΔM is the difference between the ascending and descending parts of the hysteresis loops for $H > 0$. In such plots, the number of maxima corresponds to the number of coercivity components. At 10 K, such plots (Fig. 3.4) for Co-0.03 $\rightarrow$ Co-0.33 yield only one maximum which shows that though the samples have wide distribution in their particle sizes, there is one dominant coercivity component.

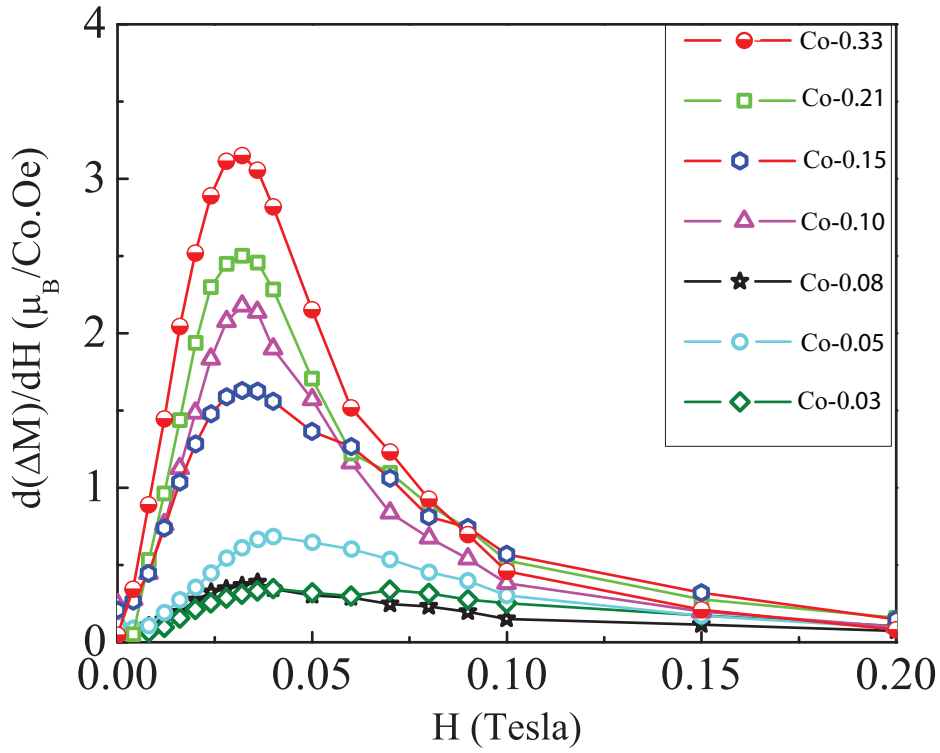

Figure 3.4: $d(\Delta M)/dH$ versus H plots for Co-0.03 $\rightarrow$ Co-0.33 at 10 K.

Figures 3.5 and 3.6 show M*vs*.H for all samples at 4 K. For clarity, only the part of hysteresis loops at descending magnetic field have been shown here. The same figures also show the theoretical fit of the data using a combination of superparamagnetic (SPM) and

ferromagnetic (FM) contributions, using the following equation [159],

$$M(H) = \frac{2M_S^{FM}}{\pi}\left[tan^{-1}\left(\frac{H \pm H_C}{H_C}\right) tan\left(\frac{\pi M_R}{2M_S^{FM}}\right)\right] + M_S^{SPM}\left[coth\left(\frac{\mu H}{k_B T}\right) - \left(\frac{\mu H}{k_B T}\right)^{-1}\right] + \chi^{PM} H \tag{3.6}$$

The first and second terms on the right hand side of the equation represent the FM and SPM contributions, respectively. The fitting parameters are M_S^{FM} and M_S^{SPM}, the saturation magnetization for FM and SPM parts, respectively, in terms of magnetic moment per Co atom, and μ, the average magnetic moment of SPM particles or clusters. The values of remanence, M_R, and, coercivity, H_C are obtained from experimental data. The third term in the equation represents a paramagnetic (PM) contribution, nearly uniform in all samples, with $\chi^{PM} \sim 10^{-6}\mu_B$/Oe. For a more accurate representation of the SPM part, we used a weighted sum of Langevin function [160],

$$M = \int_0^\infty L(x) M_S dx, x = \frac{\mu H}{k_B T} \tag{3.7}$$

where M_S is the saturation magnetization of N particles with magnetic moment μ and $L(x)$ is the Langevin function. Taking the saturation magnetization as an exponential distribution, the above equation is written as,

$$M_S = \int_0^\infty \frac{1}{\sqrt{2\pi}} \frac{1}{\mu\sigma} \exp(-\frac{\ln^2 \frac{\mu}{<\mu_0>}}{2\sigma^2}) d\mu \tag{3.8}$$

Here σ is the log-normal distribution width and μ_0 is the median of the distribution related to the average magnetic moment μ_m by the following equation,

$$\mu_m = \mu_0 exp(\frac{\sigma}{2}) \tag{3.9}$$

Table 3.2: Ferromagnetic and superparamagnetic saturation magnetization, M_S^{FM} and M_S^{SPM}, respectively, remanence (M_R), coercivity (H_C), and the average magnetic moment (μ) for the CoCu nanostructured alloys, obtained from the analysis of magnetization data at 4 K. Magnetic anisotropy constant (K_A) at 300 K are also given.

Sample	M_S^{FM} (μ_B/Co)	M_R (μ_B/Co)	H_C (Oe)	M_S^{SPM} (μ_B/Co)	μ (μ_B)	K_A(at 300 K) (erg/cm^3)
Co-0.01	–	–	–	1.310(5)	4.5(1)	$--$
Co-0.03	0.07(1)	0.030(1)	390(10)	0.48(1)	7.0(1)	4.2×10^8
Co-0.05	0.08(1)	0.038(1)	420(20)	0.45(1)	7.3(1)	4.7×10^8
Co-0.08	0.08(1)	0.023(1)	330(10)	0.38(1)	7.5(1)	2.4×10^8
Co-0.10	0.13(1)	0.076(1)	410(20)	0.225(5)	10.0(1)	3.4×10^8
Co-0.15	0.12(1)	0.078(1)	420(20)	0.225(5)	10.8(1)	2.7×10^8
Co-0.21	0.20(1)	0.102(1)	340(10)	0.360(5)	11.5(1)	3.2×10^8
Co-0.33	0.18(1)	0.099(3)	320(10)	0.200(5)	13.0(1)	3.1×10^8

The various parameters in Eq. 3.6 obtained from fitting are given in Table 3.2. Sample Co-0.01 does not have coercivity or remanence even at 4 K. According to the above analysis, sample Co-0.01 is superparamagnetic, as seen in Sec. 3.1.1, with Co atom magnetic moment tending towards a value of 1.3 μ_B at saturation. But Co-0.03 $\rightarrow$ Co-0.33 have both superparamagnetic and ferromagnetic contributions in the magnetization. In these samples, the saturation moments of Co vary in the range 0.35-0.55 μ_B. The variations of saturation magnetization show that with increasing Co concentration, a larger fraction of Co magnetic moments contribute towards ferromagnetism and less towards superparamagnetism of the particles. Total magnetic moment for SPM cluster μ increase with increasing Co concentration from 4.5 μ_B to 13 μ_B for Co-0.01 $\rightarrow$ Co-0.33 samples. Coercive fields at 4 K for all the samples are in the range 320-420 Oe, however, the variation in its values are independent of Co concentration. At 300 K, the samples Co-0.03 $\rightarrow$ Co-0.33 exhibit small hysteresis loops and the coercive fields vary in the range 5-30 Oe.

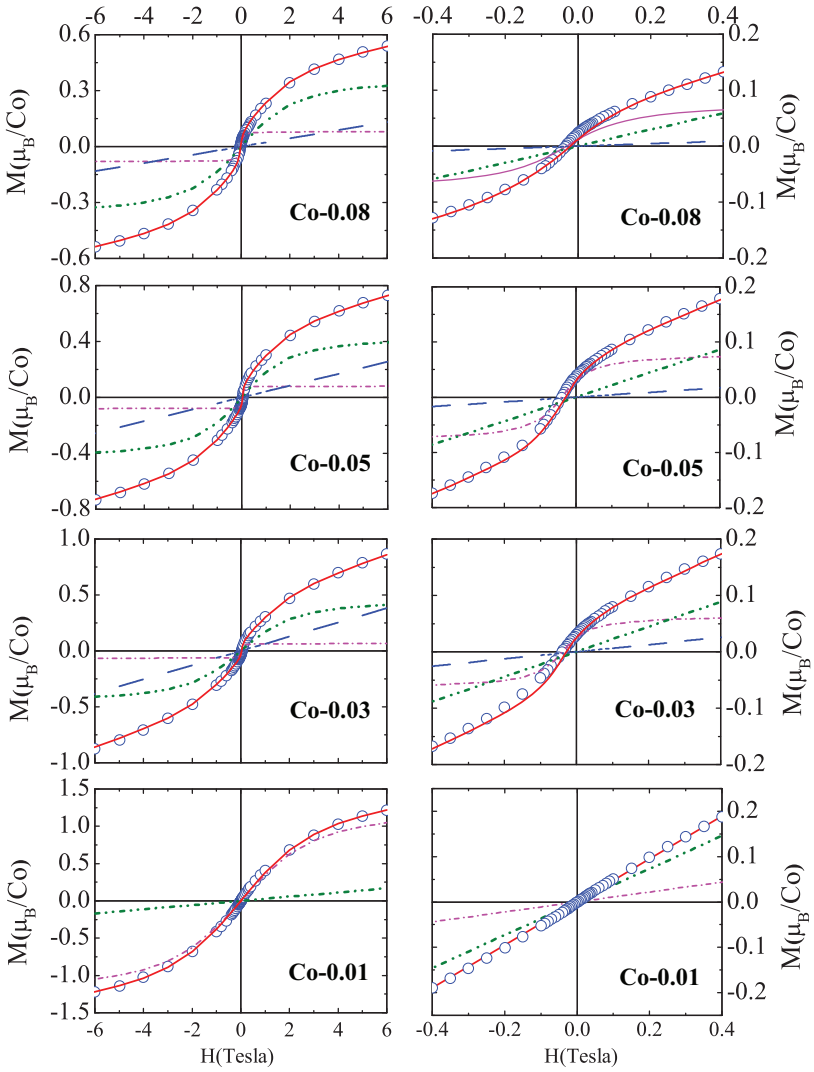

Figure 3.5: Data for descending magnetic fields of hysteresis loops obtained at 4 K for samples Co-0.01 → Co-0.08. The experimental data are shown by open circles. The left panels show data in fields -6.0 to 6.0 T for for Co-0.03 → Co-0.08; and the right panels show data in the expanded low field region -0.4 to 0.4 T for the corresponding samples. The simulations as mentioned in the text are shown as the FM (dash and dot), the SPM (dash, dot and dot), the PM (dash) components and their sum (continuous line).

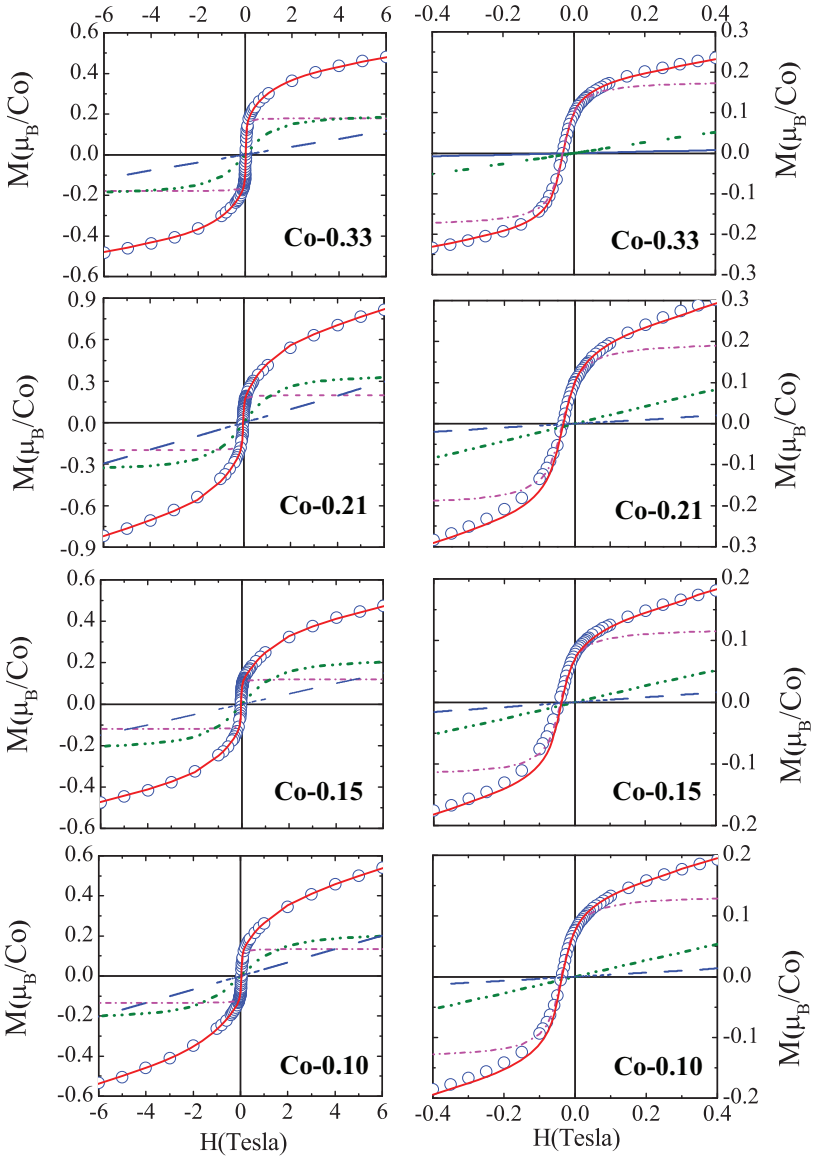

Figure 3.6: Similar to Fig. 3.5, for the samples Co-0.10 → Co-0.33.

The magnetic anisotropy constant, K_A, of a SPM particle of volume V is given by the Neel-Arrhenius relation, $K_AV = 25k_BT_B$. However, in the present case, there is a rather large distribution in the particle size and also at any temperature, there are both SPM and FM parts in magnetization. In order to obtain K_A, we have estimated V from above-mentioned analysis of hysteresis loops at 300 K. At this temperature, the magnetization has a dominant SPM contribution, and the FM contribution which gets saturated at ∼1 T is negligible.

The cluster moment μ is obtained from fitting, and knowing [161, 162, 163] that for SPM particles the moment is 2.2 μ_B per Co atom, we get the number of Co atoms in a particle or cluster. Assuming Co in fcc lattice have the same volume as copper, *i.e.*, $11.76 \times 10^{-24} cm^3$, we get V, and hence, K_A. The values so obtained are also given in Table 3.2.

Anisotropy constant is much larger for SPM particles than for bulk metal [164, 165, 166]. It is known that K_A for bulk cobalt is $7 \times 10^6 erg/cm^3$, and for SPM particle it is $3 \times 10^8 erg/cm^3$, which is comparable to the average of K_A values in Table 3.2. For bulk samples, K_A depends on magneto-crystalline anisotropy. For nearly spherical SPM particles, the dominant contributions to magnetic anisotropy come from surface effects and stress. Here, Co atoms have assumed Cu lattice and this may have further increased the stress [152].

An estimate of SPM particle size can also be obtained from above analysis of magnetization data. The sizes are in the range 7.3 to 9.4 nm, increasing with Co content. These values are much smaller than the particle size obtained from TEM studies, and possibly indicate that in a particle the magnetically active region is much smaller than its total volume, and therefore the particles are magnetically isolated from each other. On the other hand, it has been noted, as shown in Fig. 3.7, that the room temperature magnetization data can be simulated with the Langevin function, without considering inter-particle magnetic interactions, with an equation of the type,

$$M(H)_{300K} = M_S \int_0^\infty f(D) L(H,D) dD, \tag{3.10}$$

where, $f(D)$, the size distribution functions, are the same as those obtained in TEM analysis of the corresponding samples.

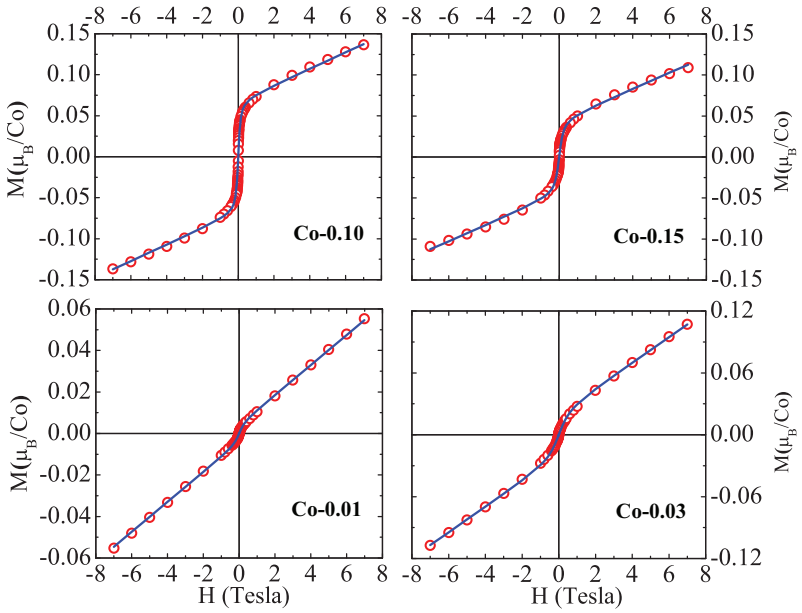

Figure 3.7: Experimetal data (circles) for descending magnetic field parts of hysteresis loops obtained at 300 K for samples Co-0.01, Co-0.03, Co-0.10 and Co-0.15. The theoretical fit (solid line) using Eq. 3.10 are also shown.

3.2 Magnetization of annealed samples

Now we discuss the magnetization, memory effect and transport studies of the eleven annealed Co_xCu_{1-x} samples which are denoted as Co-x of the second batch. The magnetic measurements were performed with a superconducting quantum interference device vibrating sample magnetometer, SQUID-vsm, of Quantum Design.

3.2.1 ZFC/FC Magnetization and determination of blocking temperature

The magnetizations of Co_xCu_{1-x} in standard zero-field cooled (ZFC) and field cooled (FC) conditions using different magnetic fields, shown in Fig. 3.8 for Co-0.32, are characteristic of superparamagnetic particles. The magnetization of such a particle can

be reversed by thermal activation over an energy barrier with a characteristic time that is temperature dependent. The blocking temperature T_B is defined as the temperature at which the characteristic time is ~ 100 s. In presence of a magnetic field, the energy barrier and therefore the blocking temperature, both are reduced.

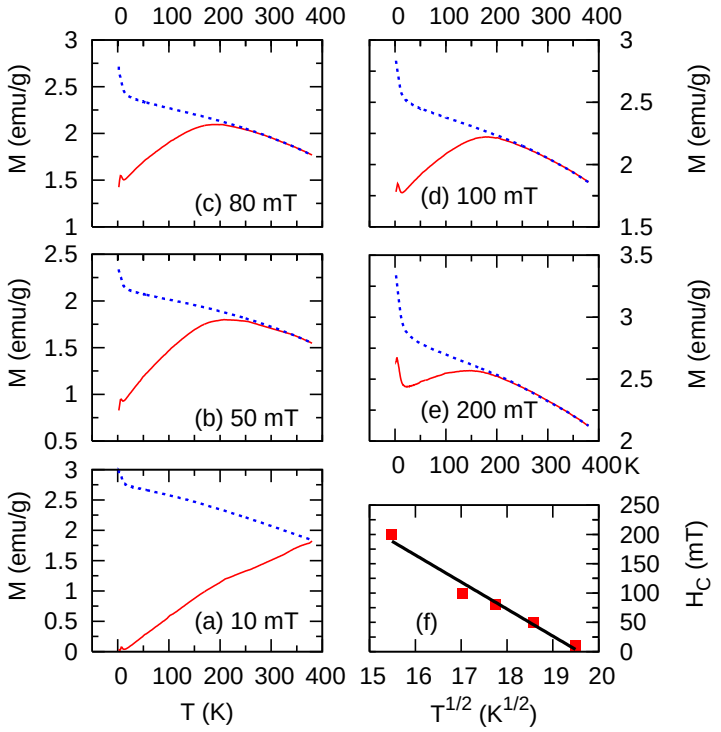

Figure 3.8: The curves of zero-field cooled (ZFC, solid line) and field cooled (FC, broken line) magnetization for Co-0.32 sample at magnetic fields of (a) 10 mT; (b) 50 mT; (c) 80 mT; (d) 100 mT; and (e) 200 mT. The plot of magnetic field *vs.* $T^{1/2}$, where, T is the temperature of bifurcation of ZFC and FC curves is shown in (f) with the linear fit using Eq. 3.11.

A system of magnetic nanoparticles with a finite size distribution has a blocking temperature distribution. In Fig. 3.8, the temperature at which ZFC and FC curves bifurcate corresponds to the blocking temperature of the particle with the largest volume for which the coercive field (H_C) is the same as the applied magnetic field. H_C and T_B are related as

[167],

$$H_C = \frac{2K_AV}{\mu}\left[1-\left(\frac{T}{T_B}\right)^{1/2}\right] \tag{3.11}$$

where, μ is the magnetic moment of the particle and K_AV, the energy barrier is the product of magnetic anisotropy, K_A, and particle volume, V. The largest significant blocking temperature in the distribution can be obtained from ZFC-FC magnetization using different magnetic fields as shown in Figs. 3.8(a) to (e) and then plotting H versus $T^{1/2}$ as shown in Fig. 3.8(f). The blocking temperature thus estimated for Co-0.32 sample was 376 K. The as-prepared samples of similar composition had blocking temperatures only of $\sim$ 40 K (presented in Sec. 3.1.1),

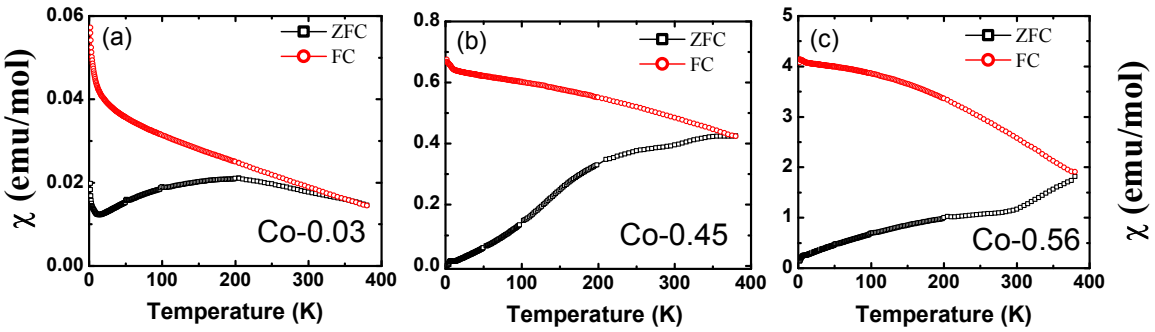

Figure 3.9: The curves of zero-field cooled (ZFC, solid line) and field cooled (FC, broken line) magnetic susceptability at 10 mT magnetic fields of samples (a) Co-0.03; (b) Co-0.45; (c) Co-0.56.

The low cobalt containing samples, Co-0.01 $\rightarrow$ 0.05, ZFC and FC curves bifurcate at temperatures in between 200-300 K. For other samples, Co-0.07 $\rightarrow$ Co-0.76, ZFC is still increasing up to 380 K. For all these samples we have estimated the blocking temperature using the method discussed above. At initial temperatures $\sim 2-8$ K, the ZFC curves at low fields $\leq$ 80 mT show a sharp small peak followed by a minimum. At around same temperature, there is a rapid decrease in FC magnetization at all fields. These features are prominently visible in samples Co-0.01 $\rightarrow$ Co-0.32, but rather suppressed in other samples.

Table 3.3: The values of blocking temperature (T_B) obtained from Eq. 3.11, glassy temperature obtained from experimental ZFC curves for all samples Co_xCu_{1-x}. The relaxation time τ_2 from Eq. 3.12, and the values of n from Eq. 3.13 are obtained at 4 K.

Sample	T_B (K)	T_G (K)	τ_2 (Sec)	n –
Co-0.01	210	5.6	4×10^5	0.79
Co-0.03	194	5.6	5.3×10^5	0.77
Co-0.05	255	6.6	5.2×10^5	0.80
Co-0.08	248	5.2	6.8×10^5	0.75
Co-0.10	235	8.0	7.6×10^5	0.71
Co-0.17	278	6.0	11×10^5	0.56
Co-0.32	376	7.0	13×10^5	0.52
Co-0.45	391	8.6	26×10^5	0.42
Co-0.56	383	7.4	46×10^5	0.25
Co-0.76	323	6.6	–	–

Such a behavior in magnetization could originate from the antiferromagnetism of surface oxide. However, at higher magnetic fields ≥ 0.2 T the peak at low temperature is no more obtained. This behavior may suggests the occurrence of spin-glass like ordering [55, 157, 168, 169, 170] which will be further investigated. Figure 3.9(a), (b) and (c) represent the ZFC/FC magnetization in the presence of 10 mT magnetic field for samples Co-0.03, Co-0.45 and Co-0.56, respectively. Table 3.3 shows the blocking temperature (T_B) and glassy temperature (T_g), the latter being the position of low temperature (below 10 K) peak in ZFC curve, for all samples Co-0.01 $\rightarrow$ Co-0.76.

3.2.2 Exchange bias and field dependence of magnetization

The hysteresis loops at various temperatures 2-300 K were obtained in both ZFC and FC conditions. In the latter case, when the sample was cooled down from 380 K in presence of 7 T magnetic field, the *Mvs.H* loops were asymmetric and shifted along the negative H-axis. If H_{C1} and H_{C2} are the shifts on positive and negative segments of H-axis, then the magnitude of the exchange bias field, is defined as H_{EB} equals to $(H_{C1}+H_{C2})/2$. Figure

3.10 shows the expanded central region of one such hysteresis loop at 4 K for Co-0.32 sample.

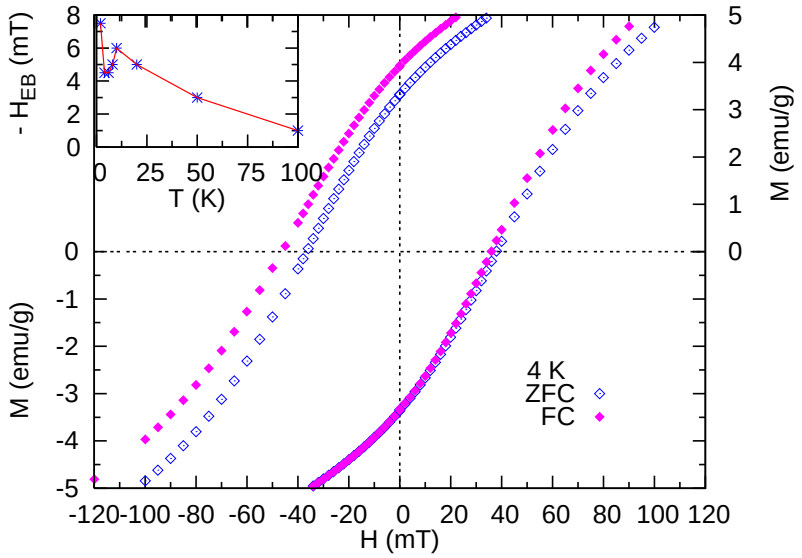

Figure 3.10: In Co-0.32, expanded central portion of hysteresis loops (magnetization (M) *vs*. magnetic field (H)) at 4 K and $-7 \leq H \leq 7T$ under conditions of ZFC (open symbols) and FC (filled symbols). Inset shows temperature dependence of exchange bias field (H_{EB}). The line joining the data points is a guide to the eye.

In general, exchange bias appears when ferromagnetism (FM) co-exists with any other magnetic interactions, *e.g.*, antiferromagnetism (AFM), spin-glass etc. As observed earlier, these particles are formed in a core-shell type structure in which the blocked moments in Co rich core become ferromagnetic. Inset of Fig. 3.10 shows that H_{EB} develops well above 100 K and increases with decrease in temperature to attain a value of ~ 7.5 mT at 2 K. This result is consistent with particles having a FM core co-existing with AFM

interaction involving uncompensated surface spins [171, 172]. However, the formation of antiferromagnetic cobalt oxide is ruled out because its signature could not be obtained from XRD, magnetization or resistivity studies in sample annealed in hydrogen atmosphere. However, the signature of spin-glass phase is obtained also in ZFC memory effect below $\sim$ 10 K, *i.e.*, the same temperature as in ZFC-FC magnetization and described in Sec. 3.2.4. The anomalous behavior of H_{EB} around 10 K is due to the spin-glass ordering which possibly occurs in Cu-rich regions but not identified definitely.

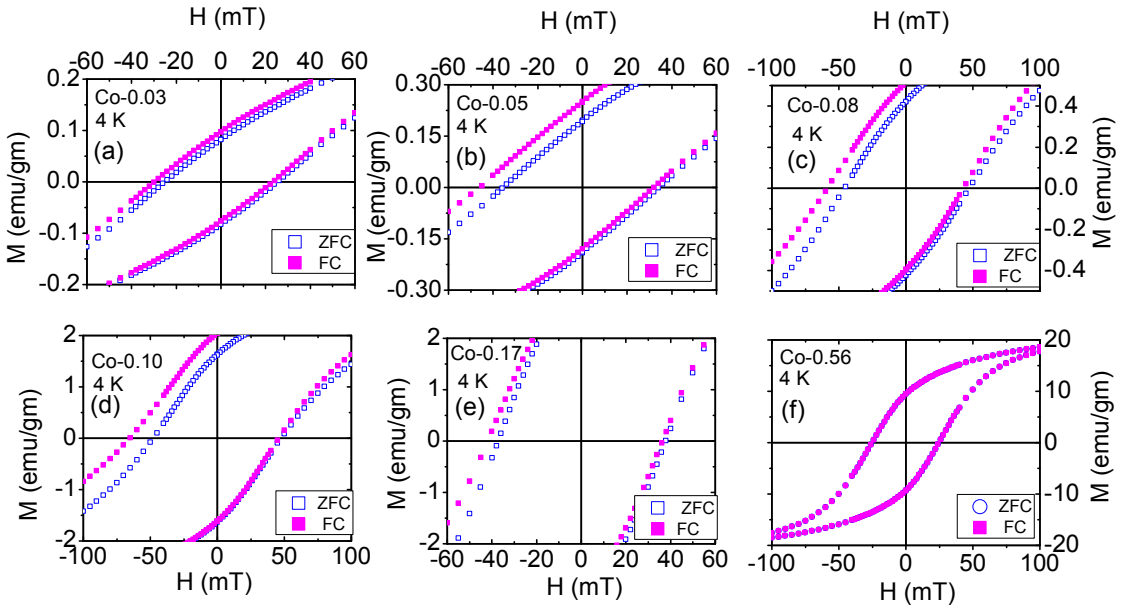

Figure 3.11: Expanded central portion of hysteresis loops (magnetization (M) *vs*. magnetic field (H)) at 4 K under conditions of ZFC (open symbols) and FC (filled symbols) in samples (a) Co-0.03, (b) Co-0.05, (c) Co-0.08, (d) Co-0.10, (e) Co-0.17; and (f) Co-0.56.

The annealed samples Co-0.01 to Co-0.33 yielded exchange bias ranging in between 20-150 Oe at 4 K. It has been argued that H_{EB} originates at the interface of Co-rich core and Cu-rich shell of the core-shell type structure. Figure 3.11 shows hysteresis loops at 4 K under conditions of ZFC (open symbols) and FC (filled symbols) in samples (a) Co-0.03, (b) Co-0.05, (c) Co-0.08, (d) Co-0.10, (e) Co-0.17; and (f) Co-0.56. In the figure we see

that exchange bias first increases from the sample Co-0.03 to Co-0.10 with increasing Co content. But it starts to decrease from the sample Co-0.15 and in high Co samples, Co-0.56 and beyond, the exchange bias disappears.

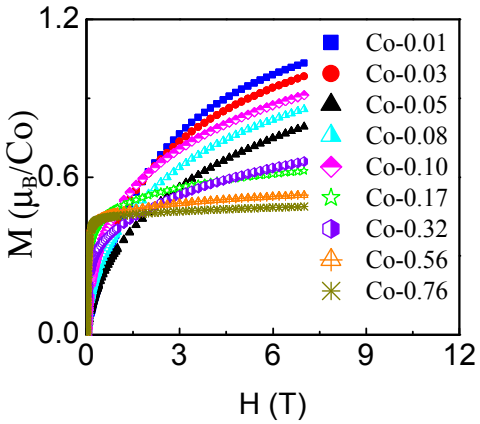

Figure 3.12: Field dependence (H) of magnetic moment $M(\mu_B/\text{Co})$ in $\text{Co}_x\text{Cu}_{1-x}$ at 4 K.

Figure 3.15(a) shows the variations of H_{EB} with the Co content in all Co-x samples at 4 K. The experimental data of the field dependence of magnetization for samples Co-0.01 $\rightarrow$ Co-0.76 shown in the Fig. 3.12.

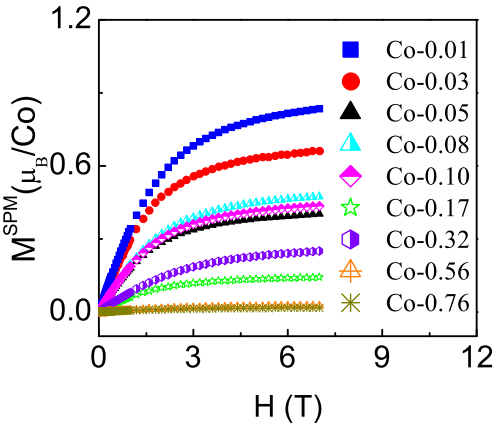

Figure 3.13: Superparamagnetic moment (M^{SPM}) vs. H(T) in $\text{Co}_x\text{Cu}_{1-x}$ at 4 K.

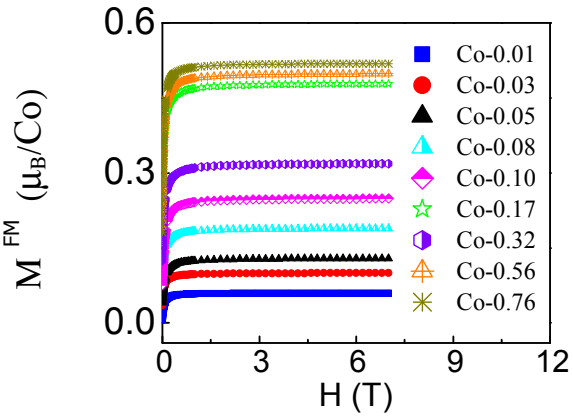

Figure 3.14: Ferromagnetic moment (M^{FM}) vs. H(T) in Co_xCu_{1-x} at 4 K.

At any temperature *Mvs.H* for all samples could be fitted as a sum of superparamagnetic (SPM) and ferromagnetic (FM) components as given by Eq. 3.6. The field variation of superparamagnetic saturation moment and ferromagnetic saturation moment at 4 K are shown in the Fig. 3.13 and Fig. 3.14 respectively.

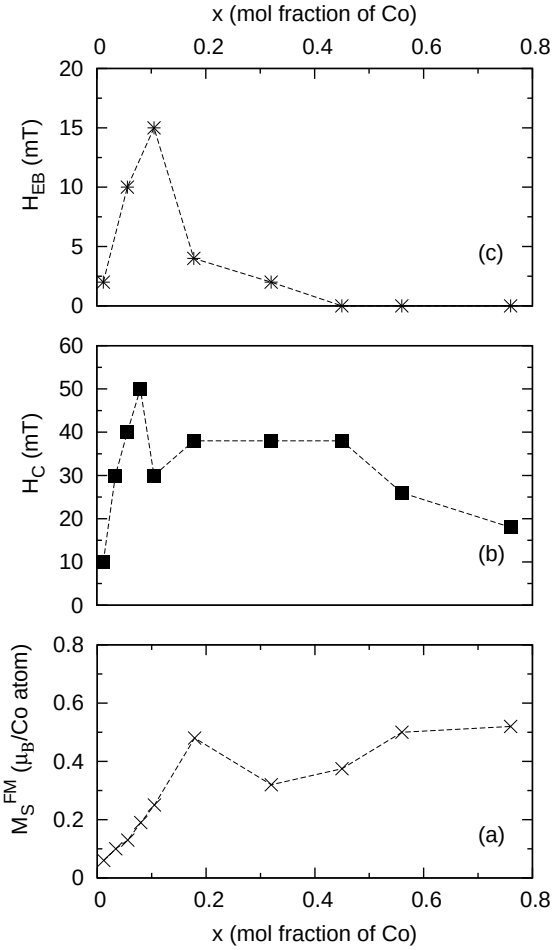

Figure 3.15: Ferromagnetic saturation moment (M_S^{FM}) vs. x in Co_xCu_{1-x}, (b) coercivity (H_C) vs. x, and (c) exchange bias (H_{EB}) vs. x, obtained from data at 4 K. The broken lines are guide to the eye.

In case of annealed Co-0.32, the field dependence (H) of magnetic moment $M(\mu_B/\text{Co})$ has been studied at various temperatures 4-300 K. The results show that the FM component which saturates at $\sim$ 1 T yields an average magnetic moment of 0.32 μ_B per Co atom at 4 K that reduces to 0.11 μ_B per Co atom at 300 K. The magnetic moment of a SPM particle or cluster has a size of 8 μ_B at 4 K and grows to 10^4 μ_B at 300 K. A comparison of these values with corresponding values of as-prepared sample (shown in

Sec. 3.1.3) shows that annealing results in an increase of ferromagnetism of the particles. However, even at 4 K, cobalt magnetic moment in $Co_{0.32}Cu_{0.68}$ is much smaller than Co moment in nanostructured or even bulk cobalt [111] suggesting that not all the cobalt atoms are ferromagnetic in $Co_{0.32}Cu_{0.68}$.

Figure 3.15(b) and (c) show the variations of M_S^{FM} and H_C with the Co content in all Co-*x* samples at 4 K. In this figure we see that in samples with $0.01 \leq x \leq 0.17$, M_S^{FM} increases with Co content. Further increasing the Co content, M_S^{FM} initially appears to decrease, but then increases and tends to level off at values of $\sim 0.5\mu_B/Co$ in Co-0.76. Even at this high cobalt containing sample, the saturation magnetic moment of cobalt remains much smaller than the reported value, $2.2\mu_B/Co$, of Co nanoparticles. The result definitely shows that there exists no long range magnetic interaction in this system of alloys. It will be described in the following sections that the samples yield strong magnetic memory effect at all temperatures 4-300 K as a consequence of the absence of long range magnetic interaction. H_C initially increases rapidly with *x* and shows a peak value of ~ 50 mT in Co-0.08, then becomes smaller in $0.1 \leq x \leq 0.32$ having values ~ 40 mT, and tends to decrease as Co content increases further. H_{EB} also increases with *x* initially and has a maximum value of 15 mT in Co-0.10. It then decreases with increasing Co content and becomes negligibly small in $0.32 \leq x \leq 0.76$.

3.2.3 DC relaxation study

In dc relaxation study the sample was first cooled down from room temperature to a lower temperature in zero magnetic field. A magnetic field of 1 T was applied for 3600 s. Immediately after switching off the magnetic field, the time dependence of dc magnetization $M(t)$ was recorded for 10000 s. Figure 3.16(a) shows the normalized magnetization $M(t)/M(0) vs. t$ for different temperatures for the sample $Co_{0.32}Cu_{0.68}$. The

relaxation data was fitted by a sum of two exponentially decaying components (Eq. 3.12),

$$M(t) = (1-M)\exp(-\frac{t}{\tau_1}) + M\exp(-\frac{t}{\tau_2}) \tag{3.12}$$

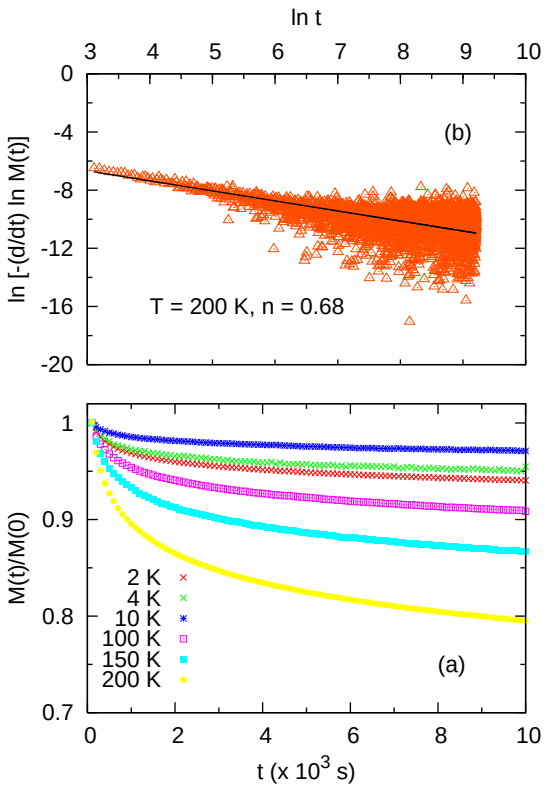

Figure 3.16: (a) For $Co_{0.32}Cu_{0.68}$, time (t) decay of normalized magnetization $(M(t)/M(0))$ at various temperatures in between 2 to 200 K; (b) From the time (t) decay of normalized magnetization, as shown in Fig. 3.16(a), the logarithm of both sides of Eq. (3.13) have been plotted for the data at 200 K. The slope of the linear fit of the data yields n.

in which, $\tau_1 << \tau_2$. On the right hand side of the equation it is the second component, *i.e.*, the one with long relaxation time that is dominant with M being larger than 0.8 at all temperatures. Even at higher temperatures, the magnetization has a long relaxation time signifying a negligible interaction among the *supermoments*. Over and above the slow relaxation of magnetization, it is interesting to note that in between 2-10 K, $M(t)/M(0)$ in this ZFC protocol increases with increase in temperature. This anomalous behavior is

evidently a signature of the onset of spin-glass like ordering. Figure 3.17(a) shows the time decay of normalized magnetization $(M(t)/M(0))$ at 4 K for samples Co-0.01 $\rightarrow$ Co-0.56. Figure 3.17(b) shows the behavior of relaxation time τ_2 with the molar fraction of Co in the sample. It must be noted that τ_2 is very long, $\sim 10^6$ s, and therefore not quite feasible to be measured accurately. The same data are listed in Table 3.3, and show that τ_2 increases with Co concentration.

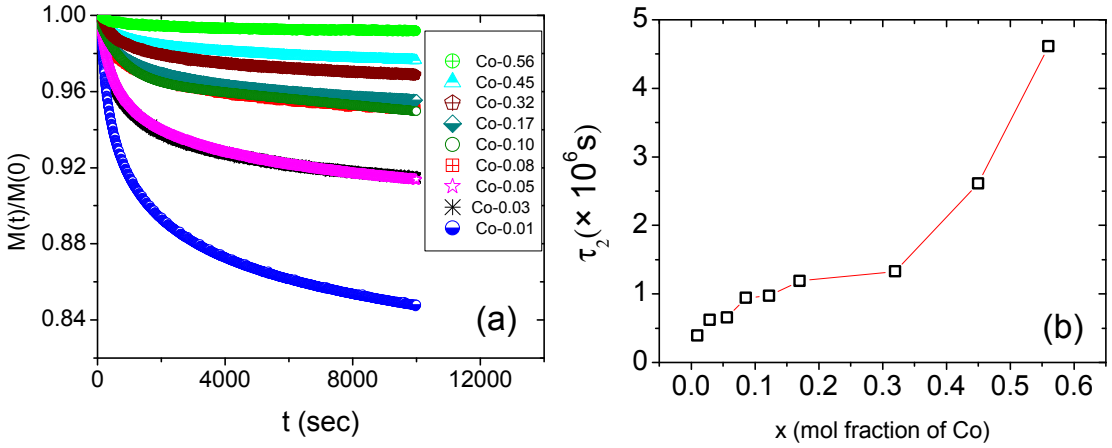

Figure 3.17: (a) Time (t) decay of normalized magnetization $(M(t)/M(0))$ at 4 K for samples Co-0.01 $\rightarrow$ Co-0.56; (b) The estimated relaxation time (τ_2) obtained from Fig. 3.17 (a). The line is a guide to eye.

According to the relaxation mechanism proposed by Ulrich *etal*., the decay $M(t)$ follows the relation [41, 173],

$$-(d/dt)lnM(t) = At^{-n} \tag{3.13}$$

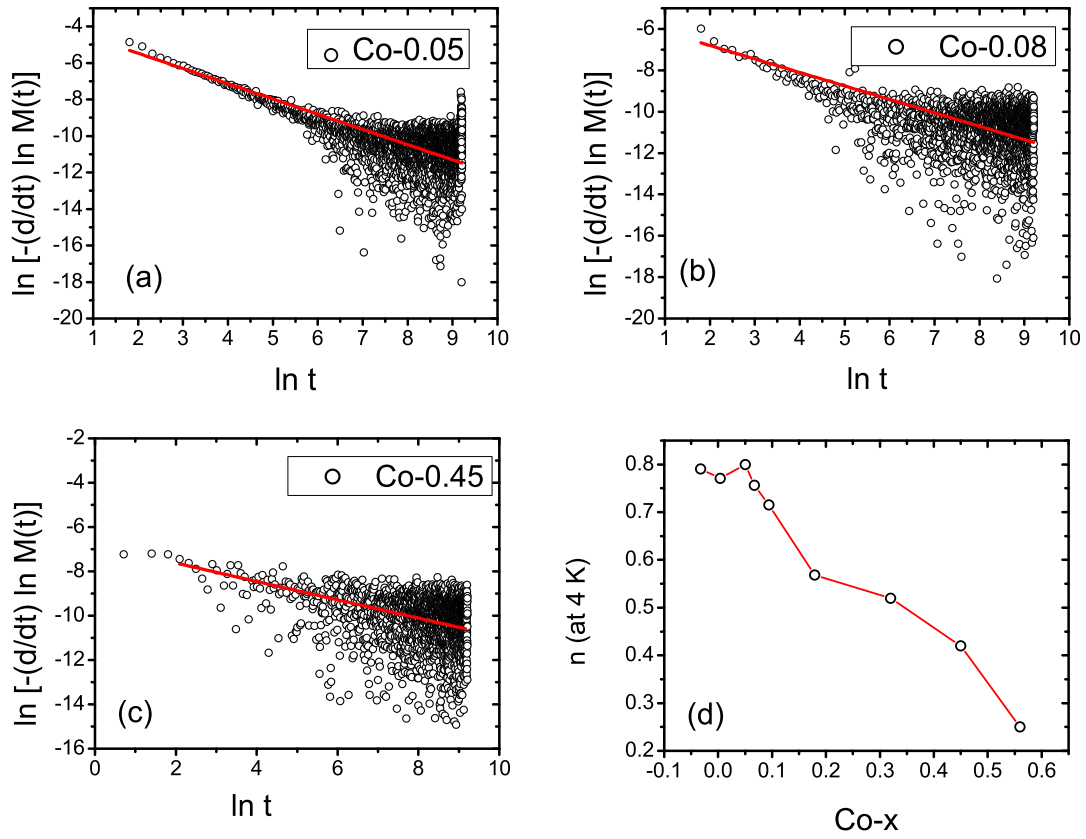

Figure 3.18: From the time (t) decay of normalized magnetization, as shown in Fig. 3.17(a), the logarithm of both sides of Eq. 3.12 have been plotted for the data at 4 K, (a) Co-0.05; (b) Co-0.08; (c) Co-0.45; (d) The slope of the linear fit of the logarithm of both sides of Eq. 3.13 which yields n vs. Co-content (x) (the line is a guide to the eye).

where, A is a constant and n denotes the strength of inter-particle dipolar interaction and is a function of temperature and particle density. The above equation has been used to calculate the value of n as for example shown in Fig. 3.18 for the samples, (a) Co-0.05; (b) Co-0.08; and (c) Co-0.45 for data at 4 K and in Fig. 3.16(b) for Co-0.32 sample at 200 K. The variation of n with the molar fraction of Co is shown in Fig. 3.18(d). Also, Table 3.3 lists the values of n and τ_2 for all samples at 4 K. In case of strongly interacting system with dense particle distribution, n is ≥ 1. For weakly interacting system like dilute FM

nanoparticles embedded in a nonmagnetic metal matrix, n should be ~ 0.6. In our samples n is about 0.8 in low Co samples at 4 K and decreases to less than 0.4 in high Co samples (Table 3.3 and Fig. 3.18(d)). We have checked that in Co-0.32 sample in between 2 to 300 K the value of n varies in between 0.52 - 0.68. The behavior of τ_2 and n indicate that magnetically the Co-Cu alloy system becomes increasingly non-interacting with increase in Co content, or, in other words, as Co increases more and more disorder is introduced in the system.

3.2.4 Memory effect

The memory effect was studied following the same protocols as proposed by Sun *et al.* [36]. Figure 3.19(a) shows the data for Co-0.32 sample. The sample was cooled at the rate of 1K/min from 380 K in presence of 10 mT magnetic field and the data recorded during cooling. At T_{stop} of 300 K, the measurement was stopped, magnetic field switched off immediately, and the magnetic state of the sample was left to relax for a duration (t_w) of 12000 s. After this relaxation the same magnetic field (10 mT) was reapplied and the magnetization data recorded down to 4 K with more stops at T_{stop} of 100, 50, 10 and 4 K, where magnetic field was temporarily switched off for t_w of 12000 s with no measurement. This cooling protocol resulted in a step-like $M(T)$ curve. Finally, after reaching 4 K, the sample in 10 mT magnetic field was heated back continuously at the same rate (1 K/min) and the magnetization was recorded. Despite the continuous heating, the $M(T)$ curve obtained in this way exhibits a clear upturn at each T_{stop}, resembling the previous step-like shape and revealing the previous history of zero-field-relaxation at that T_{stop}. This curve is referred to as the *memory* curve. Step like memory effect appear in FC magnetization of a nanoparticle system, whether non-interacting or interacting, whenever there is a particle size distribution, and therefore, a distribution in blocking temperature [34, 35, 41]. In our sample, the blocking temperature has an upper limit of $\sim$ 380 K, and significant memory

effect persists even at 300 K. Figure 3.20, Fig.3.21 and Fig 3.22 show the the same step like memory effect in temperature (T) dependence of magnetization (M) during FC cooling in 10 mT magnetic field with cooling temporarily stopped for t_w of 8000 s at each of temperatures (T_{stop}), followed by $Mvs.T$ under conditions of continuous heating in 10 mT in sample of the samples Co-0.05, Co-0.10, and Co-0.45 respectively.

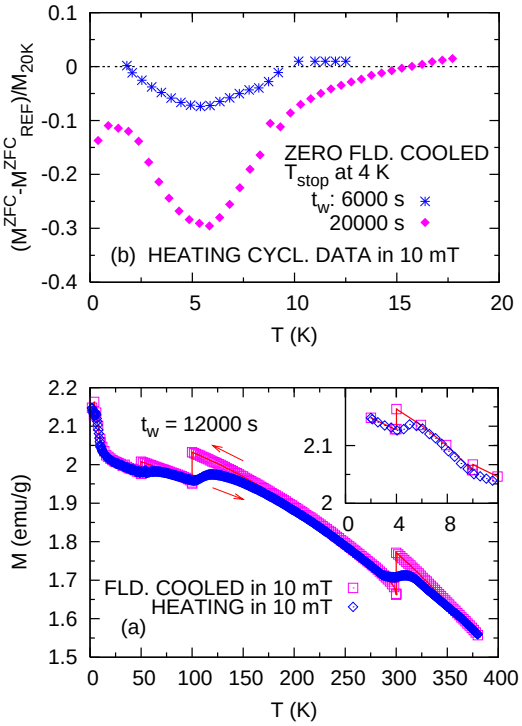

Figure 3.19: (a) For Co-0.32 sample, temperature (T) dependence of magnetization (M) during cooling in 10 mT magnetic field (squares) with cooling temporarily stopped for t_w of 12000 s at each of temperatures (T_{stop}) of 300, 100, 50, 10 and 4 K, followed by $Mvs.T$ under conditions of continuous heating in 10 mT (rhombuses). Inset shows same data for expanded low temperature region; (b) the difference of M^{ZFC} and M^{ZFC}_{REF}, both measured during continuous heating in 10 mT following zero-field cooling. For M^{ZFC} there was temporary stop at 4 K during zero-field cooling. The data were taken twice; for t_w of 6000 s (stars) and 20000 s (filled symbols).

A non-interacting or weakly interacting SPM material shows memory effect only in FC protocol, whereas, spin-glass shows in both FC and ZFC protocols. Therefore, the magnetic state below 7 K has been probed using memory effect in ZFC magnetization

following a procedure suggested by Sasaki *et al.* [34]. The sample was cooled rapidly in ZFC mode from 380 to 2 K with an intermediate stop t_w of 6000 s and 20000 s at 4 K. The magnetization data, denoted as M^{ZFC}, was recorded during the heating cycle from 2 to 300 K with an applied field of 10 mT. The conventional ZFC magnetization, *i.e.*, without the stop, was also recorded and denoted as M_{REF}^{ZFC}. The difference curves of M^{ZFC} minus M_{REF}^{ZFC} as a function of temperature for both stopping times showed a dip just above the stopping temperature, *i.e.*, at 5.5 K as shown in Fig. 3.19(b). When the intermediate stop was given at a slightly higher temperature 10 K, there was no such dip in the difference curve.

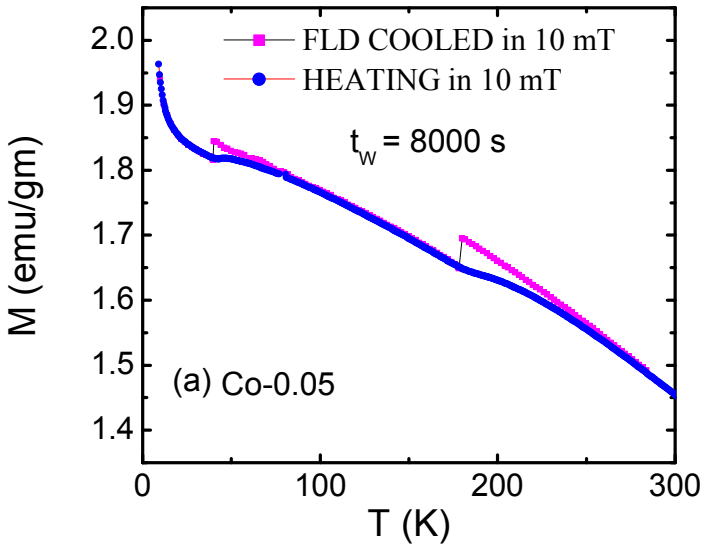

Figure 3.20: Temperature (T) dependence of magnetization (M) during cooling in 10 mT magnetic field (squares) with cooling temporarily stopped for t_w of 8000 s at each of temperatures (T_{stop}) of 180, and 40 K, followed by $Mvs.T$ under conditions of continuous heating in 10 mT (rhombuses) in sample Co-0.05.

In a non-interacting system, there is no memory effect in ZFC process, as below the blocking temperature, a particle can align itself as either up or down spin with equal probability according to the two-state model, and there is no difference in the

magnetization data with and without the intermediate stop during cooling. But inter-particle or inter-cluster interaction appearing below the spin-glass transition produces a number of equilibrium states with different energy barriers. The depth of the energy barrier of the state in which the system is blocked depends on the waiting time, as it happens in annealing. Afterwards, during the heating cycle, the response of the spin system to the magnetic field becomes sluggish in overcoming the energy barrier, thus producing the dip in the difference of magnetization with and without the intermediate waiting.

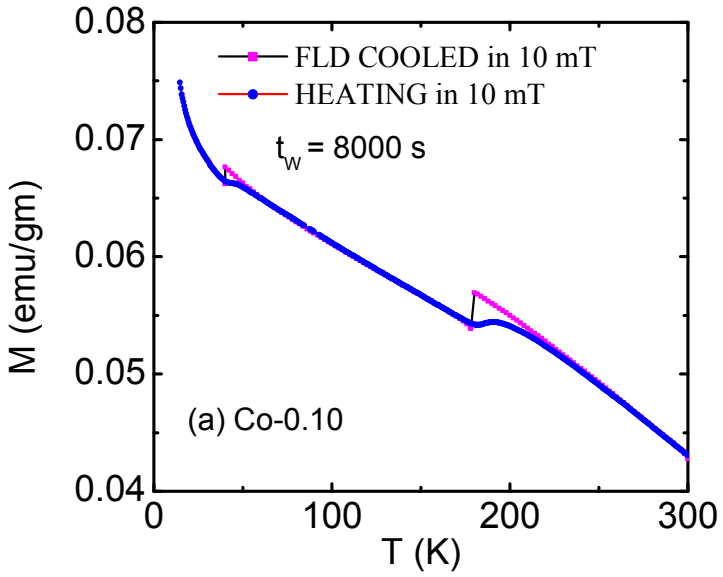

Figure 3.21: Temperature (T) dependence of magnetization (M) during cooling in 10 mT magnetic field (squares) with cooling temporarily stopped for t_w of 8000 s at each of temperatures (T_{stop}) of 180, and 40 K, followed by $Mvs.T$ under conditions of continuous heating in 10 mT (rhombuses) in sample Co-0.10.

Memory effect has been further investigated by studying relaxation dynamics using the experimental protocol of Sun et al. Magnetic relaxation at 100 K measured in 10 mT field after zero field cooling from 380 K is shown in Fig. 3.23(a). Initially, the magnetic relaxation measurement was performed for time t_1. At the end of t_1, magnetic field was switched off and relaxation was further recorded in zero-field through time t_2. Finally,

relaxation was again recorded for time t_3 in the presence of 10 mT magnetic field. Magnetic relaxation of times t_1 and t_3 are shows a single functional dependency with time, as shown in the inset of Fig. 3.23(a). So, the relaxation at time t_3 regains the memory of the previous state, *i.e.*, before temporary switching off the field, when the field is again switched on.

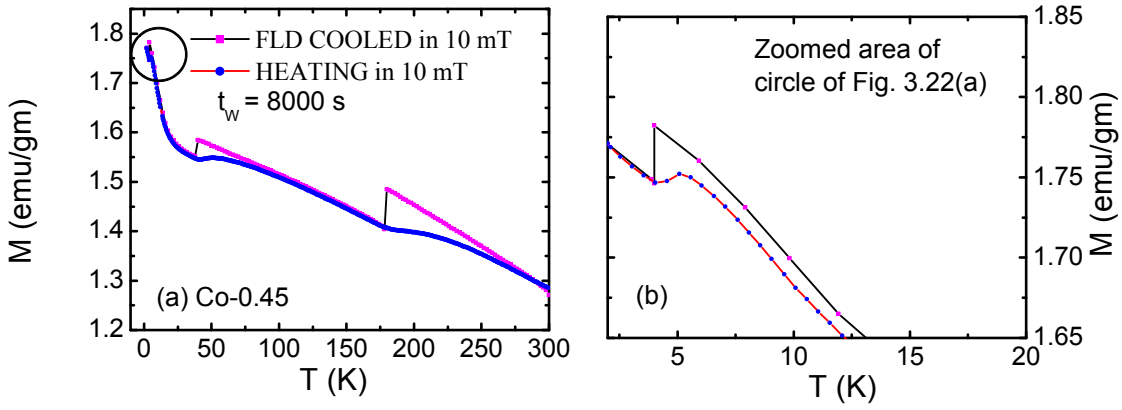

Figure 3.22: Temperature (T) dependence of magnetization (M) during cooling in 10 mT magnetic field (squares) with cooling temporarily stopped for t_w of 8000 s at each of temperatures (T_{stop}) of 180, and 40 K, followed by $Mvs.T$ under conditions of continuous heating in 10 mT (rhombuses) in sample Co-0.45; (b) same data for expanded low temperature region.).

In the next experiment (Fig. 3.23(b)), initially the magnetic relaxation data was recorded for time t_1 at 100 K in 10 mT field after zero-field cooling from 380 K. After the time t_1, the sample was cooled down to 50 K and relaxation was recorded for time t_2. Finally, the sample was heated back to 100 K and relaxation was allowed for time t_3. Here also we see that the relaxation in time t_3 is just the continuation of relaxation at time t_1, as shown in inset of Fig. 3.23(b).

In another experiment (Fig. 3.23(c)), the sample was cooled from 380 K to 100 K in 10 mT. Then the magnetic relaxation data was recorded for time t_1 in zero field condition. After t_1 the sample was cooled down to 50 K and the magnetic relaxation data was saved

for time t_2. Finally after t_2 the sample was heated back to 100 K and relaxation performed for time t_3. Here also the relaxation for time t_3 is just a continuation of the relaxation in time t_1, which is shown in the inset of Fig. 3.23(c). The relaxation curves in insets of the Fig. 3.23(c) fit satisfactorily with an exponential function of the type, $M(t) = M_0 + A_n exp(-\tau_n/t_n)$, with the characteristic times τ_n same for t_1 and t_3.

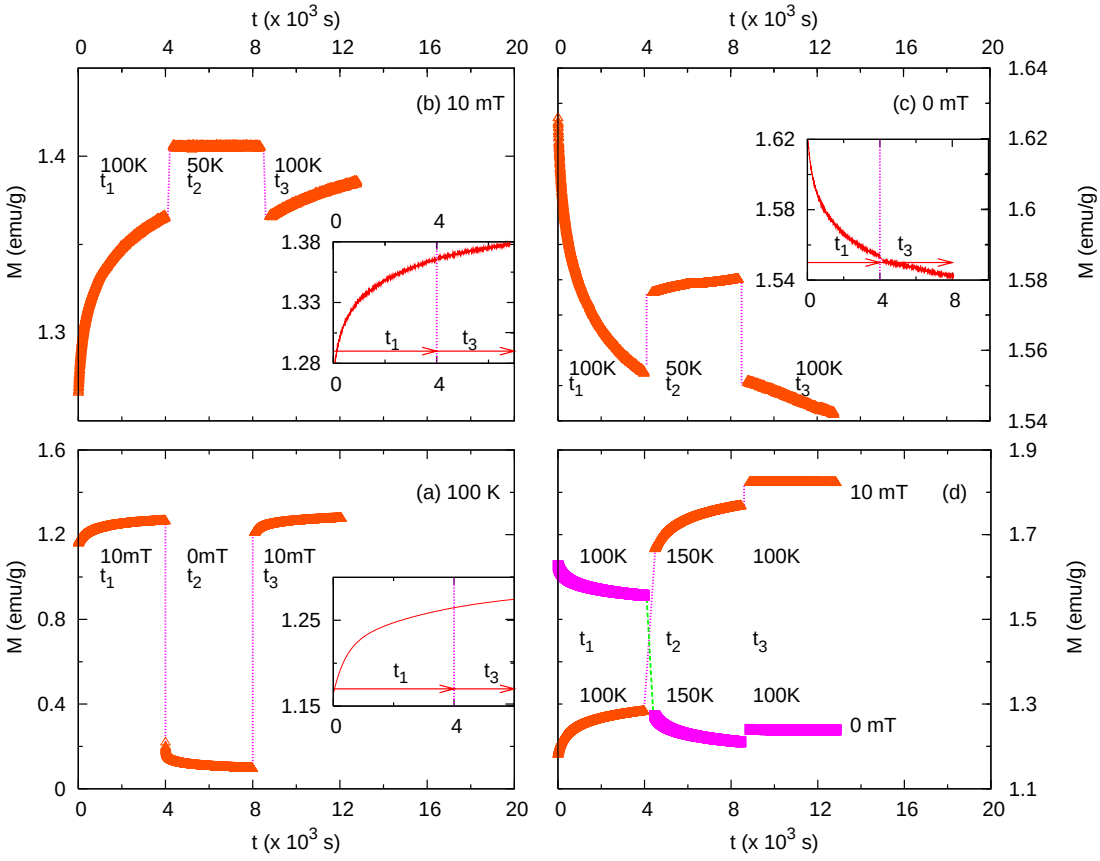

Figure 3.23: (a) For Co-0.32 sample, magnetic relaxation at 100 K and 10 mT for t_1 and t_3 after cooling in ZFC mode with an intermediate measurement in zero-field for t_2. Inset shows the relaxation in 10 mT only. (b) Relaxation at 100 K and 10 mT for t_1 and t_3 after ZFC with an intermediate cooling at 50 K for t_2. Inset shows the relaxation at 100 K only. (c) Relaxation at 100 K at 0 mT for t_1 and t_3 after FC in 10 mT with an intermediate cooling at 50 K for t_2. Inset shows the relaxation at 100 K only. (d) Magnetic relaxation in zero and 10 mT after cooling in FC and ZFC modes, respectively, with an intermediate heating at 150 K.

In the last two measurement protocols, we observed that the memory effect was strongly present after temporary cooling of the sample at low temperature. We also

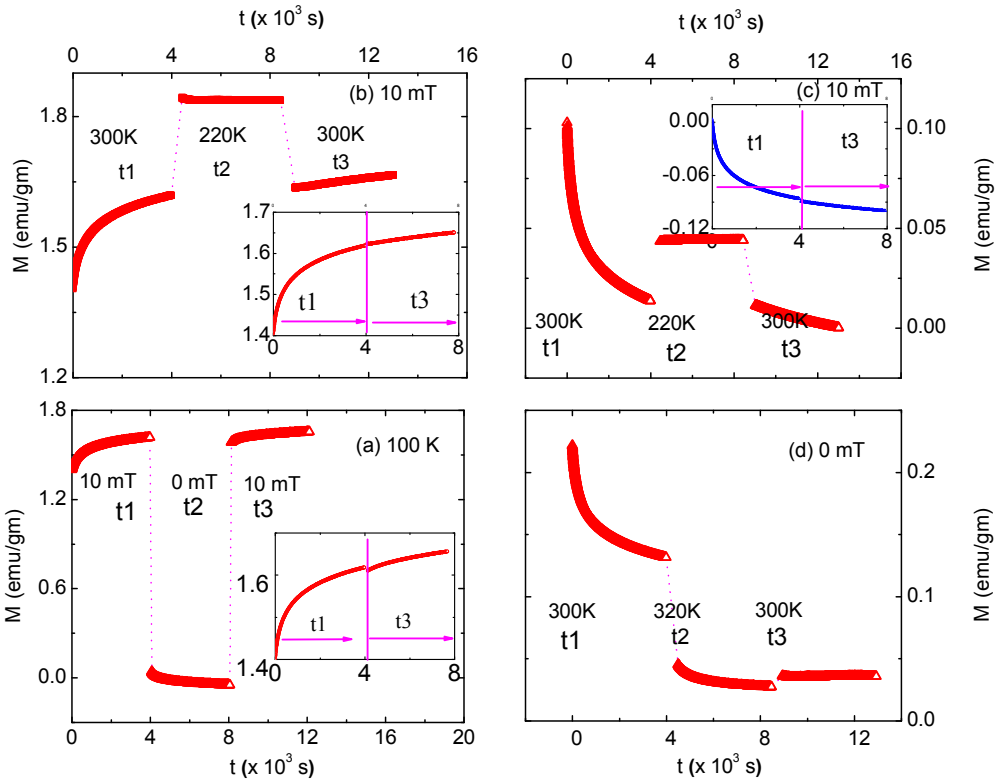

Figure 3.24: (a) For Co-0.32 sample, magnetic relaxation at 300 K and 10 mT for t_1 and t_3 after cooling in ZFC mode with an intermediate measurement in zero-field for t_2. Inset shows the relaxation in 10 mT only. (b) Relaxation at 300 K and 10 mT for t_1 and t_3 after ZFC with an intermediate cooling at 220 K for t_2. Inset shows the relaxation at 300 K only. (c) Relaxation at 300 K at 0 mT for t_1 and t_3 after FC in 10 mT with an intermediate cooling at 2200 K for t_2. Inset shows the relaxation at 300 K only. (d) Magnetic relaxation in zero after cooling in FC modes, respectively, with an intermediate heating at 320 K.

compared the states of magnetization before and after a temporary heating of the sample. The sample was cooled from 380 K to 100 K in zero field cooled condition. The magnetic field of 10 mT was switched on and the growth of $M(t)$ was recorded for time t_1 at 100 K. The sample was heated to 150 K and the relaxation experiment performed for the time t_2. After completion of time t_2 the sample was cooled back to 100 K and the relaxation data was recorded during time t_3. In this experiment it was observed that the relaxation at times t_1 and t_3 are in different state. The observation was the same when the sample was initially cooled in 10 mT and then switched off to study relaxation using the same protocol, in this case recording the decay of $M(t)$. So, both in presence or absence of magnetic

field, the sample does not regain its previous magnetization state after intermediate heating [110, 174, 175]. Results of these two experiments are shown in Fig. 3.23(d).

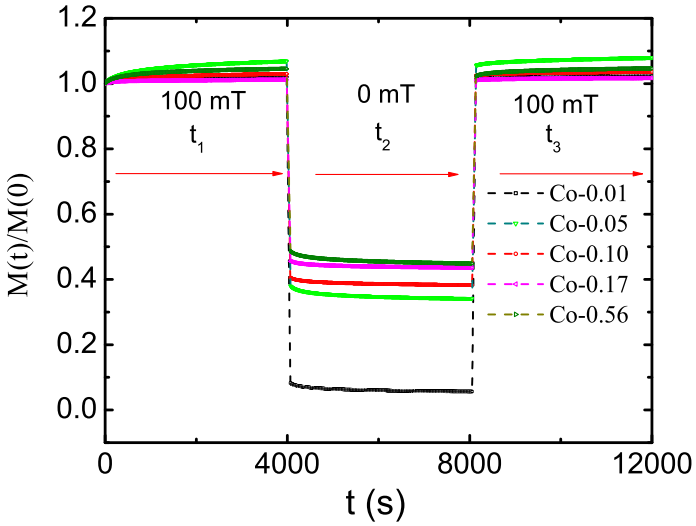

Figure 3.25: Magnetic relaxation at 300 K and 10 mT for t_1 and t_3 after cooling in ZFC mode with an intermediate measurement in zero-field for t_2 for the samples Co-0.01→ Co-0.56

The above memory effects including the loss of memory upon intermediate heating of the sample can be explained by the hierarchical model [41, 122], originally proposed for interacting particle system. However, earlier it was shown [38] that the same effect can be obtained in a non-interacting superparamagnetic system having a particle size distribution, wherein, a distribution of anisotropy energy barriers and blocking temperatures create a set of free energy states. After temporary cooling only smaller nanoparticles are able to respond to the temperature or field change and relax to the new equilibrium state. The larger nanoparticles are frozen. Upon returning to the initial temperature or field value, the smaller particles rapidly respond to the change such that this new state is essentially the same as that before the temporary cooling, and the larger nanoparticles are now able to resume relaxing to the equilibrium state. This results in a continuation of the magnetic relaxation after the temporary temperature or field change. In contrast, for positive heating, all the particles, smaller as well as bigger, are able to respond to the temperature or field

change. Therefore, after returning to the initial temperature, the bigger particles do not respond at all whereas the smaller particles take time to respond, thus leading to no memory effect in the positive heating cycle. The same magnetic relaxation experiments described above were repeated at 300 K, after cooling the sample from 380 K in presence or absence of magnetic field, as the experiment required and the results are presented in Fig. 3.24. Fig 3.25 shown the memory effect in magnetic relaxation at 300 K and 10 mT for t_1 and t_3 after cooling in ZFC mode with an intermediate measurement in zero-field for t_2 for the samples Co-0.01$\rightarrow$ Co-0.56. Strong memory effect persists even at room temperature

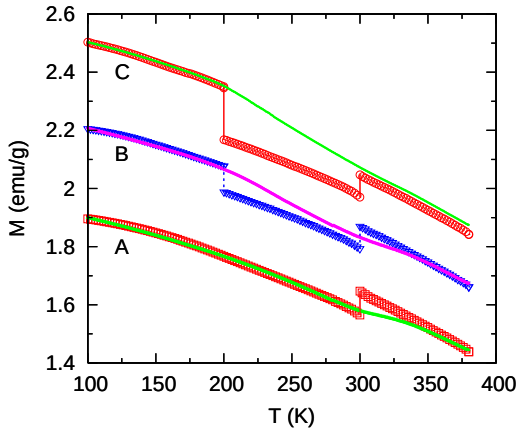

Figure 3.26: For Co-0.32 sample, temperature (T) dependence of magnetization (M) in 10 mT magnetic field (H) during interrupted cooling (open symbols) followed by continuous heating (lines). Cooling was stopped for t_w of 12000 s at 300 K (data A) and at 300 and 200 K (data B and C). At 300 K, during t_w, H was set to zero in A, B and C. At 200 K, during t_w, H was 20 mT in B and 30 mT in C.

and have been observed for magnetic field changes from 10 mT to 2 T. However, in such single domain nanoparticle systems, the ability to store the memory of successive magnetic field changes is restricted to small magnetic fields, and the memory of one field variation is erased by another field change beyond a critical value afterwards [174]. We have found the critical $'erasing'$ field for our system at 300 K. M versus T in a measuring field of 10 mT was obtained during cooling the sample from 380 K. At T_{stop} of 300 K, field switched off and cooling temporarily stopped for t_w of 12000 s. At the end of t_w, the same measuring

field was applied and M versus T data recorded down to 100 K. The continuous heating cycle data from 100 to 380 K was taken with the same 10 mT measuring field. The result is shown in Fig. 3.26, data A. In the following two runs, using the same measuring field of 10 mT and identical T_{stop} at 300 K, one more T_{stop} at 200 K was given for t_w of 12000 s during which the magnetic field was raised to 20 mT (data B) and 30 mT (data C). The continuous heating cycle data show wiggle near 300 K in data A and B, but not in C. Thus, erasing the memory of a magnetic field variation at 300 K requires a later variation of magnetic field by only about three times the original variation, which would make this kind of granular alloys technologically interesting in regard to coding-decoding and erasing of data.

3.3 Transport study

Resistivity measurements were performed with a Physical Properties Measurement System (PPMS 9 of Quantum Design) using four-probe method and a constant current of 60 mA. Figures 3.27(a) and (b) show resistivity as a function of temperature (ρ) in between 2-300 K in zero external magnetic field for some of the samples. For convenience, $(\rho - \rho_{min})$ is plotted in this figure. For low Co containing samples, Co-0.01, Co-0.03, and Co-0.08, a metallic resistivity behavior is observed. It decreases as temperature decreases from 300 K down to $\sim$ 10 K, and there is a residual resistivity below 10 K where $(\rho - \rho_{min})$ levels off to zero (Fig. 3.27(a)). For higher Co containing samples, Co-0.17, Co-0.56 and Co-0.76 (Fig. 3.27(b)), the resistivity is much higher and the zero in $(\rho - \rho_{min})$ is obtained at a finite temperature T_{min} which is seen clearly in Fig. 3.27(c). Figure 3.27(c) shows that T_{min} increases with x, and also the minimum becomes more pronounced with x, *i.e.*, the depth of the resistivity minimum which may be defined as $(\rho_{5K} - \rho_{T_{min}})$, increases with x.

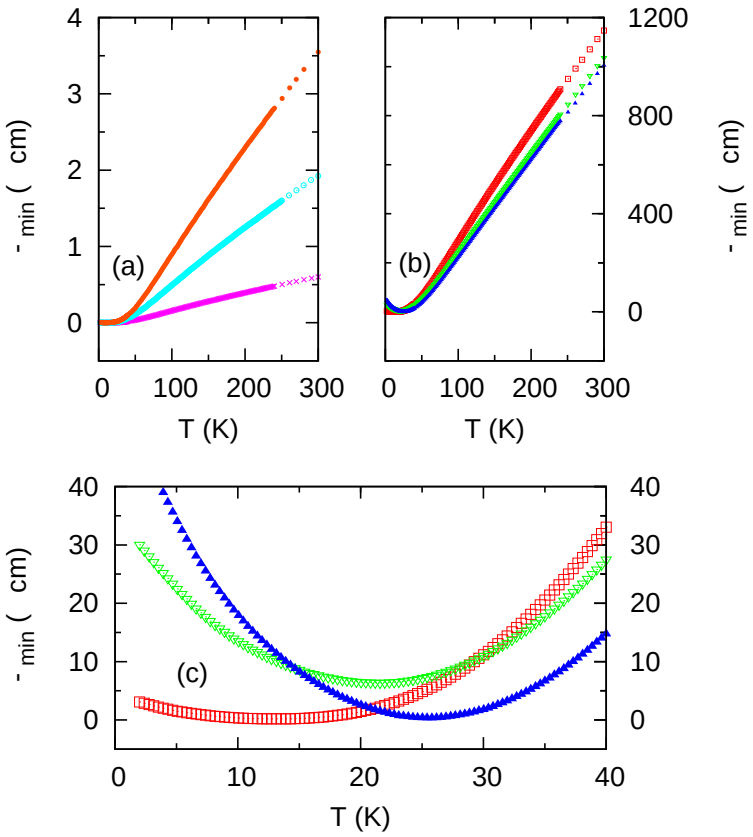

Figure 3.27: Resistivity (ρ) as a function of temperature for (a) samples Co-0.01 ($\times$), Co-0.03 ($\circ$) and Co-0.08 ($\bullet$); (b) samples Co-0.17 ($\square$), Co-0.56 ($\triangledown$) and Co-0.76 ($\blacktriangle$); and (c) expanded low temperature region of Fig. 3.24(b).

The resistivity for a metallic behavior can be written in the form of a general power law, $\rho = \rho_0 + \rho_P T^P$, in which ρ_0 is the residual resistivity and the other term represents the combined effect of inelastic electron-electron, electron-phonon and electron-magnon scattering contributions. In granular alloy and other systems, the resistivity upturn in low temperature can have its origin in different mechanisms like Coulomb blockade effect,[176] electron-electron scattering and Kondo effect. For Coulomb blockade(CB) effect the resistivity is empirically given as,

$$\rho = \rho_0 + \rho_{CB} exp(\frac{\Delta}{T})^{1/2} + \rho_P T^P \tag{3.14}$$

where Δ is Coulomb energy required to generate a charge carrier, in which an electron is removed from a neutral grain and placed on a neighboring neutral grain [177].

An upturn in resistivity may also result from tunneling of spin-polarized conduction electrons between neighboring grains whose magnetic moments are not parallel [178],

$$\rho = \frac{r_1 + r_2 T^{3/2}}{1 + \varepsilon < cos\theta_{ij} >} \tag{3.15}$$

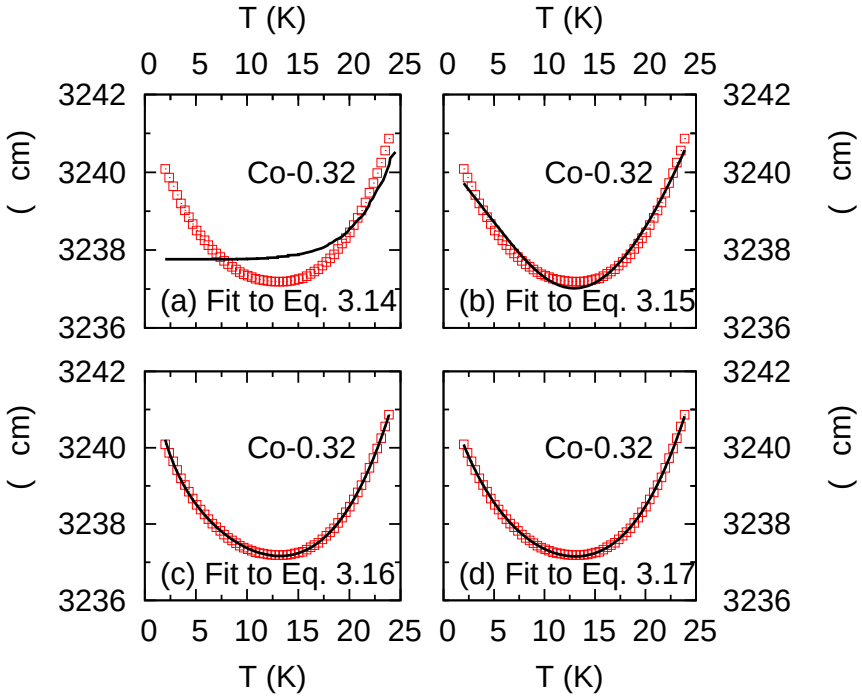

Figure 3.28: Fitting of low temperature resistivity upturn of Co-0.32 sample. The experimental data (□) are fitted (solid line) for (a) Coulomb blocking effect (Eq. 3.14); (b) inter-grain tunneling of electrons (Eq. 3.15); (c) Kondo effect (Eq.3.16); and (d) elastic scattering of electrons (Eq. 3.17).

In the above equation, r_1 and r_2 are field independent parameters and ε represents

the degree of polarization of electrons. In absence of magnetic field, the spin correlation function $< cos\theta_{ij} >$ is given as,

$$< cos\theta_{ij} >= -L(\frac{|J|}{k_B T})$$

where, $L(x) = [coth(x) - 1/x]$ is the Langevin function and J is the inter-grain antiferromagnetic exchange integral.

With the assumption that the upturn is due to Kondo effect, the resistivity at low temperatures can be written as [90],

$$\rho = \rho_0 - \rho_K(T) + \rho_P T^P \tag{3.16}$$

where, $\rho_K(T) = c\rho_m + c\rho_1 lnT$. ρ_m is the spin scattering resistivity and $\rho_1 = \rho_m \frac{(3n_s J_{sd})}{E_F}$, in which, J_{sd} is the $s-d$ exchange interaction between the spins (S_e) of the conduction electrons of Cu and the localized magnetic moment (S_d) of the transition element Co. E_F is the Fermi energy of cobalt and n_s the number of conduction electrons per atom.

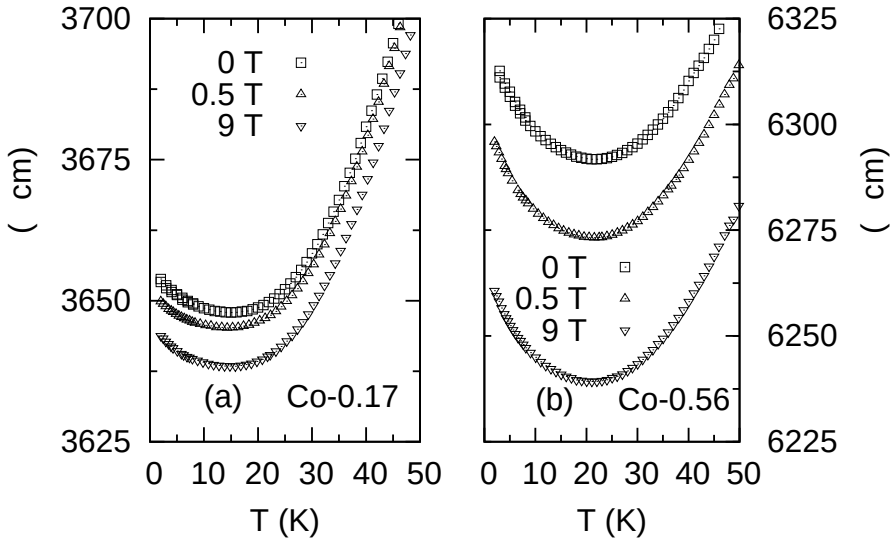

Figure 3.29: Resistivity (ρ) vs. temperature in zero magnetic field and in magnetic fields of 0.5 and 9 T measured in samples (a) Co-0.17; and (b) Co-0.56.

Various non-magnetic and magnetic amorphous and disordered metal alloys exhibit resistivity minimum at low temperature [99, 100, 101]. The origin of minimum in these strongly disordered systems has been attributed to the elastic electron-electron interaction and quantum coherence effect [145], in which the resistivity in the low temperature regime takes the form,

$$\rho = \rho_0 - \rho_e T^{1/2} + \rho_P T^P. \tag{3.17}$$

In the above equation, ρ_e, the elastic scattering coefficient, is given as [104],

$$\rho_e = 0.0309 \frac{{\rho_0}^2 e^2}{\hbar} (\sqrt{\frac{1}{T L_T^2}}) \tag{3.18}$$

where, L_T is the thermal diffusion length, which, for any temperature (T), can be obtained from ρ_e and ρ_0 estimated from fitting of the experimental data with Eq. 3.17. Equations 3.14, 3.15, 3.16 and 3.17 have been used to fit the observed resistivity data. An example is shown in Fig. 3.28 for the fitting of the data of Co-0.32 sample. It is found that at low

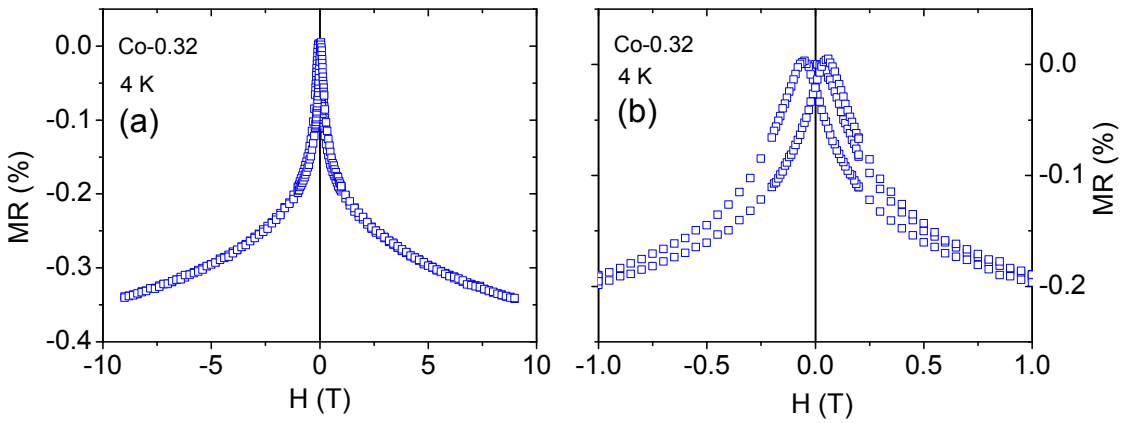

Figure 3.30: (a) Field dependence (H) of magneto resistance (MR %) and $-9 \leq H \leq 9T$ in sample Co-0.32, and (b) expanded low field region of Fig. 3.27(a).

temperatures the data do not fit at all to Eq. 3.14 and they make an unsatisfactory fit to Eq. 3.15. However, the data fit equally satisfactorily to Eqs. 3.16 and 3.17. The data for all the samples $x \geq 0.17$ were fit with Eqs. 3.15, 3.16 and 3.17, and also the magnetic field dependence of resistivity were checked to ascertain the plausible mechanism behind the observed resistivity minimum. Table 3.4, 3.5 and 3.6 give the experimentally obtained temperature of minimum resistivity, T_{min}, and the various fitting parameters corresponding to each equation. The results show that the values of electron polarization (ε) and inter-grain coupling (J) obtained from the fitting with Eq. 3.15 are too small to consider the electron tunneling effect to be responsible for the resistivity behavior. Also, in cases where inter-grain tunneling effect is dominant, the depth of the minimum in resistivity decreases on increasing the magnetic field and the minimum vanishes beyond a certain value of magnetic field [179, 180]. In Fig. 3.29, the zero-field resistivities of two of these samples, *viz*., Co-0.17 and Co-0.56, are shown with the resistivities measured in magnetic fields of 0.5 T and 9 T. It is found that the resistivity minimum is not suppressed even at high magnetic fields. Previously, such low temperature upturns in granular alloys of Au-Ni and Co-Cu were explained by Kondo scattering mechanism involving small clusters of spins and it was also observed [24] that for larger cluster sizes Kondo effect should disappear. In contrary

Table 3.4: For Co_xCu_{1-x} ($0.17 \leq x \leq 0.76$) various parameters obtained from fitting the experimental data with equations corresponding to inter-grain tunneling (Eq. 3.15).

		From Eq. 3.15			
Sample	T_{min}	r_1	r_2	ε	J/k_B
Co-0.17	13.5(5)	1359	0.5	0.01	0.03
Co-0.32	13.5(5)	3196	1.1	0.01	0.03
Co-0.45	16.5(5)	5268	2.8	0.02	0.03
Co-0.56	21.5(5)	7425	2.8	0.02	0.03
Co-0.76	25.5(5)	10390	3.5	0.02	0.03

to this observation, the resistivity upturn in the present case is very much pronounced at high Co concentrations and at low Co concentrations it is not obtained. Moreover, Kondo effect is weakened in presence of a magnetic field. It is indicated from the data of Fig. 3.29 that magnetic fields have negligible effect on both T_{min} and the depth of resistivity minimum. In other words, these samples posses small magneto-resistance, $\sim -0.4\%$ near T_{min} at 9 T (shown in the Fig 3.30). These observations strongly suggest that influence of both inter-grain tunneling [178] and Kondo-like scattering of electrons are absent in the present case, and the observed resistivity minimum possibly arises from elastic scattering of electrons. Also, it is seen in Table 3.6 that ρ_P is orders of magnitude smaller than other resistivity coefficients indicating that inelastic scattering of electrons does not have a significant contribution to resistivity at these temperatures.

The resistivity upturn resulting from Coulomb interaction is due to the quantum interference effect of the electrons. Electrons travel with a characteristic mean free time, τ_e, and mean free path, l_e, between two successive collisions. For elastic scattering, the electrons remain coherent even for distances larger than l_e as energy is conserved. The temperature effect can cause destruction of this quantum coherence of electrons. At low temperatures, the thermal energy is much smaller than the Fermi energy, and the wave functions of the electrons maintain their amplitudes, though the phase vary slightly. If this variation is sufficiently small, thermal energy is unable to destroy the coherence. Under this

Table 3.5: For Co_xCu_{1-x} ($0.17 \leq x \leq 0.76$) various parameters obtained from fitting the experimental data with equations corresponding Kondo scattering (Eq. 3.16).

	From Eq. 3.16			
Sample	ρ_0 ($\mu\Omega$ cm)	ρ_1 ($\mu\Omega$ cm)	ρ_P ($\mu\Omega$ cm)	P
Co-0.17	1382	1.1	$< 10^{-4}$	3.8
Co-0.32	3241	1.8	$< 10^{-4}$	4.1
Co-0.45	5414	4.2	$< 10^{-4}$	4.2
Co-0.56	7641	12.4	$< 10^{-4}$	3.65
Co-0.76	10663	23.5	3×10^{-4}	3.13

condition, the electrons move coherently a long distance. With increase in Co concentration the number of scatters in the path of the coherently mobile electron increases and so increases the event of coherent scattering. This results in the increase of T_{min}, ρ_e and also of L_T with increases in Co concentration. At temperatures above T_{min} the coherence is lost and the resistivity increases with increasing temperature.

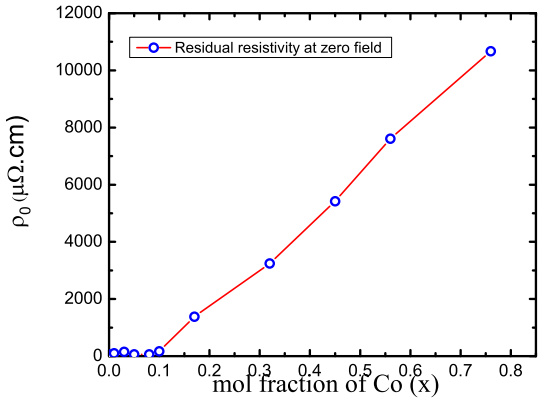

Figure 3.31: Resdual resistivity (ρ_0) as a function of Co content (x).

Table 3.5 and 3.6 list the residual resistivities (ρ_0) for the samples with $x \geq 0.17$ only; however, ρ_0 for low Co containing samples have also been obtained. Figure 3.31 shows the behavior of residual resistivity (ρ) as a function of Co content (x). A pellet of copper only nanoparticles prepared by an identical procedure (*i.e.*, $x = 0$ sample in the

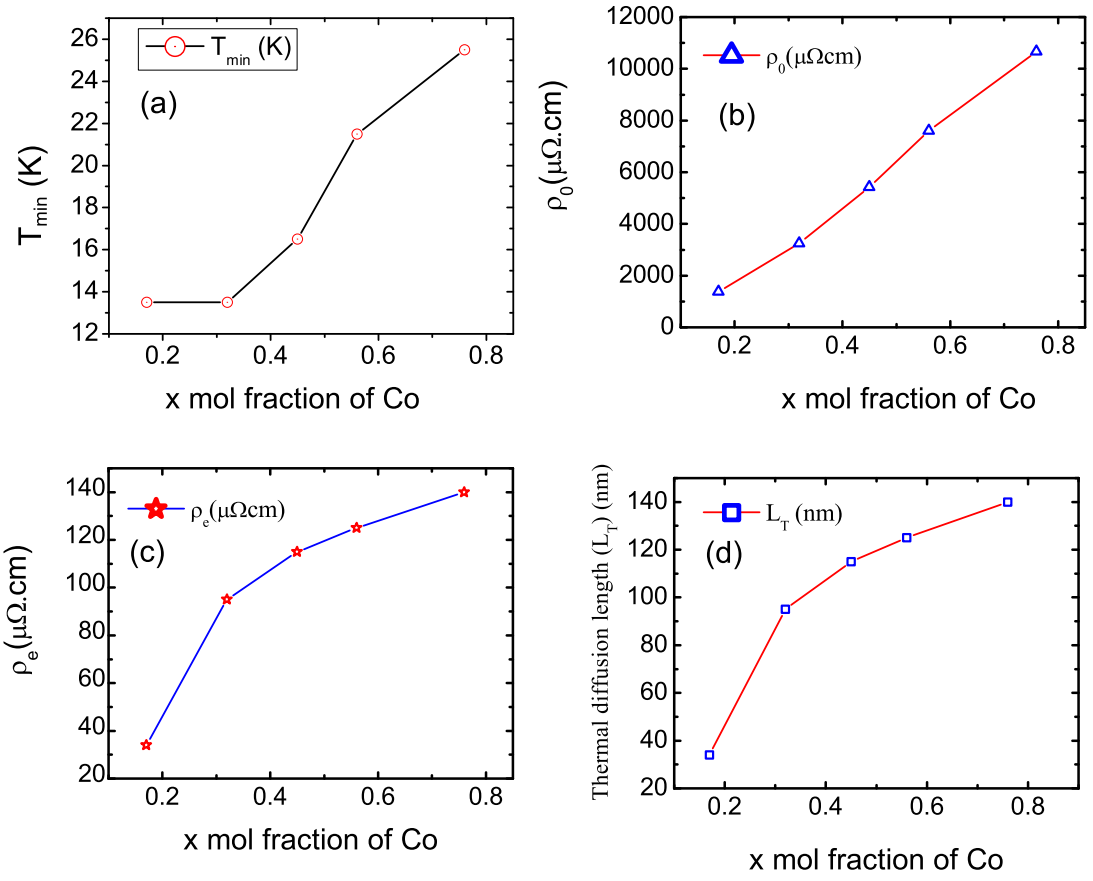

Figure 3.32: Variation of (a) T_{min}; (b) residual resistivity (ρ_0); (c) elastic contribution in resistivity (ρ_e), and (d) thermal diffusion length (L_T) with the molar fraction (x) of Co. The lines are guide to the eye.

present series) shows metallic behavior and yields a ρ_0 of 56$\mu\Omega$cm, which is high compared to ρ_0 of 7$\mu\Omega$cm obtained in a melt-spun CoCu alloy [181]. This increment is probably related to the lump and filament structure (Fig. 2.9(d)) that results in electron flow in narrow meandering channels having a typical width of the order of the particle size, and the resistivity predominantly arises from diffusive scattering at the channel boundaries [182]. In case of alloys, we have found that in low Co samples ρ_0 remain small and close to that of the Cu only sample. But as x increases beyond 0.1, ρ_0 increases continuously and almost linearly with x throughout the range $0.17 \leq x \leq 0.76$ (shown in the Fig 3.31). This systematic variation of ρ_0 most probably reflects a variation in the electron diffusion or scattering mechanism that depends only on cobalt concentration. However, the huge values

Table 3.6: For Co_xCu_{1-x} ($0.17 \leq x \leq 0.76$), temperature of minimum resistivity (T_{min}) and various parameters obtained from fitting the experimental data with equations corresponding to elastic scattering (Eq. 3.17) of electrons. Also given are the thermal diffusion lengths (L_T).

	From Eq. 3.17					
Sample	T_{min} ($\mu\Omega$ cm)	ρ_0 ($\mu\Omega$ cm)	ρ_e ($\mu\Omega$ cm)	ρ_P	L_T (nm)	P
Co-0.17	13.5(5)	1383	1.3	2×10^{-4}	34	2.7
Co-0.32	13.5(5)	3244	2.6	2×10^{-4}	95	2.8
Co-0.45	16.5(5)	5418	8.9	2×10^{-4}	115	2.6
Co-0.56	21.5(5)	7606	11.1	0.003	125	2.4
Co-0.76	25.5(5)	10669	19.3	0.018	140	2.2

of ρ_0, more than two or three orders of magnitude over the values for pure Cu or low cobalt containing bulk alloy is probably related to the microstructure of the system [151].

It is surprising that the resistivity minimum originating from electron-electron interaction is sustained to a very high concentration of Co (Co $\sim$ 76%). Generally in a dense alloy system, the magnetic impurities can not remain isolated and there appears a long range magnetic interaction that dominates $e-e$ interaction. This does not seem to happen in the present case. Indeed, in previously described (Sec. 3.2) magnetic measurements on a similar system of Co_xCu_{1-x} with $x \leq 0.3$ have shown absence of any long range magnetic interaction and indicated that isolated nanoparticles are formed in a core-shell type structure with cluster(s) of cobalt atoms surrounded by copper.

3.4 Co- content (x) dependent model of Co_xCu_{1-x} granular alloy

With the above magnetization results and the observation that the residual resistivity (ρ_0) is small for low Co containing samples and then increases almost linearly with Co

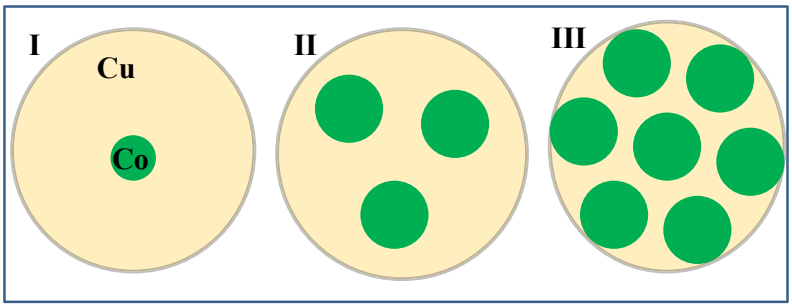

Figure 3.33: A schematic diagram of a particle of Co-Cu alloy with low cobalt content (marked I), intermediate cobalt content (marked II) and high cobalt content (marked III) regions. The particle in all three cases is in the form of cluster(s) of Co atoms within Cu matrix.

content (Table 3.6), we can now construct a model for the formation of these non-interacting CoCu alloy particles. At low Co concentrations (x), there are small cluster(s) of Co atoms surrounded by Cu on all sides (shown in Fig. 3.33 I). Electrical conduction in an assembly of such particles takes place mainly through copper and there is no significant scattering by Co clusters. Thus, a small residual resistance is obtained. At intermediate Co concentrations the cluster size increases with x (shown in Fig. 3.33 II) and as a consequence M_S^{FM}, H_C and also H_{EB} increase (Fig. 3.15). Afterwards, when x goes above a value of ~ 0.16, there is no further increase in the cluster size. Instead, there is an increase only in the number of clusters inside a particle by way of formation of new clusters and also disintegration of existing clusters (Fig. 3.33 III). In this condition, M_S^{FM} tends to level off, and, simultaneously, the boundary between Co clusters and Cu shell possibly become diffused or less well-defined resulting in the decrease and finally disappearance of H_{EB} (also in Fig. 3.15) . Under such condition, a high degree of structural and magnetic disorder is expected to prevail in the system. The fact that ρ_0 begins to increase with x indicates that for higher cobalt the clusters are also at the periphery of the particles and scattering from cobalt clusters dominate in the process of electron conduction.

CHAPTER 4

SUMMARY AND CONCLUSION

4.1 Summary

In this thesis work, a detailed and systematic study to understand the magnetic and transport properties of Co_xCu_{1-x} nanostructured alloys of varying compositions of cobalt ($x \sim 0.01 - 0.76$) have been carried out. The major findings of the thesis work along with the possible further scope of future study in this field are discussed in this chapter.

The first chapter gives a brief introduction, motivation and scientific background of magnetism in nanoparticle systems.

The second chapter thoroughly describes the sample preparation method, and structural, chemical and microscopic characterizations of the system using different techniques. Co_xCu_{1-x} ($x \sim 0.01 - 0.76$) granular alloys were prepared by chemical reduction of $CoCl_2$ and $CuCl_2$ in solution with *CTAB* being used for capping of the alloy particles. Average cobalt content (x) in these alloys were obtained from inductively coupled plasma optical emission spectroscopic (ICPOES) measurements. Transmission electron microscopy

(TEM) results showed particles of mean size ~ 15 nm existing in lumps and filament-like formations. The measured lattice spacings from selected area diffraction (SAD) pattern confirms that the alloy is formed in fcc crystalline phase as in copper.

In the third chapter, first we have presented the details of magnetization study of as-prepared samples. Lowest Co-content $\sim 0.01 mol\%$ sample shows identical paramagnetic behavior in both ZFC and FC magnetization measurements. For other samples, there is a peak in ZFC magnetization at a certain temperature and ZFC/FC magnetization bifurcate at a higher temperature, which for high Co containing samples is close to room temperature. Samples are characterized by blocking temperature (T_B) distributions of SPM clusters resulting from variations in particle size and inhomogeneities in their chemical compositions. Such variations are reflected also in data obtained from TRM studies. All the samples except Co-0.01 exhibit hysteresis loops at 4-300 K. Analysis shows that FM contribution increases and SPM contribution decreases with increase in Co content. At low Co concentration the sample is entirely superparamagnetic but at high Co concentration the sample magnetization is a combination of superparamagnetism and ferromagnetism. It is clear from the above results that in samples $\sim 0.01 - 0.33 mol\%$, there is a FM part growing in size with Co content, together with a SPM part. As the samples have almost the same average saturation magnetic moment per Co atom independent of Co concentration, there is a possibility of occurrence of a Co rich core and Cu rich shell type structure. The coercivity values yield the magnetic anisotropy constant which is $\sim 10^8$ erg/cm^3, *i.e.*, about 2 orders of magnitude higher than that of bulk cobalt.

Secondly, we have studied the exchange bias, magnetic relaxation and memory effect for annealed Co-0.33 sample. A significant temperature dependent exchange bias field is obtained from above 100 K down to 2 K. These observations suggest that the particles have a Co rich SPM core, surrounded by uncompensated dilute Co spin moments at the surface. Such a distribution, with lowering of temperature, leads to the co-existence of

ferromagnetic (FM) and antiferromagnetic (AFM) interactions in the core and surface regions, respectively. Also, the sample exhibits a weak spin-glass like ordering occurring at ~ 7 K. The overall behavior of the system is that of an assembly of almost non-interacting magnetic nanoparticles as suggested by the study of relaxation of magnetization. If during relaxation certain external conditions are temporarily disturbed, *e.g.*, by lowering the temperature or changing the magnetic field the magnetization also changes accordingly; but as the conditions are restored the magnetization returns to its previous value. Such magnetic 'memory effect' has been studied with various experimental protocols and persists strongly even at room temperature.

Lastly, electrical resistivity of nanostructured granular alloys Co_xCu_{1-x} ($x \sim 0.01 - 0.76$) prepared by chemical reduction method are investigated in the temperature range 2-300 K. The samples with low cobalt content of $x \leq 0.1$ show a metallic resistivity behavior. For samples with higher cobalt content, $x \geq 0.17$, the resistivity shows a minimum. The minimum becomes more pronounced as Co content (x) increases and also the temperature of minimum resistivity, T_{min}, increases with x. Such trends continue even when x is as high as $\sim 76\%$. This is the first time resistivity minimum is observed in a metal alloy system with such high concentrations of a ferromagnetic element. Application of an external magnetic field has negligible effect on the resistivity behavior. Detailed analysis suggests that the low temperature upturn in resistivity most probably arises due to elastic electron-electron interaction (quantum interference effect). Magnetic measurements at 4 K on the same samples show absence of long range magnetic interaction and evidence of increasing magnetic disorder as x increases beyond $\sim 10\%$. Combining the results of the two types of measurements, a model of formation of these alloy particles involving random clusters of Co atoms within Cu matrix has been proposed.

4.2 Conclusion

We have presented here the results of magnetization and transport measurements on as-prepared and annealed nanosized particles of Co_xCu_{1-x} alloys with a wide range $\sim 0.01 - 0.76 mol\%$ of Co content. In as-prepared Co-0.01 sample with the lowest cobalt concentration of $\sim 0.01 mol\%$, there is negligible interaction among Co magnetic moments. In all other samples Co-0.03 $\rightarrow$ Co-0.33, the magnetization is a combination of ferromagnetic and superparamagnetic contributions with a blocking temperature distribution. Estimation of blocking temperature from ZFC/FC magnetization and TRM measurements do not differ significantly, implying that there is negligible dipolar interaction among the particles. Significantly, blocking temperatures are not dependent of overall composition of the samples. Study of hysteresis loops show that,

(i) the average saturation magnetic moment per Co atom, 0.45 (0.10) μ_B, does not change with Co content.

(ii) coercivity and magnetic anisotropy do not vary as the Co content.

(iii) Co atoms participating in ferromagnetism tend to increase and that in superparamagnetism decrease with increase in Co content.

The above observations indicate that for Co-0.03 $\rightarrow$ Co-0.33 samples, there is a cobalt rich part where ferromagnetism is favored, and another part low in cobalt that is superparamagnetic. Since the samples are in the form of small spherical particles and no segregation of copper and cobalt is observed in any sample, it is reasonable to conclude that Co_xCu_{1-x} alloy particles are formed in a core-shell type structure with the Co rich part at the core. With increase in Co concentration the size of the core increases in relation to the shell. The paramagnetic contribution to the magnetization comes from dilute Co atoms embedded in copper at or near the surface of particles. The magnetic properties

of an assembly of such particles, as we have studied here, are largely determined by the dipolar and exchange interactions among the cluster of Co atoms within a particle. Since they are capped with a surfactant, the particles are isolated and inter-particle interactions are negligible.

Study of magnetic measurements and magnetic memory effect results also show that the particles are formed with a cobalt rich superparamagntic (SPM) core region, and outside this region there is antiferromagnetic interaction between diluted Co moments. Magnetization and magnetic relaxation studies show the system as largely non-interacting SPM particles with a blocking temperature distribution, which eventually give rise to strong magnetic memory effects that have been observed in different measurement protocols and persists even at room temperature.

A detailed investigation of the temperature dependence of resistivity was carried out in the annealed granular alloy system of Co_xCu_{1-x} with varying Co content $x \sim 0.01$-0.76. All the samples show metallic resistivity behavior below the room temperature. A minimum in low temperature resistivity was found only in high Co containing samples. The resistivity behavior around the minimum is weakly dependent on magnetic field. It has been argued that the low temperature resistivity upturn arises from quantum interference effect induced by inherent disorder of the system. Magnetization studies show that with increase in Co content the magnetic disorder in the system increases and there is no inter particle long range interaction even at high Co concentrations. With the above magnetization and transport results and the observation, we have drawn a model for the formation of these non-interacting CoCu alloy particles in which at low Co concentrations (x), there are small cluster(s) of Co atoms surrounded by Cu on all sides. Electrical conduction in an assembly of such particles takes place mainly through copper and there is no significant scattering by Co clusters. Afterwards, when x goes above a value of ~ 0.16, there is no further increase in the cluster size. Instead, there is an increase only in the number of clusters inside a particle

by way of formation of new clusters and also disintegration of existing clusters.

4.3 Future aspects

In this thesis, different aspects of Co_xCu_{1-x} ($x \sim 0.01 - 0.76$) granular alloy prepared by chemical reduction method were extensively studied through complementary experimental techniques including structural, magnetic and transport studies. The system is nearly non-interacting, which enabled us to explore some interesting phenomena like superparamagnetism, strong memory effect, extremely long relaxation time, exchange bias and low temperature upturn in resistivity. There is a further scope of study of such non-interacting core-shell nanostructure system with different magnetic or combining magnetic ions suchas Ni, Mn, V etc. with noble metal such as Cu, Ag and Au. A detail theoretical study of core-shell model with variation of the cobalt content would also be helpful. In future, Monte Carlo simulations are expected to shed light on the structural agglomeration of the nanoparticles. In Chapter 3 we have highlighted the superparamagnetism and blocking, magnetic relaxation and strong memory effect of the nanoparticle system. Magneto-optic Kerr effect (MOKE), neutron diffraction, nuclear magnetic resonance (NMR) techniques are also very useful for magnetic characterization of such system. We have also observed low temperature upturn in resistivity in concentrated granular alloy system which have been analyzed for first time as electron−electron interaction. In this regard, study of Hall effect can be very useful for such system.

Bibliography

[1] D. L. Leslie-Pelecky and R. D. Rieke *Chem. Mater.*, vol. 8, p. 1770, 1996. 6, 20

[2] K. Raj, R. Moskowitz, and R.Casciari *J. Magn. Magn. Mater.*, vol. 149, p. 174, 1995. 6

[3] R. Cowburn *Phil. Trans. Soc. Lond.*, vol. A358, p. 281, 2000. 6

[4] L. S. R.D. McMichael, R.D. Shull and L. Bennet *J. Magn. Magn. Mater.*, vol. 111, p. 29, 1992. 6

[5] R. Shull *IEEE. Trans. Magn.*, vol. 29, p. 2614, 1993. 6

[6] P. Tartaj, M. del Puerto Morales, S. Veintemillas-Verdaguer, T. G. Carreno, and C. Serna *J. Phys. D:. Appl. Phys.*, vol. 36, p. R182, 2003. 6

[7] J. Eastman and R. W. Siegel *Res. Dev.*, vol. 31, p. 56, 1989. 6

[8] R. W. Siegel *Nanostruct. Mater.*, vol. 3, p. 1, 1993. 6

[9] H. Gleiter *Prog. mater. Sci.*, vol. 33, p. 223, 1989. 6

[10] V. G. Gryaznov and L. I. Trusov *Prog. mater. Sci.*, vol. 37, p. 289, 1993. 6

[11] J. Dormann and D. Fiorani, *Magnetic Properties of Fine Particles*. Amsterdam Pub. Co, 1992. 6

[12] B. H. Kear, L. E. Cross, J. E. Keem, R. W. Siegel, F. Spaepen, K. C. Taylor, E. L. Thomas, and K. N. Ru, *Research Opportunities for Materials with Ultrafine Microstructures*. national Academies, 1989. 6

[13] C. Suryanarayana *Int. mater. Rev.*, vol. 40, p. 41, 1995. 6

[14] R. D. Shull, *Report on the First NIST Workshop on Nanostructured Materials*. National Institute of Standards and Technology, 1994. 6

[15] H. Gleiter *Nanostruct. mater.*, vol. 1, p. 1, 1992. 6

[16] M. N. Baibich, J. M. Broto, A. Fert, F. N. V. Dau, F. Petroff, P. Etienne, G. Creuzet, A. Friederich, and J. Chazelas *Phys. Rev. Lett.*, vol. 61, p. 2472, 1988. 6, 7, 10, 11

[17] S. S. P. Parkin *Annu. Rev. Mater. Sci.*, vol. 25, p. 357, 1995. 6, 7

[18] C. Chien *Annu. Rev. Mater. Sci.*, vol. 25, p. 129, 1995. 6, 7

[19] A. E. Berkowitz, J. R. Mitchell, M. J. Carey, A. P. Young, S. Zhang, F. E. Spada, F. T. Parker, A. Hutten, and G. Thomas *Phys. Rev. Lett.*, vol. 68, p. 3745, 1992. 6, 7, 8, 10, 11

[20] J. Q. Xiao, J. S. Jiang, and C. L. Chien *Phys. Rev. Lett.*, vol. 68, p. 3749, 1992. 6, 7, 8, 11

[21] A. J. Rondinone and Z. J. Zhang 7, 15

[22] W. M. Star, F. B. Basters, G. M. Nap, E. de Vroede, and C. van Baarle *Physica*, vol. 58, p. 585, 1972. 7

[23] P. Wahl, A. P. Seitsonen, L. DiekhÃűner, M. A. Schneider, and K. Kern *New. J. Phys.*, vol. 11, p. 113015, 2009. 7, 10

[24] L. M. Fabietti, J. Ferreyra, M. Villafuerte, S. E. Urreta, and S. P. Heluani *Phys. Rev.*, vol. B82, p. 172410, 2010. 7, 8, 10, 105

[25] G. J. van den Berg, *Progress in Low Temperature Physics*, vol. IV. Amsterdam: North Holland, 1964. 7, 10

[26] V. V. Hiep, N. Chau, D. M. Hong, and N. H. Luong *J. Magn. Magn. Mater.*, vol. 310, p. 2524, 2007. 7

[27] I. Garcia, J. Echeberria, G. N. Kakazei, V. O. Golub, M. Ilyn, K. Y. Guslienko, and J. M. Gonzalez *J. Nanosci. Nanotechn.*, vol. 12, p. 7529, 2012. 7

[28] I. Garcia, J. A. Pomposo, J. Echeberria, J. Ollo, M. Ilyn., K. Y. Guslienko, and J. Gonzailez *J. Nanosci. Nanotechn.*, vol. 10, p. 4246, 2010. 7

[29] B. Gopalakrishnan, C. Surgers, R. Montbrun, A. Singh, M. Uhlarz, and H. v. Lohneysen *Phys. Rev.*, vol. B77, p. 104414, 2008. 7, 10

[30] J. A. D. Toro, J. P. Andres, J. A. Gonzalez, J. P. Goff, A. J. Barbero, and J. M. Riveiro *Phys. Rev.*, vol. B70, p. 224412, 2004. 7, 10

[31] C. Luna, M. P. Morales, C. J. Serna, and M. Vazquez *Nanotechnology*, vol. 15, pp. S293–297, 2004. 7

[32] S. E. Inderhees, J. A. Borchers, K. S. Green, M. S. Kim, K. Sun, G. L. Strycker, and M. C. Aronson *Phys. Rev. Lett.*, vol. 101, p. 117202, 2008. 7

[33] J. Y. Ji, P. Shih, T. S. Chan, Y. Ma, and S. Y. Wu *Nanoscale. Res. Lett.*, vol. 10, p. 243, 2015. 7

[34] M. Sasaki, P. E. Jonsson, H. Takayama, and H. Mamiya *Phys. Rev.*, vol. B71, p. 104405, 2005. 7, 8, 9, 35, 36, 90, 93

[35] R. K. Zheng, H. Gu, B. Xu, and X. X. Zhang *Phys. Rev.*, vol. B72, p. 014416, 2005. 7, 9, 36, 90

[36] Y. Sun, M. B. Salamon, K. Garnier, and R. S. Averback *Phys. Rev. Lett.*, vol. 91, p. 167206, 2003. 7, 8, 9, 35, 90

[37] S. Chakraverty, M. Bandyopadhyay, S. Chatterjee, S. Dattagupta, A. Frydman, S. Sengupta, and P. A. Sreeram *Phys. Rev.*, vol. B71, p. 054401, 2005. 7, 8, 9, 35

[38] M. Bandyopadhyay and S. Dattagupta *Phys. Rev.*, vol. B74, p. 214410, 2006. 7, 8, 9, 35, 36, 98

[39] H. Mamiya, I. Nakatani, and T. Furubayashi *Phys. Rev. Lett.*, vol. 82, p. 4332, 1999. 7, 8, 9, 35

[40] M. Thakur, M. P. Chowdhury, S. Majumdar, and S. Giri *Nanotechnology.*, vol. 19, p. 045706, 2008. 7, 8, 9, 35

[41] D. De, A. Karmakar, M. K. Bhunia, A. Bhaumik, S. Majumdar, and S. Giri *J. Appl. Phys.*, vol. 111, p. 033919, 2012. 7, 9, 88, 90, 98

[42] X. Chen, S. Bedanta, O. Petracic, W. Kleemann, S. Sahoo, S. Cardoso, and P. P. Freitas *Phys. Rev.*, vol. B72, p. 214436, 2005. 7, 9

[43] E. C. Stoner and E. P. Wohlfarth *Philos. Trans. R. Soc. London*, vol. 240, p. 599, 1948. 8

[44] J. Wecker, R. von Helmolt, L. Schultz, and K. Samwer *Appl. Phys. Lett.*, vol. 62, p. 1985, 1993. 8

[45] B. J. Hickey, M. A. Howson, S. O. Musa, G. J. Tomka, B. D. Rainford, and N. Wiser *J. Magn. Magn. Mat.*, vol. 147, p. 253, 1995. 8

[46] B. J. Hickey, M. A. Howson, S. O. Musa, and N. Wiser *Phys. Rev.*, vol. B51, p. 667, 1995. 8

[47] V. M. Fedosyuk, O. I. Kasyutich, D. Ravinder, and H. J. Blythe *J. Magn. Magn. Mat.*, vol. 156, p. 345, 1996. 8

[48] V. M. Fedosyuk and O. I. Kasyutich *Thin Solid Films*, vol. 230, p. 4, 1993. 8

[49] H. Blythe and V. M. Fedosyuk *J. Magn. Magn. Mat.*, vol. 155, p. 352, 1996. 8

[50] V. M. Fedosyuk and O. I. Kasyutich *J. Magn. Magn. Mat.*, vol. 125, p. 330, 1996. 8

[51] H. Blythe, V. Fedosyuk, O. Kasyutich, and W. Schwarzacher *J. Magn. Magn. Mat.*, vol. 208, p. 251, 2000. 8

[52] P. Allia, M. Coisson, P. Tiberto, F. Vinai, M. Knobel, M. A. Novak, and W. C. Nunes *Phys. Rev.*, vol. B64, p. 144420, 2001. 8, 29, 66, 69

[53] P. Panissod, M. Malinowska, E. Jedryka, M. Wojcik, S. Nadolski, M. Knobel, and J. E. Schmidt *Phys. Rev.*, vol. B63, p. 014408, 2000. 8

[54] R. W. Chantrell, M. El-Hilo, and K. O'Grady *IEEE Trans. Magn.*, vol. 27, p. 3570, 1991. 8

[55] J. R. Childress and C. L. Chien *Phys. Rev.*, vol. B43, p. 8089, 1991. 8, 65, 80

[56] H. J. Blythe and V. M. Fedosyuk *Phys. Stat. Sol. (a)*, vol. 146, p. K13, 1994. 9

[57] H. J. Blythe and V. M. Fedosyuk *J. Phys.: Condens. Mat.*, vol. 7, p. 3461, 1995. 9

[58] R. K. Zheng, H. Gu, and X. X. Zhang *Phys. Rev. Lett.*, vol. 93, p. 139702, 2004. 9, 36

[59] M. Sasaki, P. E. Jonsson, H. Takayama, and P. Nordblad *Phys. Rev. Lett.*, vol. 93, p. 139701, 2004. 9, 36

[60] D. Hanning, Y. Songliu, Z. Xianfeng, and T. Zhaoming *J. Wuhan Univ. of Techn. Mater. Sci. Ed.*, vol. 28, p. 467, 2013. 9

[61] N. H. Nam and N. H. Luong *VNU J. Sci.: Mathematics and Physics*, vol. 30, p. 3, 2014. 9

[62] W. H. Meiklejohn *J. Appl. Phys.*, vol. 33, p. 1328, 1962. 9

[63] E. P. Wohlfarth *Adv. Phys.*, vol. 8, p. 87, 1959. 9

[64] H. Schmid *Cobalt.*, vol. 6, p. 8, 1960. 9

[65] F. S. Luborsky *Electro. Technol.*, vol. 107, p. 8, 1960. 9

[66] J. S. Kouvel *J. Phys. Chem. Solids.*, vol. 24, p. 795, 1963. 9

[67] N. H. March, P. Lambin, and F. Herman *J. Magn. Magn. Mater.*, vol. 44, p. 1, 1984. 9

[68] A. E. Berkowitz and K. Takano *J. Magn. Magn. Mater.*, vol. 200, p. 552, 1999. 9

[69] J. Nogues and I. K. Schuller *J. Magn. Magn. Mater.*, vol. 192, p. 203, 1999. 9

[70] R. L. Stamps *J. Phys. D:. Appl. Phys.*, vol. 33, p. R247, 2000. 9

[71] M. Kiwi *J. Magn. Magn. Mater.*, vol. 234, p. 584, 2001. 9

[72] C. Binek *Spinger. Tr. Mod. Phys.*, vol. 196, p. 1, 2003. 9

[73] J. F. Bobo, L. Gabillet, and M. Bibes *J. Phys.: Condens. matter.*, vol. 16, p. S471, 2003. 9

[74] J. Nogues, J. Sort, V. Langlais, V. Skumryev, S. Surinach, J. S. Munoz, and M. D. Baro *Phys. Rep.*, vol. 422, p. 65, 2005. 9

[75] J. Nogues, J. Sort, V. Langlais, V. Skumryev, S. S. S, J. S. Munoz, and M. D. Baro *Int. J. Nanosci.*, vol. 2, p. 23, 2005. 9

[76] O. Iglesias, A. Labarta, and X. Batlle *J. Nanosci. Nanotecnol.*, vol. 8, p. 2761, 2008. 9

[77] J. S. Kouvel and C. D. Graham *J. Phys. Chem. Solids.*, vol. 11, p. 220, 1959. 9

[78] J. S. Kouvel, C. D. Graham, and I. S. Jacobs *J. Phys. Radium.*, vol. 20, p. 198, 1959. 9

[79] J. S. Kouvel and C. D. Graham *J. Appl. Phys.*, vol. 30, p. 312S, 1959. 9

[80] J. S. Kouvel *J. Phys. Chem. Solids.*, vol. 16, p. 152, 1960. 9

[81] J. S. Kouvel and W. Abdul-Razzaq *J. Magn. Magn. Mater.*, vol. 53, p. 139, 1985. 9

[82] J. S. Kouvel *J. Phys. Chem. Solids.*, vol. 21, p. 57, 1961. 9

[83] J. S. Kouvel *J. Phys. Chem. Solids.*, vol. 16, p. 107, 1960. 9

[84] M. P. Sarachik, E. Corenzwit, and L. D. Longinotti *Phys. Rev.*, vol. 135(4A), p. 1041, 1964. 10

[85] M. D. Daybell and W. A. Steyert *Phys. Rev. Lett*, vol. 18, p. 398, 1967. 10

[86] M. A. Jensen, A. J. Heeger, L. B. Welsh, and G. Gladstone *Phys. Rev. Lett.*, vol. 18, p. 997, 1967. 10

[87] R. B. Prankel, N. A. Blum, B. B. Schwartz, and D. J. Kim *Phys. Rev. Lett.*, vol. 18, p. 1051, 1967. 10

[88] M. D. Daybell and W. A. Steyert *Phys. Rev. Lett*, vol. 20, p. 195, 1968. 10

[89] Y. Mei, E. H. Tyler, and H. L. Luo *Phys. Rev.*, vol. B26, p. 4299, 1982. 10

[90] Y. Mei and H. L. Luo *Phys. Rev.*, vol. B34, p. 509, 1986. 10, 103

[91] C. Deenadas, A. W. Thompson, R. S. Craig, and W. E. Wallace *J. Phys. Chem. Sol.*, vol. 32, p. 1853, 1971. 10

[92] B. Cornut and B. Coqblin *Phys. Rev.*, vol. B8, p. 4541, 1972. 10

[93] M. N. Francillon, A. Percheron, J. C. Achard, O. Gorpchov, B. Cornut, D. Jerome, and B. Coqblin *Sol. St. Commun.*, vol. 11, p. 845, 1972. 10

[94] F. Steglich, W. Franz, W. Seuken, and M. Loewenhaupt *Physica*, vol. B86-88, p. 503, 1977. 10

[95] C. D. Bredl, F. Steglich, and K. D. Schotte *J. Magn. Magn. Mater.*, vol. 9, p. 60, 1978. 10

[96] T. Komatsubara, T. Suzuki, M. Kawakami, S. Kunii, T. Fujita, Y. Isikawa, A. Takase, K. Kojima, M. Suzuki, Y. Aoki, K. Takegahara, and T. Kasuya *J. Magn. Magn. Mater.*, vol. 15-18, p. 963, 1980. 10

[97] P. Bonville *Int. Conf. on the Applications of the Mossbauer Effect*, vol. 40, p. 15, 1987. 10

[98] M. Ilyn, V. Zhukova, C. Garcia, J. J. del Val, M. Ipatov, A. Granovsky, and A. Zhukov *IEEE Transac. Magn.*, vol. 48, p. 3532, 2012. 10

[99] O. Rapp, S. M. Bhagat, and H. Gudmundsson *Sol. St. Commun.*, vol. 42, p. 741, 1982. 10, 39, 104

[100] R. W. Cochrane and J. O. Strom-Olsen *Phys. Rev.*, vol. B29, p. 1088, 1984. 10, 39, 104

[101] B. Sas, T. Kemeny, J. Toth, and F. I. B. Williams *Mater. Sci. Engg.*, vol. 99, p. 223, 1988. 10, 39, 104

[102] A. Barman, M. Ghosh, S. Biswas, S. K. De, and S. Chatterjee *Sol. St. Commun.*, vol. 106, p. 691, 1998. 10, 39

[103] A. Tiwari and K. P. Rajeev *Sol. St. Commun.*, vol. 111, p. 33, 1999. 10, 39

[104] E. Rozenberg, M. Auslender, I. Felner, and G. Gorodetsky *J. Appl. Phys.*, vol. 88, p. 2578, 2000. 10, 39, 104

[105] D. Kumar, J. Sankar, J. Narayan, R. K. Singh, and A. K. Majumdar *Phys. Rev.*, vol. B65, p. 094407, 2002. 10, 39

[106] Y. Xu, J. Zhang, G. Cao, C. Jing, and S. Cao *Phys. Rev.*, vol. B73, p. 224410, 2006. 10, 39

[107] L. Maritato, C. Adamo, C. Barone, G. M. de Luca, A. Galdi, P. Orgiani, and A. Y. Petrov *Phys. Rev.*, vol. B73, p. 094456, 2006. 10, 39

[108] S. Mukhopadhyay and I. Das *Europhys. Lett.*, vol. 79, p. 67002, 2007. 10, 39

[109] R. R. Jia, J. C. Zhang, R. K. Zheng, D. M. Deng, H.-U. Habermeier, H. L. W. Chan, H. S. Luo, and S. X. Cao *Phys. Rev.*, vol. B82, p. 104418, 2010. 10, 39

[110] M. Knobel, W. C. Nunes, L. M. Socolovsky, E. de Biasi, J. M. Vargas, and J. C. Denardin *J. Nanosci. and Nanotech.*, vol. 8, p. 2836, 2008. 11, 98

[111] B. J. Hickey, M. A. Howson, D. Greig, and N. Wiser *Phys. Rev.*, vol. B53, p. 32, 1996. 11, 86

[112] M. J. Carey, A. P. Young, A. Starr, D. Rao, and A. E. Berkowitz *Appl. Phys. Lett.*, vol. 61, p. 2935, 1992. 11

[113] H. Sakakima and S. Satomi *Jpn. J. Appl. Phys.*, vol. 31, p. 484, 1992. 11

[114] M. Jimbo, S. Tsunashima, T. Kanda, S. Goto, and S. Uchiyama *J. Appl. Phys.*, vol. 74, p. 3341, 1993. 11

[115] K. Attenborough, R. Hart, S. J. Lane, M. Alper, and W. Schwarzacher *J. Magn. Magn. Mat.*, vol. 148, p. 335, 1995. 11

[116] Y. D. Zhang, J. I. Budnick, W. A. Hines, C. L. Chien, and J. Q. Xiao *Appl. Phys. Lett.*, vol. 72, p. 2053, 1998. 11

[117] C. B. Ene, G. Schmitz, R. Kirchheim, D. Rao, and A. Hutten *Acta. Mater.*, vol. 53, p. 3383, 2005. 11

[118] S. K. Ghosh, A. K. Grover, P. Chowdhury, S. K. Gupta, and G. Ravikumar *Appl. Phys. Lett.*, vol. 89, p. 132507, 2006. 11

[119] R. Kodama *J. Magn. Magn. Mater.*, vol. 200, p. 359, 1999. 12

[120] R. Zysler, D. Fiorani, J. L. Dormann, and A. M. Testa *J. Magn. Magn. Mater.*, vol. 133, p. 71, 1994. 12

[121] B. D. cullity, *Introduction to Magnetic Materials*. Massachusetts: Addison-Wesley Pub.Co., 1972. 13, 25

[122] L. Neel *Ann. Geophys.*, vol. 5, p. 99, 1949. 13, 98

[123] W. F. B. Jr. *J. Appl. Phys.*, vol. 34, p. 1319, 1963. 13

[124] J. W. Brown *IEEE. Trans. Magn.*, vol. MAG-15, p. 1196, 1979. 13

[125] P. Weiss *Compt. Rend.*, vol. 143, p. 1136, 1906. 18

[126] J. Frenkel and J. Dorfman *Nature.*, vol. 126, p. 274, 1930. 19

[127] C. Kittel *Phys. Rev.*, vol. 70, p. 965, 1946. 19, 20

[128] C. Liu, B. Zou, A. J. Rondinone, and Z. J. Zhang *J. Phys. Chem.*, vol. B104, p. 1141, 2000. 23, 24, 28

[129] J. I. Gittlemann, B. Abeles, and S. Bosowski *Phys. Rev.*, vol. B9, p. 3891, 1974. 24

[130] A. J. Rondinone, A. C. S. Samia, and Z. J. Zhang *J. Phys. Chem.*, vol. B103, p. 6876, 1999. 24, 28

[131] M. F. Hansen and S. Morup *J. Magn. Magn. Mater.*, vol. 203, p. 214, 1999. 24

[132] C. Cannas, G. Concas, D. Gatteschi, A. Falqui, A. Musinu, G. Piccaluga, C. Sangregorio, and G. Spano *Phys. Chem. Chem. Phys.*, vol. 3, p. 832, 2001. 24

[133] L. Neel *C. R. Acad. Sci.*, vol. 228, p. 664, 1949. 25

[134] P. Bean and J. D. Livingston *J. Appl. Phys.*, vol. 30, p. 120, 1959. 25

[135] J. C. Denardin, A. L. Brandl, M. Knobel, P. Panissod, A. B. Pakhomov, H. Liu, and X. X. Zhang *Phys. Rev.*, vol. B65, p. 064422, 2002. 29, 66, 67, 69, 70

[136] S. Morup, J. A. Dumesic, and H. Topsoe, *In Applications to Mossbauer Spectroscopy vol 2*. Acadamec Press Pub.Co., 1980. 29

[137] S. Morup, M. B. Madsen, J. Franck, J. Villadsen, and C. J. W. Kock *J. Magn. Magn. Mater.*, vol. 40, p. 163, 1983. 29

[138] W. H. Meiklejohn and C. P. Bean *Phys. Rev.*, vol. 102, p. 1413, 1956. 32

[139] W. H. Meiklejohn and C. P. Bean *Phys. Rev.*, vol. 105, p. 904, 1956. 32

[140] F. Lefloch, J. Hammann, M. Ocio, and E. Vincent *Europhys. Lett.*, vol. 18, p. 647, 1992. 35

[141] J. Kondo *Prog. Theor. Phys.*, vol. 32, p. 37, 1964. 38

[142] J. Kondo *Physica*, vol. B84, p. 40, 1976. 38

[143] S. N. Kaul, W. Kettler, and M. Rosenberg *Phys. Rev.*, vol. B33, p. 4987, 1986. 39

[144] J. S. Dugdale *Contemp. Phys.*, vol. 28, p. 574, 1987. 39

[145] P. A. Lee and T. V. Ramakrishnan *Rev. Mod. Phys.*, vol. 57, p. 287, 1985. 39, 104

[146] B. Altshuler and A. Aronov *Zh. Eksp. Teor. Fiz.*, vol. 77, p. 2028, 1979. 40

[147] B. Altshuler and A. Aronov *Solid. State. Commun.*, vol. 30, p. 115, 1979. 40

[148] B. I. Shklovskii and A. L. Efros, *Electronic Properties of Doped Semiconductors*. Springer, 1984. 40

[149] Z. Qiu-li, Y. Zhi-mao, D. Bing-jun, L. Xin-zhe, and G. Ying-juan *Trans. Norferrous Met. Soc. China*, vol. 20, p. 240, 2010. 42

[150] S.-H. Wu and D.-H. Chen *J. Colloid. Interface Sci.*, vol. 273, p. 165, 2004. 42

[151] J. M. D. Coey, A. E. Berkowitz, L. Balcells, F. F. Putris, and A. Barry *Phys. Rev. Lett.*, vol. 80, p. 3815, 1998. 43, 109

[152] W. A. Jesser and J. W. Matthews *Philos. Mag.*, vol. 17, p. 461, 1968. 48, 76

[153] C. Papusoi *J. Magn. Magn. Mat.*, vol. 195, p. 708, 1999. 65

[154] S. Modak, S. Karan, S. K. Roy, and P. K. Chakrabarti *J. Appl. Phys.*, vol. 108, p. 093912, 2010. 65

[155] J. J. Lu, H. Y. Deng, and H. L. Huang *J. Magn. Magn. Mat.*, vol. 37, p. 209, 2000. 66

[156] K. Zaveta, H. K. Lachowicz, M. Marysko, Z. Arnold, and P. Dluzewski *J. Alloys and Compds.*, vol. 392, p. 12, 2005. 66

[157] R. Torchio, C. Meneghini, S. Mobilio, G. Capellini, A. G. Prieto, J. Alonso, M. Fdez-Gubieda, V. T. Liveri, A. Longo, A. M. Ruggirello, and T. Neisius *J. Mag. Mag. Matt.*, vol. 322, p. 3565, 2010. 68, 80

[158] L. Tauxe, T. A. T. Mullender, and T. Pick *J. Geophys. Res.*, vol. 101, p. 571, 1996. 71

[159] B. Bandyopadhyay, B. Pahari, and K. Ghoshray *Phys. Rev.*, vol. B76, p. 214424, 2007. 72

[160] J. P. vejpravova, V. Sechovsky, D. Niznansky, J. Plocek, A. Hutlova, and J. L. Rehspringer *J. Appl. Phys.*, vol. 97, p. 124304, 2005. 72

[161] J. P. Bucher, D. C. Douglass, and L. A. Bloomfield *Phys. Rev. Lett.*, vol. 66, p. 3052, 1991. 76

[162] S. N. Khanna and S. Linderoth *Phys. Rev. Lett.*, vol. 67, p. 742, 1991. 76

[163] D. C.Douglass, A. J. Cox, J. P. Bucher, and L. A. Bloomfield *Phys. Rev.*, vol. B47, p. 12874, 1993. 76

[164] A. Garvin and C. L. Chien *J. Appl. Phys.*, vol. 67, p. 938, 1990. 76

[165] G. Xiao, S. H. Liou, A. Levy, J. N. Taylor, and C. L. Chien *Phys. Rev.*, vol. B34, p. 7573, 1986. 76

[166] C. L. Chien *J. Appl. Phys.*, vol. 69, p. 5267, 1991. 76

[167] G. A. Candela and R. A. Haines *Appl. Phys. Lett.*, vol. 34, p. 868, 1979. 79

[168] J. A. Mydosh, *Spin Glasses: An Experimental Introduction*. CRC Press, 1993. 80

[169] D. N. H. Nam, R. Mathieu, P. Nordblad, N. V. Khiem, and N. X. Phuc *Phys. Rev.*, vol. B62, p. 1027, 2000. 80

[170] M. Thakur, S. Majumdar, S. Giri, A. Bhaumik, M. Nandi, H. Nakamura, H. Kobayashi, and T. Kohara *J. Phys.: Condens. Matter*, vol. 20, p. 295228, 2008. 80

[171] T. Zhang, X. P. Wang, Q. F. Fang, and X. G. Li *Appl. Phys. Rev.*, vol. 1, p. 031302, 2014. 82

[172] J. Curiale, M. Granada, H. E. Troiani, R. D. Sanchez, A. G. Leyva, P. Levy, and K. Samwer *Appl. Phys. Lett.*, vol. 95, p. 043106, 2009. 82

[173] M. Ulrich, J. Garcia-Otero, J. Rivas, and A. Bunde *Phys. Rev.*, vol. B67, p. 024416, 2003. 88

[174] S. Chakraverty, B. Ghosh, S. Kumar, and A. Frydmana *Appl. Phys. Lett.*, vol. 88, p. 042501, 2006. 98, 99

[175] N. Khan, P. Mandal, and D. Prabhakaran *Phys. Rev.*, vol. B90, p. 024421, 2014. 98

[176] L. Balcells, J. Fontcuberta, B. Martinez, and X. Obradors *Phys. Rev.*, vol. B58, p. R14697, 1998. 101

[177] P. Sheng, B. Abeles, and Y. Arie *Phys. Rev. Lett.*, vol. 31, p. 44, 1973. 102

[178] J. S. Helman and B. Abeles *Phys. Rev. Lett.*, vol. 37, p. 1429, 1976. 102, 106

[179] O. Ciftija, M. Luban, M. Auslender, and J. H. Luscombe *Phys. Rev.*, vol. B60, p. 10122, 1999. 105

[180] M. I. Auslender, E. Rozenberg, A. E. Karlin, B. K. Chaudhuri, and G. Gorodetsky *J. Alloys Compd.*, vol. 326, p. 81, 2001. 105

[181] H. Sato, K. Honda, Y. Aoki, N. Kataoka, I. J. Kim, and K. Fukamichi *J. Mag. Mag. Mat.*, vol. 152, p. 109, 1996. 108

[182] S. B. Arnason, S. P. Herschfield, and A. F. Hebard *Phys. Rev. Lett.*, vol. 81, p. 3936, 1998. 108